

Electronic Thesis and Dissertation Repository

5-5-2023 1:30 PM

Spatiotemporal Optimization of Intratumoural Electric Field Modulation for Cancer Therapy

Erin Iredale,

Supervisor: Wong, Eugene, *The University of Western Ontario*

Co-Supervisor: Peters, Terry, *The University of Western Ontario*

A thesis submitted in partial fulfillment of the requirements for the Doctor of Philosophy degree in Medical Biophysics

© Erin Iredale 2023

Follow this and additional works at: <https://ir.lib.uwo.ca/etd>



Part of the [Medical Biophysics Commons](#)

Recommended Citation

Iredale, Erin, "Spatiotemporal Optimization of Intratumoural Electric Field Modulation for Cancer Therapy" (2023). *Electronic Thesis and Dissertation Repository*. 9289.

<https://ir.lib.uwo.ca/etd/9289>

This Dissertation/Thesis is brought to you for free and open access by Scholarship@Western. It has been accepted for inclusion in Electronic Thesis and Dissertation Repository by an authorized administrator of Scholarship@Western. For more information, please contact wlsadmin@uwo.ca.

Abstract

The use of anti-cancer non-ablative electric fields is an expanding area of research that includes clinically available external devices for the treatment of glioblastoma (GBM), and a pre-clinical internal system called Intratumoural Modulation Therapy (IMT). IMT uses multiple electrodes implanted within the tumour to apply low intensity electric fields (~ 1 V/cm) focused on the target region, anywhere in the brain, with no externally visible devices. In this thesis, multi-electrode spatiotemporally dynamic IMT is investigated through computer simulation, numerical optimization, brain phantom and *in vitro* validation methods. These planning and validation strategies are hypothesized to improve tumour coverage with the necessary electric field and improving treatment efficiency through minimizing number of electrodes, power consumption, and manual planning time.

The development of an IMT optimization algorithm that considers the placement of multiple electrodes, voltage amplitude and phase shift of input waveforms showed that human scale tumours are coverable with anti-cancer electric fields. Additionally, maximally separating the relative phase shifts of sinusoidal voltage waveforms applied to the electrodes, induces rotating electric fields that cover the tumour over time, with spatially homogeneous time averaged fields. A treatment planning system designed specifically for IMT considered optimizable electrode trajectories and patient images to create custom field plans for each patient, which was validated using robotic electrode implantation on a brain phantom. These custom fields can be optimized to conform to patient-specific tumour size, shape, or location. The efficacy of spatiotemporally dynamic fields was validated by developing a purpose-built *in vitro* device to deliver multi-electrode IMT to patient derived GBM cells. Cell viability was reduced when subjected to these rotating electric fields, supporting the optimality criteria derived analytically.

The IMT optimization algorithm and planning system, supporting phantom validation and *in vitro* data, together with an accompanying planning system user guide support the move to clinical trials in the future. Overall, IMT technology has been advanced in this thesis to include patient-specific treatment planning optimization, a development that holds significance towards the future clinical implementation of IMT and treatment goals.

Keywords

Electric Field, Optimization, Brain Cancer, Brain Tumour, Glioblastoma, Electrotherapy, Intratumoural Modulation Therapy, Non-Ionizing Radiation, Computer Simulation.

Summary for Lay Audience

A recent advancement in brain cancer research is the use of electric fields to control the disease. These electric fields can be applied either externally in the form of an electrode cap, or internally with implanted electrodes. The former is available clinically, and the latter is the topic of this thesis. Electric fields delivered directly using electrodes surgically placed within the brain tumour is a method called Intratumoural Modulation Therapy (IMT). Computerized optimization allows us to determine the ideal treatment settings to best cover the tumour with the prescribed electric field. In this thesis, anti-cancer electric fields are optimized for brain cancer treatment, through the development of an IMT optimization algorithm, a patient-specific IMT treatment planning system, and *in vitro* validation of optimized rotating electric fields.

It was found through computer simulations and a custom designed optimization algorithm that human scale tumours can be covered with sufficient anti-cancer electric fields from multiple electrodes placed in the tumour at optimized locations. The settings of the applied voltage waveforms to each electrode resulted in fields that moved over time to cover the entire tumour. A treatment planning system was then developed that incorporates this optimization algorithm. Patient images are used in conjunction with treatment goals including electric field dose and number of electrodes, where the treatment provider can run the simulator and optimizer to design a patient-specific treatment plan. The planning system was validated by performing an electrode implantation on a brain phantom using a robotic insertion technique. Finally, the rotating electric fields found to have the best coverage were investigated *in vitro*, where a device was designed to deliver reliable reproducible stimulation to multiple wells simultaneously. The results of this study found rotating fields effective at reducing the viability of brain cancer cells, where the strength of the electric field was the main driver of cell death. The optimization strategies applied in the planning system were found to be impactful with more tumour cell kill observed in trials using optimized settings. Overall, the discoveries made in this thesis are significant in the development of IMT and patient-specific treatment planning.

Co-Authorship Statement

Chapter 2 was adapted from the published article entitled “Optimization of multi-electrode implant configurations and programming for the delivery of non-ablative electric fields in intratumoral modulation therapy” by Erin Iredale, Andrew Deweyert, Douglas A. Hoover, Jeff Z. Chen, Susanne Schmid, Matthew O. Hebb, Terry M. Peters, and Eugene Wong, *Medical Physics*, **47**(11):5441-5454 (2020). Erin Iredale developed the optimization algorithm, performed the simulations and optimizations, performed the sensitivity analysis, designed the proposed in vitro experiment, and wrote the manuscript. Douglas Hoover, Jeff Chen, Terry Peters, and Eugene Wong provided input on the algorithm design and helped edit the manuscript. Andrew Deweyert, Susanne Schmid, and Matthew Hebb provided input from the biological perspective and helped edit the manuscript.

Chapter 3 was adapted from the published article entitled “Planning system for the optimization of electric field delivery using implanted electrodes for brain tumor control” by Erin Iredale, Brynn Voigt, Adam Rankin, Kyungho W. Kim, Jeff Z. Chen, Susanne Schmid, Matthew O. Hebb, Terry M. Peters, and Eugene Wong, *Medical Physics*, **49**(9):6055-6067 (2022). Erin Iredale designed the treatment planning system, coded the optimization algorithm and parts of the Slicelet, performed all treatment planning system testing, designed, and carried out the robot-assisted electrode implantation in the brain phantom, and wrote the manuscript. Brynn Voigt assisted in coding the Slicelet. Adam Rankin aided in carrying out the robot-assisted electrode implantation. William Kim coded the smoothing module used in the Slicelet. Jeff Chen, Terry Peters, and Eugene Wong provided input on the design of the planning system and phantom experiment and helped edit the manuscript. Susanne Schmid and Matthew Hebb provided input from the biological perspective and helped edit the manuscript.

Chapter 4 was adapted from the published article entitled “Spatiotemporally dynamic electric fields for brain cancer treatment: an in vitro investigation” by Erin Iredale, Abdulla Elsaleh, Hu Xu, Paul Christiaans, Andrew Deweyert, John Ronald, Susanne Schmid, Matthew O. Hebb, Terry M. Peters, and Eugene Wong, *Physics in Medicine and Biology*, **68**:085012 (2023). Erin Iredale designed all experiments, performed the in vitro voltage measurements

to determine the electrical conductivity of DMEM, performed all computer simulations and optimizations, analyzed the bioluminescence imaging (BLI) results, and wrote the manuscript. Abdulla Elsaleh performed the in vitro cell work and obtained the bioluminescence images. Hu Xu provided insight on cell culturing, Paul Christiaans developed the printed circuit board, and John Ronald provided insight on BLI methods. Susanne Schmid and Matthew Hebb provided input from the biological perspective, the facilities to perform cell work, provided the patient derived cells, and helped edit the manuscript. Terry Peters and Eugene Wong provided input on the physics and experiment design and helped edit the manuscript.

Acknowledgements

I would like to start by thanking my supervisors, Dr. Eugene Wong, and Dr. Terry Peters for allowing me the opportunity to conduct my PhD research in such a supportive and positive environment. I have learned so much through your mentorship and advice, both academically and professionally. I am grateful to have had supervisors who showed such dedication and encouragement. Additionally, to my advisory committee member Dr. Matthew Hebb, thank you for taking the time to provide guidance from the clinical perspective and for your mentorship through the years.

I thank the members of the IMT research team, collaborators, and co-authors over the years, with a special thank you to long time collaborators Dr. Susanne Schmid, Dr. Andrew Deweyert, Dr. Jeff Chen, and to the members of the Wong and VASST labs, past and present. I would also like to thank the Department of Medical Biophysics staff, administrators, and teachers at Western University. I thank the members of the Physics and Astronomy Department for aiding with developing device prototypes, specifically Paul Christiaans and Brian Dalrymple.

I acknowledge the sources on funding that have supported this work, including NSERC CGS-M and NSERC CGS-D, and the funding of my supervisors and supervisory committee; NSERC Idea to Innovation Grant, NSERC Discovery Grant, Cancer Research Society, the Canada Foundation for Innovation (CFI), and the Western Innovation Fund.

Last but certainly not least, I would like to thank my family, who are the reason for all that I do. My parents Susan and Tim, my brother Jordan and sister-in-law Samantha, my heavenly grandparents James, Violet, and Norman, and my grandmother Jackie. And my dogs, who have provided much stress-relief and comfort over the years, Tilly, Maggie, and Sully. I am truly blessed to have all of you.

Dedication

To my family, Susan, Tim, Jordan, and Sam

For making this possible with your unwavering love and support

Table of Contents

Abstract.....	ii
Summary for Lay Audience.....	iv
Co-Authorship Statement.....	v
Acknowledgements.....	vii
Dedication.....	viii
Table of Contents.....	ix
List of Tables.....	xiv
List of Figures.....	xv
List of Appendices.....	xxi
List of Abbreviations.....	xxii
Chapter 1.....	1
1 General Introduction.....	1
1.1 Motivation and Overview.....	1
1.2 Electric Field Theory.....	1
1.3 Electric Fields in Medicine.....	4
1.3.1 Tumour Treating Fields.....	5
1.3.2 Mechanism of Tumour Treating Fields.....	6
1.3.3 Tumour Ablation Techniques.....	7
1.3.4 Non-Cancer Applications.....	8
1.4 Electric Field Computer Simulations.....	9
1.5 Numerical Optimization.....	11
1.6 Intratumoural Modulation Therapy.....	12
1.7 Research Hypothesis.....	14
1.8 Research Objectives.....	14

1.9	References.....	15
Chapter 2.....		24
2	Optimization of Multi-Electrode Implant Configurations and Programming for the Delivery of Non-Ablative Electric Fields in Intratumoural Modulation Therapy	24
2.1	Introduction.....	24
2.2	Materials and Methods.....	27
2.2.1	Electric Field Simulation	27
2.2.2	Sensitivity Analysis	29
2.2.3	Optimization Algorithm.....	30
2.2.4	Robustness of the Pattern Search Algorithm	33
2.2.5	Spherical Tumour Optimal Configurations, Phase Shift and Maximum Treatable Tumour Size.....	34
2.2.6	Tissue Sparing.....	34
2.3	Results.....	35
2.3.1	Sensitivity Analysis	35
2.3.2	Robustness of the Pattern Search Algorithm	35
2.3.3	Spherical Tumour Optimal Configurations, Phase Shift and Maximum Treatable Tumour Size.....	36
2.3.4	Tissue Sparing.....	44
2.4	Discussion.....	45
2.5	Conclusions.....	49
2.6	Appendix.....	49
2.7	Acknowledgements.....	51
2.8	Conflicts of Interest.....	51
2.9	References.....	52
Chapter 3.....		56
3	Planning System for the Optimization of Electric Field Delivery using Implanted Electrodes for Brain Tumour Control	56

3.1	Introduction.....	56
3.2	Materials and Methods.....	60
3.2.1	Slicelet Design	60
3.2.2	Smoothing and Electrode Implantation Modules	60
3.2.3	Optimization Module	61
3.2.4	Planning System Testing.....	64
3.2.5	Phantom Electrode Implantation.....	65
3.3	Results.....	66
3.3.1	Slicelet Design	66
3.3.2	Smoothing and Electrode Implantation Modules	66
3.3.3	Optimization Module	67
3.3.4	Planning System Testing.....	67
3.3.5	Phantom Electrode Implantation.....	69
3.4	Discussion.....	72
3.5	Conclusions.....	76
3.6	Acknowledgements.....	76
3.7	Conflicts of Interest.....	76
3.8	References.....	77
	Chapter 4.....	83
4	Spatiotemporally Dynamic Electric Fields for Brain Cancer Treatment: An In Vitro Investigation.....	83
4.1	Introduction.....	83
4.2	Materials and Methods.....	85
4.2.1	In Vitro Electrical Conductivity Measurement.....	85
4.2.2	Electrode Construct Design Optimization	86
4.2.3	Experiment Design Optimization	87

4.2.4	In Vitro IMT Model	88
4.3	Results	89
4.3.1	In Vitro Electrical Conductivity Measurement	89
4.3.2	Electrode Construct Design Optimization	89
4.3.3	Experiment Design Optimization	90
4.3.4	In Vitro IMT Model	93
4.4	Discussion	96
4.5	Conclusions	99
4.6	Acknowledgements	99
4.7	Conflicts of Interest	100
4.8	References	100
Chapter 5	103
5	General Discussion and Conclusions	103
5.1	Overview and Research Questions	103
5.2	Limitations	105
5.3	Future Directions	106
5.3.1	Biological	107
5.3.2	Computational	107
5.3.3	Device Development	108
5.4	Significance	109
5.5	References	110
Appendices	112
Appendix A	– Permission to Reproduce Content	112
Appendix B	– Supplemental Materials for Chapter 1	121
Appendix C	– Supplemental Materials for Chapter 2	129
Appendix D	– Supplemental Materials for Chapter 3	132

Appendix E – Supplemental Materials for Chapter 4	136
Appendix F – IMT Planning System (IMTPS) User Guide.....	140
Curriculum Vitae	154

List of Tables

Table 1.1: Stimulation parameters for electrotherapy devices including voltage, frequency, and average electric field.	4
---	---

List of Figures

- Figure 1.1: Summary of proposed mechanisms of action for tumour treating electric fields. TTFields have been found to be (a) anti-mitotic, (b) to decrease DNA repair, (c) to decrease cell migration, (d) to promote autophagy, (e) to promote an immune response, and (f) to increase membrane permeability and blood brain barrier breaching..... 7
- Figure 1.2: Pattern search optimization strategy where the objective function is computed for test point parameters surrounding a central point (previous iteration's best result (blue)). If a better objective value is computed (green), this becomes the new center point. The array of test points are parameter values an equal relative distance from the central point, with the distance contracting when no better solution is found..... 12
- Figure 2.1: Geometry of a 5 electrode, 3 contact tumour model (grey) created in COMSOL. Total of 15 contacts, each with separately programmable input waveforms highlighted by different colours. The tumour is surrounded by normal tissue. 28
- Figure 2.2: Objective function value for starting random parameters and final minimized objective value for 50 runs with different random starting parameters. 36
- Figure 2.3: Average temporal electric field maps and corresponding animations of field coverage over time for (a) 2, 3, 4, and 5 optimally placed electrodes in cross sections of corresponding maximum tumour volumes (black circle). (b) 5-electrode configuration with no phase shifting (centre, upper left, bottom right: 2 V amplitude stimulating electrodes, upper right and bottom left: 0 V ground electrodes). 2, 3, and 4 electrode figures with no phase shifting can be found in Appendix C (Figure C.1). (c) Electric field volume histogram of the tumour volume (cm³) receiving at least a certain temporal average electric field value (V/cm) for both optimized phase shift and no phase shift cases..... 39
- Figure 2.4: Maximum treatable tumour diameter (95% coverage of 95% of prescription 1 V/cm) for 2, 3, 4, 5, 6 and 7 single contact electrodes at both 2 V and 4 V input sine wave amplitudes. The data was fit to a function of $d = an + b$, where d is the tumour diameter, n is the number of electrodes, and a and b are fit parameters. With 7 electrodes, at 4 V, with optimal location and phase shift, tumours up to 5.5 cm diameter could be treated..... 41

Figure 2.5: Input voltage sine waves of optimal phase shift configurations with corresponding contact geometries for (a) single contact, (b) 2 contacts, and (c) 3 contacts. Two periods of the waveforms are shown. Contacts of the same colour have the same phase shift, contacts of different hue of the same colour differ slightly in phase shift and different colours differ maximally in phase shift. 43

Figure 2.6: Animations of 1 V/cm isosurface coverage (red) of tumour volume (cyan) over time. Normalized electric field vectors show the field direction over time for both (a) single contact, 5 electrode and (b) 3-contact, 5 electrode models. 44

Figure 2.7: (a) Average temporal electric field maps and corresponding animations of field coverage over time for a 5-electrode tissue sparing example with optimally placed and programmed electrodes. (b) Electric field volume histogram of the percent tumour volume and spared tissue receiving at least a certain temporal average electric field value (V/cm). . 45

Figure 2.8: Time average electric field magnitude (V/cm) for (a) rotating electric field and (b) non-rotating electric field. (Animation includes field vectors)..... 51

Figure 3.1: Pipeline of custom IMT Slicelet in 3D Slicer including the tissue segmentation, smoothing and simplification of segmented volumes (custom module), electrode trajectory planning (custom module), electric field optimization (custom module) and the visualization of the completed optimized treatment plan (custom module). 59

Figure 3.2: Results of electric field optimization for the (a) dual entry six-electrode human model with electrode location results displayed as the 3D geometry of brain (grey), tumour (cyan), electrodes (blue) and active contacts (magenta). The resulting electric fields (b) are displayed on selected axial, sagittal, and coronal cross sections superimposed on the MRI. Further numerical results of optimal phase shift, voltage amplitude, and electrode trajectories can be found in Appendix D (Figure D.2). Results of electric field optimization for the (c) six-electrode single entry human model with 3D geometry and (d) resulting electric fields displayed on selected axial, sagittal and coronal cross sections superimposed on the MRI. Further numerical results of optimal phase shift, voltage amplitude, and electrode trajectories can be found in Appendix D (Figure D.3). 68

Figure 3.3: Results of electric field optimization for the four-electrode dual entry CT phantom model. Electrode location results displayed as (a) 3D geometry of brain (grey), tumour (cyan), electrodes (blue) and active contacts (magenta). Numerical electric field coverage results are displayed as the (b) EVH of tumour coverage, and (c) resulting electric fields are displayed on selected axial, coronal and sagittal cross sections superimposed on the phantom MRI. Further numerical results of optimal phase shift, voltage amplitude, and electrode trajectories can be found in Appendix D (Figure D.4)..... 69

Figure 3.4: Robotic electrode implantation setup including (a) the Neuromate[®] robot with Mayfield[®] head frame and Neurolocate[™] fiducial apparatus attached, and the workstation running the Neuroinspire[™] electrode implantation planning system. (b) Phantom skull housing the brain phantom attached to the head frame with robot moved into Neurolocate[™] registration position. (c) Cannula placement through drilled hole in skull at registered implant trajectory and depth. (d) CT imaging setup of post-implantation of electrodes and (e) the resulting CT image of the six implanted electrodes in the axial plane showing the four stimulating electrodes (top) and the two measurement electrodes (bottom). 70

Figure 3.5: (a) Post-implantation phantom with four electrodes stimulated with four-channel waveform generator, connected to five contacts per electrode (20 total stimulating contacts), and two additional measurement electrodes. (b) Simulated geometry of electrode construct with measurement contacts highlighted in different colours. (c) Voltage measurement and simulation results, with colours corresponding to measurement contacts on electrode geometry, for various stimulation types (1: Full 20 contact stimulation, 2-5: 19 contact stimulation with corresponding electrode contact replaced with measurement prong, and 6: 16 contact stimulation with all middle contacts replaced with measurement prongs). (d) Sagittal slice of post-operative treatment planning results with electric field superimposed on the CT and implanted electrodes projections (white) and tumour (cyan)..... 72

Figure 4.1: *In vitro* electrical conductivity measurement (a) circuit diagram with waveform generator programmed to V_{prog} and internal impedance Z_0 , connected to the *in vitro* setup with impedance Z , voltage across the dish of V_{meas} , and electric field map simulated from the (b) geometry of the *in vitro* setup. 85

Figure 4.2: Custom designed printed circuit board (PCB) including (a) three stimulating electrode wells labelled “Electrode A”, “Electrode B” and “Electrode C”, and a Sham well. Each well is individually stimulated via the Signal In connector (white) or can be connected to other wells to provide identical stimulation using the corresponding links (A/B Link, A/C Link, B/C Link). Four Platinum Iridium wire electrodes are included in each well, located 6.3 mm from the center. (b) PCB fitted to the 24-well plate and connected to a 4-channel waveform generator with unique stimulation delivered to each electrode in well “Electrode A”. The A/B Link is connected in this case to provide identical stimulation to the top two wells. (c) The wire electrodes extend below the PCB, with a length that touches the bottom of the well..... 90

Figure 4.3: Summary of *in vitro* experiment designs, beginning with (a) 200 kHz rotating electric fields at magnitudes of 1, 1.5 and 2 V/cm, to determine the cell survival curve. Voltage and phase parameters were optimized for electric field coverage at the corresponding magnitude and homogeneity to the central 3 mm radius. Rotating fields were delivered with different voltage waveforms $V(t) = A\sin 2\pi ft - \phi n$ to each electrode ($n=1,2,3,4$), where A is the voltage amplitude, t is time, f is the frequency, and ϕn is the phase shift. Experiment (b) compares field rotation to no rotation by grounding (G) two adjacent electrodes and (c) compares a different rotating field frequency of 10 kHz, all with voltage configurations optimized to cover the central 3 mm radius with 1 V/cm. (d) Destructive interference configurations contain alternating ground (G) and stimulating electrodes: voltage matched (left) or power matched (right) to the rotating scenario, resulting in a field cancellation to 0 V/cm in the center. See Appendix E for animation of this figure..... 92

Figure 4.4: (a) Bioluminescence image after 3 days of 1.5 V/cm average IMT electric fields to the top two wells. Bottom two wells were not stimulated, to provide two sham conditions. (b) The cell survival curve for increasing electric field magnitudes. Data is plotted as the mean \pm standard error in blue, and the data was fit to a linear quadratic model $S = Ae - \alpha E + \beta E^2 - 1 + 1$ in black ($R^2=0.95$). 93

Figure 4.5: Mean of the BLI peak signal normalized to sham \pm standard error, proportional to the cell survival, for the cases of constructive interference 200 kHz rotating fields (0.53 ± 0.03 , $n=12$), 200 kHz non-rotating (0.55 ± 0.06 , $n=12$), 10 kHz rotating fields (0.49 ± 0.04 ,

n=12), and destructive interference 200 kHz voltage matched non-rotating fields (0.99 ± 0.02 , n=12).....	95
Figure 4.6: Mean of the BLI peak signal normalized to sham \pm standard error, proportional to the cell survival, for the cases of constructive interference 200 kHz rotating fields (0.47 ± 0.04 , n=6) and destructive interference power matched (0.66 ± 0.03 , n=6).....	96
Figure C.1: Average temporal electric field maps for optimized 2-5 electrodes configurations with no phase shifting	131
Figure D.1: Custom IMT Slicelet design including (a) the numbered pipeline, (b) the smoothing module, (c) the electrode implantation module, and (d) the optimization module.	132
Figure D.2: Treatment planning system full visualization layout of optimized plan results for the human dual entry model including phase shift and voltage amplitude programming, electrode insertion and tip coordinates, the interactive 3D brain, tumour, and electrode models, the EVH, and the axial, sagittal and coronal interactive slice views of the electric field on the MRI.....	133
Figure D.3: Treatment planning system full visualization layout of optimized plan results for the human single entry model including phase shift and voltage amplitude programming, electrode insertion and tip coordinates, the interactive 3D brain, tumor, and electrode models, the EVH, and the axial, sagittal and coronal interactive slice views of the electric field on the MRI.....	134
Figure D.4: Treatment planning system full visualization layout of optimized plan results for the phantom CT dual entry model including phase shift and voltage amplitude programming, electrode insertion and tip coordinates, the interactive 3D brain, tumour, and electrode models, the EVH, and the axial, sagittal and coronal interactive slice views of the electric field on the MRI.....	135
Figure E.1: Ratio of programmed to measured voltage for 24-well, 4 electrode <i>in vitro</i> scenarios including different volumes of DMEM, two wells linked together, and two stimulating electrodes.....	138

Figure E.2: Cell viability comparison between patient derived cell line GBM 23 and GBM 25. Mean of the BLI peak signal normalized to sham \pm standard error, for the cases of constructive interference 200 kHz rotating fields (0.58 ± 0.05 , n=6 vs. 0.48 ± 0.03 , n=6), 200 kHz non-rotating (0.69 ± 0.06 , n=6 vs. 0.40 ± 0.07 , n=6), and 10 kHz rotating fields (0.54 ± 0.07 , n=6 vs. 0.43 ± 0.05 , n=6), and destructive interference 200 kHz voltage matched non-rotating fields (0.97 ± 0.04 , n=6 vs. 1.01 ± 0.03 , n=6).....139

List of Appendices

Appendix A – Permission to Reproduce Content	112
Appendix B – Supplemental Materials for Chapter 1	121
Appendix C – Supplemental Materials for Chapter 2	129
Appendix D – Supplemental Materials for Chapter 3	132
Appendix E – Supplemental Materials for Chapter 4	136
Appendix F – IMT Planning System (IMTPS) User Guide	140

List of Abbreviations

BBB	Blood-brain barrier
BLI	Bioluminescence imaging
DBS	Deep brain stimulation
DIPG	Diffuse intrinsic pontine glioma
CSF	Cerebrospinal fluid
CT	Computed tomography
DAMP	Damage-associated molecular patterns
DMEM	Dulbecco's modified eagle medium
DNA	Deoxyribonucleic acid
EDTA	Ethylenediaminetetraacetic acid
EVH	Electric field volume histogram
GBM	Glioblastoma
GUI	Graphical user interface
HRR	Homologous recombinational repair
IMT	Intratumoural modulation therapy
IRE	Irreversible electroporation
MRI	Magnetic resonance imaging
OAR	Organ at risk

PCB	Printed circuit board
SEEG	Stereoelectroencephalography
tDCS	Transcranial direct current stimulation
tACS	Transcranial alternating current stimulation
TMZ	Temozolomide
TTFields	Tumour treating fields

Chapter 1

1 General Introduction

1.1 Motivation and Overview

Glioblastoma (GBM) is the most aggressive and common type of primary brain cancer with a 5-year relative survival ranging from 2-14% depending on patient age^{1,2}. Despite surgical resection, chemotherapy, and radiation as standard treatment options, the median survival of GBM is 12-14 months^{1,2}. The aggressiveness of these tumours and delicate surrounding structures contribute to the difficulty to control. Other primary brain cancers, such as pediatric Diffuse Intrinsic Pontine Glioma (DIPG), that are located on or near the brainstem are especially hard to control with existing treatment options. Children diagnosed with DIPG have a 2-year survival rate of less than 10% with radiation as the main treatment option, as surgical resection of diffuse disease on the brainstem is not possible and traditional chemotherapy strategies are ineffective^{3,4}. With poor survival outcomes even with the three core treatment options, new modalities are needed to improve survival and patient quality of life.

1.2 Electric Field Theory

Charged particles intrinsically exhibit electric fields, with their magnitude and direction defining the force of attraction or repulsion exerted on surrounding charges. Electric fields are vector quantities that depend on the location in three-dimensional space \mathbf{x} , and the time t , expressed as $\mathbf{E}(\mathbf{x}, t)$. The electric potential $V(\mathbf{x}, t)$ is a location and time dependent quantity defining the energy per unit charge. The electric field and potential are closely related (1.1), where known electric potentials can be used to compute the electric field.

$$\mathbf{E}(\mathbf{x}, t) = -\nabla V(\mathbf{x}, t) \quad (1.1)$$

The electric potential, also referred to as voltage, is an important consideration for medical electric fields, where voltages, and hence electric fields, are applied to biological tissues with either voltage or current driven sources. Permittivity and electrical

conductivity are material properties that influence how electric fields behave. Permittivity, alternatively termed the dielectric constant ϵ , represents a material's ability to store energy, and is a quantity relating the electric field with the charge density $\rho(\mathbf{x}, t)$ in Gauss' law (1.2)⁵.

$$\nabla \cdot \epsilon \mathbf{E}(\mathbf{x}, t) = \rho(\mathbf{x}, t) \quad (1.2)$$

Gauss' law can also be expressed in terms of the electric flux density $\mathbf{D}(\mathbf{x}, t)$, which describes the electric charge over unit area (1.3).

$$\mathbf{D}(\mathbf{x}, t) = \epsilon \mathbf{E}(\mathbf{x}, t) \quad (1.3)$$

In the presence of alternating electric fields, the permittivity is a complex quantity with real and imaginary parts that are frequency dependent. The capability of a material to conduct electric currents is represented by the electrical conductivity σ , and relates the electric field with the current density through Ohm's law (1.4), where $\mathbf{J}(\mathbf{x}, t)$ is the location and time dependent current density⁵.

$$\mathbf{J}(\mathbf{x}, t) = \sigma \mathbf{E}(\mathbf{x}, t) \quad (1.4)$$

The permittivity ϵ and conductivity σ described so far have been scalar quantities, which are used for isotropic media. While this assumption and simplification are applicable, in most cases, it is noted that these simplifications arise from more complicated anisotropic definitions. For anisotropic cases where the electrical properties have directional components, the permittivity and conductivity are represented as tensors, redefining Gauss' law to (1.5) and Ohm's law to (1.6).

$$\mathbf{D}(\mathbf{x}_i, t) = \epsilon_{ij} \mathbf{E}(\mathbf{x}_j, t) \quad (1.5)$$

$$\mathbf{J}(\mathbf{x}_i, t) = \sigma_{ij} \mathbf{E}(\mathbf{x}_j, t) \quad (1.6)$$

Biological tissues exposed to electrical stimulation represent parallel circuit models containing resistive and capacitive components⁵. The absolute value of tissue impedance Z can therefore be defined as (1.7), where R is the resistance (conductivity dependent), f

is the frequency, and C is the capacitance (permittivity dependent) and used to relate current I to the voltage V (1.8).

$$Z = (R^{-2} + (2\pi fC)^2)^{-0.5} \quad (1.7)$$

$$V = ZI \quad (1.8)$$

The biological circuit becomes more complex when multiple voltage source electrodes are included, adding parallel components to the circuit. When this is the case, it becomes more logical to use the admittance Y , which is the reciprocal of the impedance. The components from the multiple sources are expressed as an admittance matrix, which relates the current and voltage of each terminal source (1.9).

$$\begin{bmatrix} I_1 \\ \vdots \\ I_n \end{bmatrix} = \begin{bmatrix} Y_{11} & \cdots & Y_{1n} \\ \vdots & \ddots & \vdots \\ Y_{n1} & \cdots & Y_{nn} \end{bmatrix} \begin{bmatrix} V_1 \\ \vdots \\ V_n \end{bmatrix} \quad (1.9)$$

While the electric field in tissues can be summarized using macroscopic electrical properties, on the microscopic level the cell membrane and cytoplasm each have their own electrical properties, governing the electric field through each layer⁵⁻⁷. Both electrical conductivity and permittivity are dependent on the frequency of the external electric stimulation applied to the sample. Microscopic cell properties shed light on the mechanisms of applied electric fields and how the stimulation frequency and amplitude impact the normal functioning of intercellular structures and membrane potentials. Low frequency fields (~50 Hz) do not penetrate the cell membrane, while higher frequency fields (~1 MHz) completely pass through the membrane, leading to uniform field within extracellular and intercellular space⁵. For intermediate frequencies in the kHz range, increasing the frequency increases the intercellular electric field until a peak field is reached surpassing the extracellular field, then decreases to the extracellular field strength⁸. Membrane and intercellular electrical conductivity and permittivity differ between cell types, especially cancerous cells, where the unique electrical characteristics could be exploited for cancer cell targeted therapy⁹.

Macroscopic isotropic properties, derived from experimental data¹⁰⁻¹⁴, are important for mapping electric fields within tissue to determine optimal treatment scenarios. Methods for non-invasively determining these properties include the use of magnetic resonance imaging (MRI) to map the electrical conductivity and permittivity in patient brains, making possible more patient-specific electrotherapy treatments¹⁵.

1.3 Electric Fields in Medicine

Electric fields have various applications in medicine from treating neurological disorders with deep brain stimulation (DBS), transcranial direct or alternating current stimulation (tDCS, tACS), to treating tumours with irreversible electroporation (IRE), radiofrequency ablation, tumour treating fields (TTFields), or preclinical intratumoural modulation therapy (IMT), the topic of this thesis (Table 1.1). The frequency range and amplitude of such electric fields are highly influential in the treatment capabilities and mechanisms, as well as the electric properties of the impacted tissues.

Table 1.1: Stimulation parameters for electrotherapy devices including voltage, frequency, and average electric field.

Medical Device	Electrode Placement	Disease	Mechanism	Time	Voltage	Frequency	Electric Field
Tumour Treating Fields (TTFields) ^{16,17}	External	Cancer (GBM)	Anti-Mitotic?	Continuous: >18 hours/day	50 V	100-500 kHz	1-3 V/cm
Transcranial Direct Current Stimulation (tDCS) ¹⁸⁻²¹		Neurological Disorders	Neuron Firing Rate	Minutes: 20-30 min	Current 1-2 mA	N/A	<0.01 V/cm
Transcranial Alternating Current Stimulation (tACS) ^{22,23}			Neuronal Entrainment			10-250 Hz	
Radiofrequency Ablation ^{24,25}	Internal	Cancer	100°C Thermal Ablation via Ohmic Heating	Minutes: 10-15 min	20-25 V	450-550 kHz	75 V/cm
Microwave Ablation ^{24,26-28}		Cancer	100°C Thermal Ablation via Dielectric Heating		70 V	0.915-2.45 GHz	10 V/cm

Irreversible Electroporation (IRE) ²⁹	Cancer	Irreversible Membrane Permeabilization	Seconds: 50-100 total pulses	1000-3000 V	100 μ s pulse width	300-1500 V/cm
Deep Brain Stimulation (DBS) ^{30,31}	Movement/Neurological Disorders (Parkinson's, Epilepsy)	Neuronal Entrainment	Continuous	2-4 V	130-185 Hz 60-450 μ s pulse width	1-2 V/cm
Intratumoural Modulation Therapy (IMT) ³²⁻³⁴	Cancer (GBM, DIPG)	Anti-Mitotic?	Continuous	1-4 V	100-500 kHz	1-3 V/cm

1.3.1 Tumour Treating Fields

One recent advancement in the control of GBM is using low intensity alternating electric fields to interfere with tumour progression^{17,35-37}. This technique, termed Tumour Treating Fields (TTFields), uses two electrode array pairs placed on the shaved scalp to deliver alternating electric fields in the anterior-posterior and left-right orientation. Sinusoidal waveforms are continuously applied to the electrodes from a waveform generator with a maximum amplitude of 50V at 200 kHz, which alternate between the AP and LR pairs depending on the treatment plan³⁸. TTFields began with preclinical investigations into intermediate frequency (100-500 kHz) electric fields, thought previously to have no medical benefits. These early *in vitro* and *in vivo* studies deemed low intensity electric fields from 1-3 V/cm effective at non-thermally causing arrest in cancer cell proliferation in a frequency and field strength dependent manner^{39,40}. TTFields effects on cancer cells have since been corroborated by other groups and shown to have additive effects when combined with Temozolomide (TMZ), a standard of care chemotherapeutic agent for GBM^{41,42}.

Clinical trials of TTFields using the Optune® (NovoTTF-100A) device shown comparable results to standard of care chemotherapy⁴³, and significant progression-free and overall survival when TTFields was combined with TMZ compared to TMZ alone⁴⁴. Based on results of the phase 3 clinical trials, TTFields became an FDA approved treatment for GBM. An analysis of early clinical implementation of TTFields from 2011 to 2013 highlighted no unexpected adverse events and overall survival that surpassed

those reported in the clinical trials⁴⁵. Case studies on tumour recurrence suggest that underdosed regions are more susceptible to recurrence, and adjustment of treatment parameters could improve the response of local recurrence⁴⁶. Patient compliance with wearing the device, as well as electric field strength to the tumour, were both indicators of overall and progression free survival⁴⁷. The main drawback to the use of the external nature of TTFields, evident from patient compliance, is that patients must maintain a shaved scalp and wear the device for at least 18 hours a day while also carrying the accompanying waveform generator.

1.3.2 Mechanism of Tumour Treating Fields

While the mechanism is not a central part of this thesis, a brief overview of potential mechanisms has been included, with a detailed literature review included in Appendix B. The original hypothesized mechanism of action of TTFields was purely anti-mitotic, as there was an observed cell selectivity of rapidly dividing tumour cells compared to normal cells³⁹. Early studies observed two main anti-mitotic mechanisms involving spindle fiber formation and dielectrophoresis in telophase^{39,40,48}. During metaphase, chromosomes align and the mitotic spindle forms through microtubule polymerization of polar subunits (tubulin dimers) to pull sister chromatids to opposing poles. In the presence of an external electric field, the polar tubulin dimers are thought to follow the external electric field instead properly polymerizing and depolymerizing, leading to cell death⁴⁸. The second anti-mitotic observation occurs in anaphase, where septin proteins fail to localize to the mitotic spindle, impacting the cleavage furrow ring assembly^{49,50}. Another anti-mitotic action involves dielectrophoresis in telophase, where the non-uniform electric field within the dividing cell is focused at high intensity on the cleavage furrow. This non-uniformity causes dielectrophoretic forces to pull charged and polar molecules to the furrow^{37,40,48,51}. While anti-mitotic mechanisms were the original hypotheses, it has since been established that many alternative intracellular mechanisms are at play (Figure 1.1). Various reports have found TTFields reduce tumour DNA repair, reduce tumour cell migration, impact autophagy, enhance anti-tumour immunity and promote immunogenic cell death, and increase cell membrane permeability^{37,52-56}.

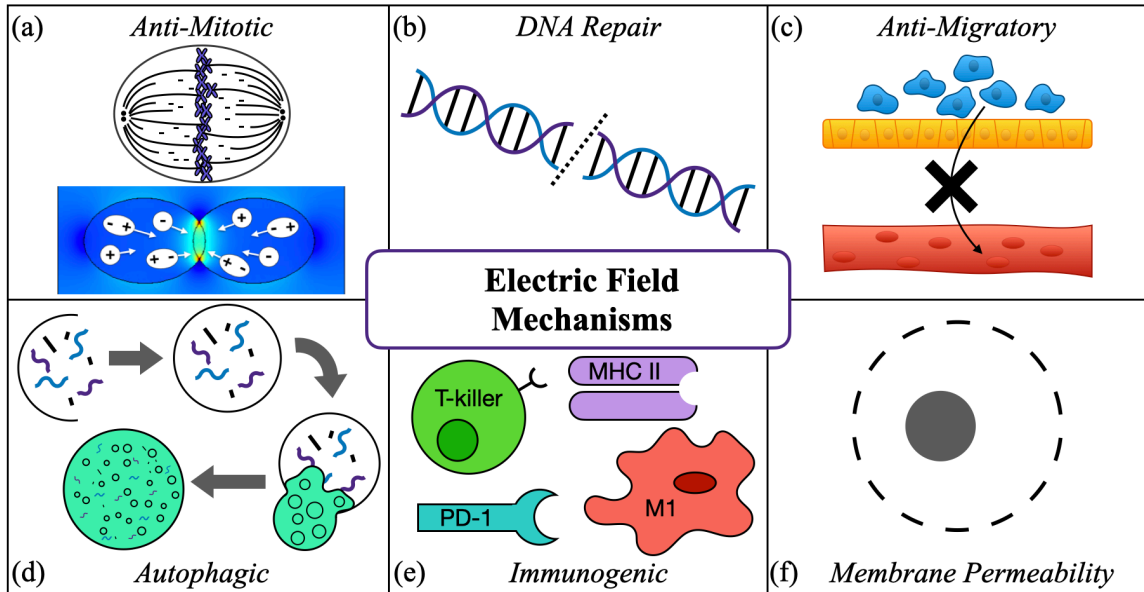


Figure 1.1: Summary of proposed mechanisms of action for tumour treating electric fields. TTFields have been found to be (a) anti-mitotic, (b) to decrease DNA repair, (c) to decrease cell migration, (d) to promote autophagy, (e) to promote an immune response, and (f) to increase membrane permeability and blood brain barrier breaching.

1.3.3 Tumour Ablation Techniques

Tumour ablation represents an alternative treatment option for patients whose primary treatments of surgery, chemotherapy and radiation are not appropriate. Thermal tumour ablation techniques including radiofrequency and microwave ablation work by destroying tumour cells with heat^{57,58}. An electrode is inserted into the tumour volume, typically non-invasively with the help of ultrasound, and radiofrequency or microwave energy is applied to raise the temperature of the tumour tissue past lethal limits. Thermal ablation is most commonly used for liver cancers, but can also be used to treat kidney, bone, and pancreas. The main drawback to thermal ablation is the non-selective destruction of nearby tissue, which is detrimental for nearby critical structures.

High intensity electric fields (~ 1000 V/cm) have the capacity to ablate tumours by causing holes in the cell membrane that cannot be repaired, leading to cancer cell death. This technique, irreversible electroporation (IRE), is a fairly new strategy developed in

the past decades, that uses multiple electrodes temporarily implanted into the tumour to deliver primarily non-thermal electric fields^{59,60}. IRE has the potential to overcome drawbacks of thermal ablative techniques impacting nearby normal critical structures. With IRE still in the early stages, treatment strategies are being investigated to determine stimulation settings and electrode pair combinations to optimally cover tumour volumes^{61,62}. Both thermal and non-thermal ablation are similar in their use of temporarily implanted electrodes to deliver electric fields, but their high intensity has its limitations on applications with nearby critical structures.

1.3.4 Non-Cancer Applications

Electric fields of low frequency (~ 100 Hz) can be used to treat neurological disorders including Parkinson's disease, dystonia, epilepsy, and essential tremor through deep brain stimulation (DBS) by regulating neuronal function⁶³⁻⁶⁵. In DBS, electrodes are surgically placed with mm precision at the desired brain region where permanent implantation allows for continuous and adjustable stimulation. Multi-element electrodes are provided with stimulation through a pulse generator implanted subcutaneously near the clavicle. The intensity and spatial configuration of the stimulation is adjusted until the patient's symptoms are resolved.

The main concern with the design of new DBS electrodes is ensuring the charge density on the electrode surface does not exceed $30 \mu\text{C}/\text{cm}^2$, the threshold for tissue damage⁶⁶. The charge density is inversely proportional to surface area, so new designs for electrodes with small directional contacts must consider the charge density⁶⁷. Improvements to the design of DBS electrodes are of current interest to improve efficacy⁶⁷⁻⁶⁹, where the impacts of tissue impedance has been deemed an important consideration⁷⁰⁻⁷².

Non-invasive methods to treat neurological disorders include tDCS and tACS, where electrodes are placed on the patient's scalp to deliver currents across the brain¹⁸⁻²³. These methods use either direct current (tDCS) or alternating current (tACS) waveforms that result in electric field magnitudes to the brain of under 0.01 V/cm, much lower than DBS.

1.4 Electric Field Computer Simulations

An important consideration with electrotherapy is the delivered electric field and current density to the brain, quantities that shape treatment planning and efficacy. For partial differential equations without simple analytical solutions, such as the electric fields in complex geometries, numerical methods are required to approximate the solution in space and time. Finite element method is one such numerical approach which discretizes the boundary value problem on a non-uniform mesh. For three dimensional problems, a non-uniform tetrahedral mesh is most commonly used, with smaller mesh elements and more discretization points in areas of greater geometrical change. For electric field finite element solvers, Gauss' law (1.2,1.3), Ohm's law (1.4), and continuity (1.10) govern the electric field computation.

$$\frac{\partial \rho(\mathbf{x}, t)}{\partial t} + \nabla \cdot \mathbf{J}(\mathbf{x}, t) = 0 \quad (1.10)$$

Boundary conditions including the voltage at terminal boundaries, electrical insulation, and maintaining $\mathbf{n} \cdot \mathbf{J} = 0$ on boundaries (\mathbf{n} is the boundaries normal vector) are required for computation in addition to known electrical conductivity and permittivity. Computer modelling is a useful and commonly used tool for analyzing the electric field distribution in medical applications such as TTFIELDS, DBS, and IRE, which can help shape treatment techniques and parameters.

Electric field simulations have played a role in the development of the external TTFIELDS device, and began with cell modelling in metaphase and telophase investigating the dependence of cellular electric field on electrical properties and frequency⁸. The electric field within the cell is inversely proportional to the intercellular conductivity, proportional to the membrane permittivity, and independent of the membrane conductivity or intercellular permittivity at 200 kHz⁸. Simulations of cells in telophase showed that the electric field at the cleavage furrow peaked at 200 kHz, with frequency dependence also observed in single cells⁸. Single and dividing cell modelling has also been used to study the potential mechanisms of TTFIELDS including the disruption of mitotic spindle formation, dielectrophoresis and impacts on the cell membrane⁷³⁻⁷⁵. Frequency and division axis orientation impact on dielectrophoretic forces during telophase and

cytokinesis were simulated and used to create an equivalent circuit model of cells undergoing mitosis⁷⁵, supporting the dielectrophoretic hypothesis. Other simulation cell studies on spherical and realistic GBM cells have found weak electric field strength within the cytoplasm raises question to intercellular mechanisms, and thermal distributions supported the hypothesis that thermal damage is not a mechanism of action⁷³. Induced membrane potential shows promise as a possible mechanism based on recent modelling, which finds previous hypothesized mechanisms of mitotic spindle formation disruption and dielectrophoresis to be lacking in theoretical support⁷⁴.

The modelling of the electric field distribution within the patient brain has been used to shape treatment parameters including electrode array layouts and stimulation programming⁷⁶. The impact of electrical properties, tumour location, and necrotic core presence on the electric field have been investigated in realistic brain and tumour models⁷⁷⁻⁷⁹. Electrical conductivity of various brain tissues has the greatest impact on electric field, with the skull acting as an insulator which greatly reduce the electric field magnitude within the brain⁷⁷⁻⁷⁹. This led to the hypothesis and subsequent simulation support that a craniectomy could be applied to improve electric field to tumours located near the skull by 60-70%⁸⁰. The necessity of time consuming realistic brain tissue segmentations has been investigated by comparing field strength to a simplified brain model, showing minimal difference between realistic and simplified brain models⁸¹. Numerical simulation-based analysis has been expanded to analyze the treatment planning system⁸² and clinical trial data, where patient compliance and dose intensity above 1 V/cm were indicators of overall survival⁴⁷.

Electrotherapy techniques using implanted electrodes are also studied computationally, including DBS tissue heating^{83,84}, impedance over time⁸⁵, and the impact of DBS electrode design on the electric field⁸⁶⁻⁸⁸. Ensuring that DBS electrodes are delivering only safe with minimal tissue heating (<0.8°C directly adjacent electrode contact⁸³) is an important consideration when designing electrodes, and can be modelled with finite element solvers similar to the electric field. For multi-contact electrodes, the farther the separation between active contacts, the lower the heat produced⁸⁴. Electric field simulations of novel electrode designs are essential in determining the treatment

capabilities and safety profiles^{86–88}. Electric fields, electric potential and current density from various electrode designs have also been investigated computationally in realistic human head models for transcranial direct current stimulation^{89,90} and radiofrequency ablation^{91–93}. While there are planning systems for irreversible electroporation considering thermal effects⁹⁴ and electric field distributions^{62,95}, there is no planning system for IMT.

1.5 Numerical Optimization

To determine optimal IMT electrode trajectories and stimulation parameters in this thesis, computer simulations of the electric field are considered in an optimization algorithm. Optimization of elaborate functions that do not have analytic solutions, including functions dependent on computer simulation results⁹⁶, require numerical methods to find the optimal solution^{97,98}. The main components of an optimization algorithm are the objective function, which is to be minimized, and the optimization strategy. Common strategical categories include descent⁹⁹, evolutionary, probabilistic and pattern search methods⁹⁶. The characteristics of the objective function including continuity and number of minima determine the strategy that is best for the problem at hand. Descent methods, commonly gradient descent, are suited for problems where the objective function is continuous and differentiable. For gradient descent a local minimum is found by computing the negative gradient of the objective function as the search direction for the next iteration⁹⁹. While descent methods are favourable for being fast and efficient, problems that contain discrete objective functions that are not differentiable require alternate methods. Metaheuristic approaches look to find the global minimum of an optimization problem and include classes such as evolutionary and probabilistic algorithms. The genetic algorithm (evolutionary) and simulated annealing (probabilistic) are common metaheuristic approaches derived from natural selection and the annealing process in metallurgy respectively⁹⁶. These techniques are well suited for problems that require finding the global minimum of a discrete problem, where the objective function can be evaluated quickly. Pattern or direct search methods (Figure 1.2) are derivative free optimization strategies that iteratively compare objective function values to find a local minimum⁹⁶. These methods can be faster and simpler to implement compared to

metaheuristic approaches, but the incomplete search of parameter space can mean the global minimum is missed. Pattern search is the chosen strategy for IMT applied in this work, while optimization strategies including gradient descent and direct search methods have been applied to simulation based problems in electrotherapy for DBS⁶⁷, TFields¹⁰⁰ and electrode placement and programming for electro-chemotherapy¹⁰¹.

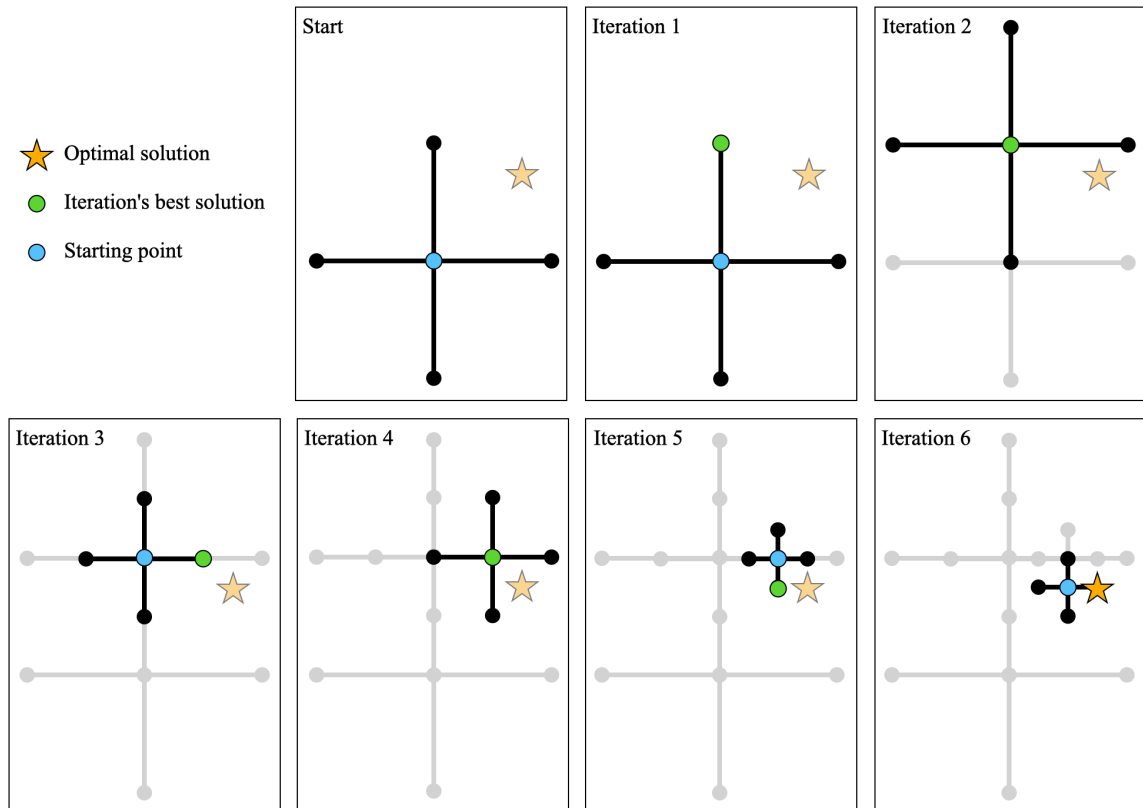


Figure 1.2: Pattern search optimization strategy where the objective function is computed for test point parameters surrounding a central point (previous iteration's best result (blue)). If a better objective value is computed (green), this becomes the new center point. The array of test points are parameter values an equal relative distance from the central point, with the distance contracting when no better solution is found.

1.6 Intratumoural Modulation Therapy

Intratumoural Modulation Therapy (IMT) is a proposed method of applying low intensity electric fields directly to brain tumour regions using multiple implanted bio-electrodes³²⁻

³⁴. These electrodes would be permanently implanted within and adjacent to the patient brain tumour where an implantable waveform generator would supply the ideal stimulation parameters to the electrodes. This method would allow the electric fields to be applied with lower voltage amplitude (<10 V) compared to external TTFields methods which require 50V stimulation to penetrate the insulating skull (Table 1.1). Additionally, IMT would allow for localized electric field coverage to tumours anywhere in the brain, including near and on the brainstem, a location not reachable with external devices. With IMT being a novel treatment modality, the ideal stimulation parameters, placement configuration and electrode design to best allow for custom treatment of patient brain tumours is still unknown.

Early *in vitro* IMT investigations considered GBM cells versus normal post-mitotic neurons exposed to 130 Hz square pulses of 4 V amplitude and 90 μ s pulse width³². Neurons remained unaffected by IMT, while GBM cells were significantly impacted by IMT with a 56% decrease in cell viability after 96 hours compared to sham conditions³². To ensure IMT would not cause unwanted neuronal entrainment from the 130 Hz DBS frequency, the frequency was increased to 200 kHz.

In this second investigation, patient derived GBM cells (n=3), F98 GBM cells (n=3) and post-mitotic primary neurons (n=4) were exposed *in vitro* to either ± 2 V, 200 kHz sinusoidal waveforms for 72 hours, Temozolomide chemotherapy (TMZ) or both³³. Reduction of cell viability for patient derived cells was observed as 83% viability for TMZ, 65% viability for IMT, and 46% viability for combination TMZ+IMT. Flow cytometry determined the percentage of apoptotic/dead cells as 15% for the sham condition, 28% for TMZ, 39% for IMT and 74% for combination TMZ+IMT. Rodent F98 GBM cells showed 55% cell viability *in vitro*, and 20% tumour volume reduction *in vivo* after one week of IMT delivered to one side of a bilateral tumour model (n=15). Primary neurons were not impacted by IMT, and computer simulations of the *in vivo* single electrode construct showed 24% of the tumour core above 1 V/cm³³.

IMT was also investigated *in vitro* for efficacy on patient derived DIPG cells (n=3), where IMT reduced cell viability to 52%, with flow cytometry viable to non-viable ratios

of 6:1 for sham conditions and 1.5:1 for IMT³⁴. When multi-modality paradigms including IMT, TMZ, and radiotherapy (RT) were applied, the cell viability was reduced to 81% for TMZ, 72% for RT, 59% for combination TMZ+RT, 44% for IMT, 40% for combination IMT+TMZ, 35% for combination IMT+RT, and 21% for IMT+TMZ+RT³⁴. The significant decrease in cell viability with IMT alone and in combination with chemotherapy and radiation highlight the potentials for improved outcomes with multi-modality treatment for DIPG. Computer simulations of the *in vitro* single electrode model yielded only 6% of the *in vitro* dish was exposed to at least 1 V/cm electric field, prompting the switch to multiple electrodes to increase electric field coverage.

All previous IMT preclinical studies used a single stimulating electrode with limitations in electric field coverage to mm scale volumes. Moving from preclinical to clinical scale tumours would require a boost in electric field coverage while maintaining the low input voltage necessary for intratumoural electrodes. This will require multiple electrodes, but the number and design of such electrodes, the optimal stimulation parameters and trajectories remain unknown. If IMT is to progress towards clinical implementation, there needs to be a way to determine optimal treatments parameters on a patient-specific basis.

1.7 Research Hypothesis

We hypothesize that planning and validating multi-electrode spatiotemporally dynamic IMT treatments using computer simulation and numerical optimization strategies will improve electric field coverage to brain tumours, with the development of novel planning systems providing a necessary step towards clinical implementation.

1.8 Research Objectives

In Chapter 2, multi-electrode IMT was investigated *in silico* and an optimization algorithm pioneered to maximize electric field coverage to human scale spherical tumour volumes. It was predicted the size of tumour that would be coverable for between 2 and 7 electrodes with multiple separately programmable contacts. Phase shifting of input waveforms to produce spatiotemporally dynamic fields was investigated theoretically for

the first time for the impact on electric field coverage over time. Optimal configurations and programming for between 2 and 7 electrodes were established for spherical tumours.

In Chapter 3, a novel treatment planning system for IMT was developed to model and optimize the electric field to patient-specific tumour volumes. Modules responsible for segmentation, smoothing, electrode trajectory planning, optimization, and visualization of electric fields were amalgamated into a planning system within 3D Slicer^{102–104} with substantial improvements to computation time. The planning system pipeline was validated with robot-assisted multi-electrode implantation on a brain phantom where post-implantation imaging was used to implement the post-operative planning pipeline. Electrodes were stimulated with planned programming and the voltage measured at various points to validate the delivered electric field.

In Chapter 4, the IMT treatment planning system was applied to design *in vitro* experiments that were carried out on GBM cells to test the efficacy of rotating electric fields and the impact of field frequency and optimization on cell survival. The dose vs. cell survival relationship was also determined. Simulations and optimizations were used to design a 4-electrode *in vitro* printed circuit board to employ rotating electric fields. The voltage drop observed within the culture media was used along with simulations to calculate the electrical conductivity of the media at 200 kHz, with simulated voltage drops validated over multiple media volumes and electrode configurations.

Chapter 5 provides a summary of findings, their related limitations and future work that this thesis can support.

1.9 References

1. Nam JY, de Groot JF. Treatment of Glioblastoma. *J Oncol Pract.* 2017;13(10):629-638. doi:10.1200/JOP.2017.025536
2. Nabors LB, Portnow J, Ahluwalia M, et al. Central Nervous System Cancers, Version 3.2020, NCCN Clinical Practice Guidelines in Oncology. *J Natl Compr Cancer Netw.* 2020;18(11):1537-1570. doi:10.6004/jncn.2020.0052
3. Gallitto M, Lazarev S, Wasserman I, et al. Role of Radiation Therapy in the Management of Diffuse Intrinsic Pontine Glioma: A Systematic Review. *Adv*

- Radiat Oncol.* 2019;4(3):520-531. doi:10.1016/j.adro.2019.03.009
4. Long W, Yi Y, Chen S, Cao Q, Zhao W, Liu Q. Potential New Therapies for Pediatric Diffuse Intrinsic Pontine Glioma. *Front Pharmacol.* 2017;8(JUL). doi:10.3389/fphar.2017.00495
 5. Claycomb J, Quoc P, Tran J. Passive Electrical Properties of Living Cells. In: *Introductory Biophysics: Perspectives on the Living State.* Jones and Bartlett Publishers; 2010:127-149.
 6. Nasir N, Al Ahmad M. Cells Electrical Characterization: Dielectric Properties, Mixture, and Modeling Theories. *J Eng.* 2020;2020:1-17. doi:10.1155/2020/9475490
 7. Kotnik T, Miklavčič D. Theoretical evaluation of the distributed power dissipation in biological cells exposed to electric fields. *Bioelectromagnetics.* 2000;21(5):385-394. doi:10.1002/1521-186X(200007)21:5<385::AID-BEM7>3.0.CO;2-F
 8. Wenger C, Giladi M, Bomzon Z, Salvador R, Basser PJ, Miranda PC. Modeling Tumor Treating Fields (TTFields) application in single cells during metaphase and telophase. In: *2015 37th Annual International Conference of the IEEE Engineering in Medicine and Biology Society (EMBC).* IEEE; 2015:6892-6895. doi:10.1109/EMBC.2015.7319977
 9. Al Ahmad M, Al Natour Z, Mustafa F, Rizvi TA. Electrical Characterization of Normal and Cancer Cells. *IEEE Access.* 2018;6:25979-25986. doi:10.1109/ACCESS.2018.2830883
 10. Miklavčič D, Pavšelj N, Hart FX. Electric Properties of Tissues. In: *Wiley Encyclopedia of Biomedical Engineering.* Hoboken, NJ, USA: John Wiley & Sons, Inc.; 2006. doi:10.1002/9780471740360.ebs0403
 11. Latikka J, Kuurne T, Eskola H. Conductivity of living intracranial tissues. *Phys Med Biol.* 2001;46(6):1611-1616. doi:10.1088/0031-9155/46/6/302
 12. Gabriel C, Peyman A, Grant EH. Electrical conductivity of tissue at frequencies below 1 MHz. *Phys Med Biol.* 2009;54(16):4863-4878. doi:10.1088/0031-9155/54/16/002
 13. Latikka J, Eskola H. The Resistivity of Human Brain Tumours In Vivo. *Ann Biomed Eng.* 2019;47(3):706-713. doi:10.1007/s10439-018-02189-7
 14. Stoy RD, Foster KR, Schwan HP. Dielectric properties of mammalian tissues from 0.1 to 100 MHz; a summary of recent data. *Phys Med Biol.* 1982;27(4):501-513. doi:10.1088/0031-9155/27/4/002
 15. Michel E, Hernandez D, Lee SY. Electrical conductivity and permittivity maps of brain tissues derived from water content based on T₁-weighted acquisition. *Magn Reson Med.* 2017;77(3):1094-1103. doi:10.1002/mrm.26193
 16. Wenger C, Miranda PC, Salvador R, et al. A Review on Tumor-Treating Fields (TTFields): Clinical Implications Inferred From Computational Modeling. *IEEE Rev Biomed Eng.* 2018;11:195-207. doi:10.1109/RBME.2017.2765282

17. Swanson KD, Lok E, Wong ET. An Overview of Alternating Electric Fields Therapy (NovoTTF Therapy) for the Treatment of Malignant Glioma. *Curr Neurol Neurosci Rep.* 2016;16(1):8. doi:10.1007/s11910-015-0606-5
18. Zhao H, Qiao L, Fan D, et al. Modulation of Brain Activity with Noninvasive Transcranial Direct Current Stimulation (tDCS): Clinical Applications and Safety Concerns. *Front Psychol.* 2017;8(MAY). doi:10.3389/fpsyg.2017.00685
19. Im C-H, Park J-H, Shim M, Chang WH, Kim Y-H. Evaluation of local electric fields generated by transcranial direct current stimulation with an extracephalic reference electrode based on realistic 3D body modeling. *Phys Med Biol.* 2012;57(8):2137-2150. doi:10.1088/0031-9155/57/8/2137
20. Dmochowski JP, Datta A, Huang Y, et al. Targeted transcranial direct current stimulation for rehabilitation after stroke. *Neuroimage.* 2013;75:12-19. doi:10.1016/j.neuroimage.2013.02.049
21. Dmochowski JP, Datta A, Bikson M, Su Y, Parra LC. Optimized multi-electrode stimulation increases focality and intensity at target. *J Neural Eng.* 2011;8(4):046011. doi:10.1088/1741-2560/8/4/046011
22. Tavakoli A V., Yun K. Transcranial Alternating Current Stimulation (tACS) Mechanisms and Protocols. *Front Cell Neurosci.* 2017;11. doi:10.3389/fncel.2017.00214
23. Herrmann CS, Rach S, Neuling T, Strüber D. Transcranial alternating current stimulation: a review of the underlying mechanisms and modulation of cognitive processes. *Front Hum Neurosci.* 2013;7(MAY). doi:10.3389/fnhum.2013.00279
24. Chang I. Finite Element Analysis of Hepatic Radiofrequency Ablation Probes using Temperature-Dependent Electrical Conductivity. *Biomed Eng Online.* 2003;2(1):12. doi:10.1186/1475-925X-2-12
25. Haemmerich D, Webster JG. Automatic control of finite element models for temperature-controlled radiofrequency ablation. *Biomed Eng Online.* 2005;4(1):42. doi:10.1186/1475-925X-4-42
26. Cheong JKK, Ooi EH, Ooi ET. Thermal and thermal damage responses during switching bipolar radiofrequency ablation employing bipolar needles: A computational study on the effects of different electrode configuration, input voltage and ablation duration. *Int j numer method biomed eng.* 2020;36(9). doi:10.1002/cnm.3374
27. Brace CL. Microwave Ablation Technology: What Every User Should Know. *Curr Probl Diagn Radiol.* 2009;38(2):61-67. doi:10.1067/j.cpradiol.2007.08.011
28. Ji Z, Brace CL. Expanded modeling of temperature-dependent dielectric properties for microwave thermal ablation. *Phys Med Biol.* 2011;56(16):5249-5264. doi:10.1088/0031-9155/56/16/011
29. Aycock KN, Davalos R V. Irreversible Electroporation: Background, Theory, and Review of Recent Developments in Clinical Oncology. *Bioelectricity.* 2019;1(4):214-234. doi:10.1089/bioe.2019.0029

30. Kuncel AM, Grill WM. Selection of stimulus parameters for deep brain stimulation. *Clin Neurophysiol.* 2004;115(11):2431-2441. doi:10.1016/j.clinph.2004.05.031
31. Johansson JD, Alonso F, Wårdell K. Modelling Details for Electric Field Simulations of Deep Brain Stimulation. In: *IFMBE Proceedings*. Vol 68. ; 2019:645-648. doi:10.1007/978-981-10-9035-6_120
32. Xu H, Bihari F, Whitehead S, Wong E, Schmid S, Hebb MO. In vitro validation of intratumoral modulation therapy for glioblastoma. *Anticancer Res.* 2016.
33. Di Sebastiano AR, Deweyert A, Benoit S, et al. Preclinical outcomes of Intratumoral Modulation Therapy for glioblastoma. *Sci Rep.* 2018;8(1):7301. doi:10.1038/s41598-018-25639-7
34. Deweyert A, Iredale E, Xu H, Wong E, Schmid S, Hebb MO. Diffuse intrinsic pontine glioma cells are vulnerable to low intensity electric fields delivered by intratumoral modulation therapy. *J Neurooncol.* 2019;143(1):49-56. doi:10.1007/s11060-019-03145-8
35. Hottinger AF, Pacheco P, Stupp R. Tumor treating fields: a novel treatment modality and its use in brain tumors. *Neuro Oncol.* 2016;18(10):1338-1349. doi:10.1093/neuonc/nov182
36. Gutin PH, Wong ET. Noninvasive Application of Alternating Electric Fields in Glioblastoma: A Fourth Cancer Treatment Modality. *Am Soc Clin Oncol Educ B.* 2012;(32):126-131. doi:10.14694/EdBook_AM.2012.32.122
37. Rominiyi O, Vanderlinden A, Clenton SJ, Bridgewater C, Al-Tamimi Y, Collis SJ. Tumour treating fields therapy for glioblastoma: current advances and future directions. *Br J Cancer.* 2021;124(4):697-709. doi:10.1038/s41416-020-01136-5
38. Lok E, Sajo E. Fundamental Physics of Tumor Treating Fields. In: *Alternating Electric Fields Therapy in Oncology*. Cham: Springer International Publishing; 2016:15-27. doi:10.1007/978-3-319-30576-9_2
39. Kirson ED, Gurvich Z, Schneiderman R, et al. Disruption of Cancer Cell Replication by Alternating Electric Fields. *Cancer Res.* 2004;64(9):3288-3295. doi:10.1158/0008-5472.CAN-04-0083
40. Kirson ED, Dbalý V, Tovaryš F, et al. Alternating electric fields arrest cell proliferation in animal tumor models and human brain tumors. *Proc Natl Acad Sci.* 2007;104(24):10152-10157. doi:10.1073/pnas.0702916104
41. Clark PA, Gaal JT, Strebe JK, et al. The effects of tumor treating fields and temozolomide in MGMT expressing and non-expressing patient-derived glioblastoma cells. *J Clin Neurosci.* 2017;36:120-124. doi:10.1016/j.jocn.2016.10.042
42. Kessler AF, Frömbling GE, Gross F, et al. Effects of tumor treating fields (TTFields) on glioblastoma cells are augmented by mitotic checkpoint inhibition. *Cell Death Discov.* 2018;4(1):77. doi:10.1038/s41420-018-0079-9
43. Stupp R, Wong ET, Kanner AA, et al. NovoTTF-100A versus physician's choice

- chemotherapy in recurrent glioblastoma: A randomised phase III trial of a novel treatment modality. *Eur J Cancer*. 2012;48(14):2192-2202. doi:10.1016/j.ejca.2012.04.011
44. Stupp R, Taillibert S, Kanner A, et al. Effect of Tumor-Treating Fields Plus Maintenance Temozolomide vs Maintenance Temozolomide Alone on Survival in Patients With Glioblastoma. *JAMA*. 2017;318(23):2306. doi:10.1001/jama.2017.18718
 45. Mrugala MM, Engelhard HH, Dinh Tran D, et al. Clinical Practice Experience With NovoTTF-100A™ System for Glioblastoma: The Patient Registry Dataset (PRiDe). *Semin Oncol*. 2014;41(5):S4-S13. doi:10.1053/j.seminoncol.2014.09.010
 46. Turner SG, Gergel T, Wu H, Lacroix M, Toms SA. The effect of field strength on glioblastoma multiforme response in patients treated with the NovoTTF™-100A system. *World J Surg Oncol*. 2014;12(1):162. doi:10.1186/1477-7819-12-162
 47. Ballo MT, Urman N, Lavy-Shahaf G, Grewal J, Bomzon Z, Toms S. Correlation of Tumor Treating Fields Dosimetry to Survival Outcomes in Newly Diagnosed Glioblastoma: A Large-Scale Numerical Simulation-Based Analysis of Data from the Phase 3 EF-14 Randomized Trial. *Int J Radiat Oncol*. 2019;104(5):1106-1113. doi:10.1016/j.ijrobp.2019.04.008
 48. Giladi M, Schneiderman RS, Voloshin T, et al. Mitotic Spindle Disruption by Alternating Electric Fields Leads to Improper Chromosome Segregation and Mitotic Catastrophe in Cancer Cells. *Sci Rep*. 2016;5(1):18046. doi:10.1038/srep18046
 49. Wong ET, Lok E, Swanson KD. Alternating Electric Fields Therapy for Malignant Gliomas: From Bench Observation to Clinical Reality. In: *Progress in Neurological Surgery*. Vol 32. ; 2018:180-195. doi:10.1159/000469690
 50. Spiliotis ET, Kinoshita M, Nelson WJ. A Mitotic Septin Scaffold Required for Mammalian Chromosome Congression and Segregation. *Science (80-)*. 2005;307(5716):1781-1785. doi:10.1126/science.1106823
 51. Gera N, Yang A, Holtzman TS, Lee SX, Wong ET, Swanson KD. Tumor Treating Fields Perturb the Localization of Septins and Cause Aberrant Mitotic Exit. Prigent C, ed. *PLoS One*. 2015;10(5):e0125269. doi:10.1371/journal.pone.0125269
 52. Tuszynski J, Wenger C, Friesen D, Preto J. An Overview of Sub-Cellular Mechanisms Involved in the Action of TTFIELDS. *Int J Environ Res Public Health*. 2016;13(11):1128. doi:10.3390/ijerph13111128
 53. Carrieri FA, Smack C, Siddiqui I, Kleinberg LR, Tran PT. Tumor Treating Fields: At the Crossroads Between Physics and Biology for Cancer Treatment. *Front Oncol*. 2020;10. doi:10.3389/fonc.2020.575992
 54. Li X, Yang F, Rubinsky B. A Correlation Between Electric Fields That Target the Cell Membrane Potential and Dividing HeLa Cancer Cell Growth Inhibition. *IEEE Trans Biomed Eng*. 2021;68(6):1951-1956. doi:10.1109/TBME.2020.3042650
 55. Chang E, Patel CB, Pohling C, et al. Tumor treating fields increases membrane

- permeability in glioblastoma cells. *Cell Death Discov.* 2018;4(1):113. doi:10.1038/s41420-018-0130-x
56. Yang M, Brackenbury WJ. Membrane potential and cancer progression. *Front Physiol.* 2013;4. doi:10.3389/fphys.2013.00185
 57. Goldberg SN. Radiofrequency tumor ablation: principles and techniques. *Eur J Ultrasound.* 2001;13(2):129-147. doi:10.1016/S0929-8266(01)00126-4
 58. Izzo F, Granata V, Grassi R, et al. Radiofrequency Ablation and Microwave Ablation in Liver Tumors: An Update. *Oncologist.* 2019;24(10):e990-e1005. doi:10.1634/theoncologist.2018-0337
 59. Wagstaff P, Buijs M, van den Bos W, et al. Irreversible electroporation: state of the art. *Onco Targets Ther.* 2016;9:2437. doi:10.2147/OTT.S88086
 60. Rubinsky B. Irreversible Electroporation in Medicine. *Technol Cancer Res Treat.* 2007;6(4):255-259. doi:10.1177/153303460700600401
 61. Garcia PA, Kos B, Rossmeis JH, Pavliha D, Miklavčič D, Davalos R V. Predictive therapeutic planning for irreversible electroporation treatment of spontaneous malignant glioma. *Med Phys.* 2017;44(9):4968-4980. doi:10.1002/mp.12401
 62. Ding L, Moser M, Luo Y, Zhang W, Zhang B. Treatment Planning Optimization in Irreversible Electroporation for Complete Ablation of Various Sized Cervical Tumors: A Numerical Study. *J Biomech Eng.* 2021;143(1). doi:10.1115/1.4047551
 63. Lozano AM, Lipsman N, Bergman H, et al. Deep brain stimulation: current challenges and future directions. *Nat Rev Neurol.* 2019;15(3):148-160. doi:10.1038/s41582-018-0128-2
 64. Krauss JK, Lipsman N, Aziz T, et al. Technology of deep brain stimulation: current status and future directions. *Nat Rev Neurol.* 2021;17(2):75-87. doi:10.1038/s41582-020-00426-z
 65. Amon A, Alesch F. Systems for deep brain stimulation: review of technical features. *J Neural Transm.* 2017;124(9):1083-1091. doi:10.1007/s00702-017-1751-6
 66. Cogan SF, Ludwig KA, Welle CG, Takmakov P. Tissue damage thresholds during therapeutic electrical stimulation. *J Neural Eng.* 2016;13(2):021001. doi:10.1088/1741-2560/13/2/021001
 67. Anderson DN, Osting B, Vorwerk J, Dorval AD, Butson CR. Optimized programming algorithm for cylindrical and directional deep brain stimulation electrodes. *J Neural Eng.* 2018;15(2):026005. doi:10.1088/1741-2552/aaa14b
 68. Howell B, Grill WM. Evaluation of high-perimeter electrode designs for deep brain stimulation. *J Neural Eng.* 2014;11(4):046026. doi:10.1088/1741-2560/11/4/046026
 69. Howell B, Huynh B, Grill WM. Design and *in vivo* evaluation of more efficient and selective deep brain stimulation electrodes. *J Neural Eng.* 2015;12(4):046030.

doi:10.1088/1741-2560/12/4/046030

70. Satzer D, Lanctin D, Eberly LE, Abosch A. Variation in Deep Brain Stimulation Electrode Impedance over Years Following Electrode Implantation. *Stereotact Funct Neurosurg.* 2014;92(2):94-102. doi:10.1159/000358014
71. Wei XF, Grill WM. Impedance characteristics of deep brain stimulation electrodes *in vitro* and *in vivo*. *J Neural Eng.* 2009;6(4):046008. doi:10.1088/1741-2560/6/4/046008
72. Lempka SF, Miocinovic S, Johnson MD, Vitek JL, McIntyre CC. In vivo impedance spectroscopy of deep brain stimulation electrodes. *J Neural Eng.* 2009;6(4):046001. doi:10.1088/1741-2560/6/4/046001
73. Li X, Yang F, Gao B, Yu X, Rubinsky B. A Theoretical Analysis of the Effects of Tumor-Treating Electric Fields on Single Cells. *Bioelectromagnetics.* 2020;41(6):438-446. doi:10.1002/bem.22274
74. Li X, Yang F, Rubinsky B. A Theoretical Study on the Biophysical Mechanisms by Which Tumor Treating Fields Affect Tumor Cells During Mitosis. *IEEE Trans Biomed Eng.* 2020;67(9):2594-2602. doi:10.1109/TBME.2020.2965883
75. Berkelmann L, Bader A, Meshksar S, et al. Tumour-treating fields (TTFields): Investigations on the mechanism of action by electromagnetic exposure of cells in telophase/cytokinesis. *Sci Rep.* 2019;9(1):7362. doi:10.1038/s41598-019-43621-9
76. Wenger C, Salvador R, Basser PJ, Miranda PC. Improving Tumor Treating Fields Treatment Efficacy in Patients With Glioblastoma Using Personalized Array Layouts. *Int J Radiat Oncol.* 2016;94(5):1137-1143. doi:10.1016/j.ijrobp.2015.11.042
77. Lok E, San P, Hua V, Phung M, Wong ET. Analysis of physical characteristics of Tumor Treating Fields for human glioblastoma. *Cancer Med.* 2017;6(6):1286-1300. doi:10.1002/cam4.1095
78. Miranda PC, Mekonnen A, Salvador R, Basser PJ. Predicting the electric field distribution in the brain for the treatment of glioblastoma. *Phys Med Biol.* 2014;59(15):4137-4147. doi:10.1088/0031-9155/59/15/4137
79. Wenger C, Salvador R, Basser PJ, Miranda PC. The electric field distribution in the brain during TTFields therapy and its dependence on tissue dielectric properties and anatomy: a computational study. *Phys Med Biol.* 2015;60(18):7339-7357. doi:10.1088/0031-9155/60/18/7339
80. Korshoej AR, Saturnino GB, Rasmussen LK, von Oettingen G, Sørensen JCH, Thielscher A. Enhancing Predicted Efficacy of Tumor Treating Fields Therapy of Glioblastoma Using Targeted Surgical Craniectomy: A Computer Modeling Study. Debinski W, ed. *PLoS One.* 2016;11(10):e0164051. doi:10.1371/journal.pone.0164051
81. Wenger C, Bomzon Z, Salvador R, Basser PJ, Miranda PC. Simplified realistic human head model for simulating Tumor Treating Fields (TTFields). In: *2016 38th Annual International Conference of the IEEE Engineering in Medicine and*

- Biology Society (EMBC)*. Vol 2016-October. IEEE; 2016:5664-5667. doi:10.1109/EMBC.2016.7592012
82. Chaudhry A, Benson L, Varshaver M, et al. NovoTTFTM-100A System (Tumor Treating Fields) Transducer Array Layout Planning for Recurrent Glioblastoma: Results of a NovoTALTM System User Study. *Int J Radiat Oncol*. 2015;93(3):E59-E60. doi:10.1016/j.ijrobp.2015.07.694
 83. Elwassif MM, Kong Q, Vazquez M, Bikson M. Bio-heat transfer model of deep brain stimulation-induced temperature changes. *J Neural Eng*. 2006;3(4):306-315. doi:10.1088/1741-2560/3/4/008
 84. Elwassif MM, Datta A, Rahman A, Bikson M. Temperature control at DBS electrodes using a heat sink: experimentally validated FEM model of DBS lead architecture. *J Neural Eng*. 2012;9(4):046009. doi:10.1088/1741-2560/9/4/046009
 85. Butson CR, Maks CB, McIntyre CC. Sources and effects of electrode impedance during deep brain stimulation. *Clin Neurophysiol*. 2006;117(2):447-454. doi:10.1016/j.clinph.2005.10.007
 86. Alonso F, Latorre M, Göransson N, Zsigmond P, Wårdell K. Investigation into Deep Brain Stimulation Lead Designs: A Patient-Specific Simulation Study. *Brain Sci*. 2016;6(3):39. doi:10.3390/brainsci6030039
 87. Butson CR, McIntyre CC. Role of electrode design on the volume of tissue activated during deep brain stimulation. *J Neural Eng*. 2006;3(1):1-8. doi:10.1088/1741-2560/3/1/001
 88. Kramme J, Dembek TA, Treuer H, et al. Potentials and Limitations of Directional Deep Brain Stimulation: A Simulation Approach. *Stereotact Funct Neurosurg*. 2021;99(1):65-74. doi:10.1159/000509781
 89. Miranda PC, Mekonnen A, Salvador R, Ruffini G. The electric field in the cortex during transcranial current stimulation. *Neuroimage*. 2013;70:48-58. doi:10.1016/j.neuroimage.2012.12.034
 90. Neuling T, Wagner S, Wolters CH, Zaehle T, Herrmann CS. Finite-Element Model Predicts Current Density Distribution for Clinical Applications of tDCS and tACS. *Front Psychiatry*. 2012;3(SEP). doi:10.3389/fpsyt.2012.00083
 91. Berjano EJ. Theoretical modeling for radiofrequency ablation: state-of-the-art and challenges for the future. *Biomed Eng Online*. 2006;5(1):24. doi:10.1186/1475-925X-5-24
 92. Lobo SM, Liu Z-J, Yu NC, et al. RF tumour ablation: Computer simulation and mathematical modelling of the effects of electrical and thermal conductivity. *Int J Hyperth*. 2005;21(3):199-213. doi:10.1080/02656730400001108
 93. Bourrier F, Duchateau J, Vlachos K, et al. High-power short-duration versus standard radiofrequency ablation: Insights on lesion metrics. *J Cardiovasc Electrophysiol*. 2018;29(11):1570-1575. doi:10.1111/jce.13724
 94. Agnass P, van Veldhuisen E, van Gemert MJC, et al. Mathematical modeling of the thermal effects of irreversible electroporation for *in vitro*, *in vivo*, and clinical

- use: a systematic review. *Int J Hyperth.* 2020;37(1):486-505. doi:10.1080/02656736.2020.1753828
95. Edd JF, Davalos R V. Mathematical Modeling of Irreversible Electroporation for Treatment Planning. *Technol Cancer Res Treat.* 2007;6(4):275-286. doi:10.1177/153303460700600403
 96. Amaran S, Sahinidis N V., Sharda B, Bury SJ. Simulation optimization: a review of algorithms and applications. *Ann Oper Res.* 2016;240(1):351-380. doi:10.1007/s10479-015-2019-x
 97. Nocedal J, Wright S. *Numerical Optimization.* New York: Springer; 2006.
 98. Lange K. *Optimization.* New York: Springer; 2013.
 99. Boyd SP, Vandenberghe L. *Convex Optimization.* Cambridge University Press; 2004.
 100. Korshoej AR, Sørensen JCH, von Oettingen G, Poulsen FR, Thielscher A. Optimization of tumor treating fields using singular value decomposition and minimization of field anisotropy. *Phys Med Biol.* 2019;64(4):04NT03. doi:10.1088/1361-6560/aafe54
 101. Corovic S, Zupanic A, Miklavcic D. Numerical Modeling and Optimization of Electric Field Distribution in Subcutaneous Tumor Treated With Electrochemotherapy Using Needle Electrodes. *IEEE Trans Plasma Sci.* 2008;36(4):1665-1672. doi:10.1109/TPS.2008.2000996
 102. 3D Slicer. 3D Slicer image computing platform. <https://www.slicer.org>.
 103. Kikinis R, Pieper SD, Vosburgh KG. 3D Slicer: A Platform for Subject-Specific Image Analysis, Visualization, and Clinical Support. In: *Intraoperative Imaging and Image-Guided Therapy.* New York, NY: Springer New York; 2014:277-289. doi:10.1007/978-1-4614-7657-3_19
 104. Jolesz FA. *Intraoperative Imaging and Image-Guided Therapy.* (Jolesz FA, ed.). New York, NY: Springer New York; 2014. doi:10.1007/978-1-4614-7657-3

Chapter 2

2 Optimization of Multi-Electrode Implant Configurations and Programming for the Delivery of Non-Ablative Electric Fields in Intratumoural Modulation Therapy

This chapter was adapted from the published article entitled “Optimization of multi-electrode implant configurations and programming for the delivery of non-ablative electric fields in intratumoural modulation therapy” by Erin Iredale, Andrew Deweyert, Douglas A. Hoover, Jeff Z. Chen, Susanne Schmid, Matthew O. Hebb, Terry M. Peters, and Eugene Wong, Medical Physics, 47(11):5441-5454 (2020). Permission to reproduce can be found in Appendix A.

2.1 Introduction

There have been substantial recent advances in the application of electric fields to treat various forms of cancer¹⁻¹². Intratumoural modulation therapy (IMT) is a developing technology that uses implanted bioelectrodes to generate electric fields to control tumour growth¹⁰⁻¹². By implanting electrodes directly within or adjacent the tumour volume, IMT has the potential to provide perpetual, titratable therapy for a variety of tumour types using a concealed, low maintenance delivery system. Preclinical studies in malignant brain tumours have demonstrated robust efficacy of IMT monotherapy at 200 kHz, +/- 2 V stimulation through *in vitro* investigations of patient derived Glioblastoma Multiforme (GBM) cells (65% cell viability)¹¹, and *in vivo* rodent models (20% reduction in tumour volume)¹¹. While there is currently no observed impact on normal neurons or adverse neurological effects in the treated rodent cohort for low voltage (2 V), intermediate frequency (200 kHz) electric fields¹¹⁻¹², surgical implantation of electrodes will pose the main safety concern with this treatment on human patients. A marked benefit of incorporating IMT within multi-modality treatment paradigms was observed through *in vitro* GBM models (cell viability reduction from 83% for temozolomide (TMZ) alone to 46% for combined IMT+TMZ)¹¹, and on patient derived diffuse intrinsic pontine glioma cells, where incorporating IMT with combined radiation and TMZ (44% vs. 60% cell viability) reduced cell viability to 20%¹⁰. These studies were performed however using a

non-optimized single electrode system with no phase shifting of input waveforms that was subsequently found to be limited by inadequate spatial coverage, with only 6.2% of the *in vitro* dish area covered by the desired 1 V/cm¹⁰ and associated constraints on tumour control with 24% of an *in vivo* tumour receiving 1 V/cm¹¹.

An extensive search of the published literature through databases including PubMed, Google Scholar and Scopus was completed using Boolean OR keywords such as tumour treating fields computer simulations and optimizations, implantable electrotherapeutic devices, deep brain stimulation, electroporation, electric field optimization, simulation-based optimization, and non-convex optimization. There are publications on optimizing electric field for treatment of tumours from external devices^{7-9,13,14-16}, for deep brain stimulation with multiple contacts to steer the field to treat the intended millimeter sized target¹⁷, and for electroporation with multiple electrodes to cover tumour volumes with large field magnitude¹⁸⁻¹⁹. The present study is the first of its kind to extend and optimize the distribution of therapeutic-range IMT fields across tumour volumes using multiple implanted electrodes rather than a single stimulation source. Advantages of the present study include incorporating multiple electrodes with multiple contacts, phase shift of input waveforms, tissue sparing, algorithm robustness evaluation, and avoidance of local minima through a custom pattern search approach. Critical fundamental unknowns include the maximum tumour volumes attainable with multi-electrode IMT, configuration and placement of electrodes and selection of stimulation parameters to maintain a minimal stimulation voltage and number of electrodes, while still covering the tumour volume with the necessary electric field. Simulations in previous studies have found that single electrode stimulation only covers a small volume in both *in vitro* and *in vivo* experiments, and multiple electrodes would be required for necessary coverage^{10,11}. 1 V/cm has been used as a threshold for *in vitro*^{4,5,10,11}, *in vivo*^{4,5,11}, and in Glioblastoma Multiforme clinical trials^{1-4,20}. While it has been suggested that thresholds likely differ between tumour types¹⁰, this study will use a threshold of 1 V/cm to demonstrate our optimization algorithm. However, the optimization method introduced in this study can use any desired field threshold. Simulations and optimizations have been established for an external device, but electric fields delivered using the external device require an accurate anisotropic conductivity whole brain map to determine the field to the tumour

volume²¹⁻²². Conversely, electrodes placed internally within the tumour volume don't require the same accuracy of surrounding tissue conductivity anisotropies, as electric fields are not passing through layers of tissue with varying electrical properties.

As with early brachytherapy, a set of interstitial implant rules such as the Manchester system were established to serve as practical treatment planning guidelines for treating tumours of various sizes²³. Both brachytherapy and IMT utilize multiple implanted sources (radiation vs. electric field) to deliver treatment, with large and steep "dose" gradients near the contact surface, so the experience gained from early brachytherapy treatment planning in terms of implant rules can be borrowed to initiate a set of rules for IMT. Providing analogous IMT rules in the present study for the number of electrodes required to cover various tumour sizes, the placement and programming of those electrodes, and starting points for patient-specific treatment optimization will allow for clinical implementation of IMT.

Based on experience from external delivery of tumour treating fields^{7-9,13,14-16}, deep brain stimulation optimizations¹⁷, and irreversible electroporation optimizations¹⁸⁻¹⁹, the incorporation of simulations and electric field optimizations ensure the desired field is being delivered to the tumour volume. The creation of methods to robustly optimize the electric field delivered to a tumour volume is a necessary step in the development of multi-electrode IMT. Stochastic optimization algorithms are designed to escape local minima by giving a finite probability to choose optimization parameters that steps away from the local minimum. Methods to evaluate the robustness of our algorithm have been considered in this study. We need to determine the configurations and stimulation parameters that result in the desired electric fields before proceeding to performing experiments *in vitro* and *in vivo*. In this study we propose the introduction of multiple stimulating electrodes with relative phase shifts between their respective stimulation waveforms, as a variable parameter to increase the electric field coverage over time. We demonstrate that the optimization of treatment parameters can be cast as a mathematical optimization problem, utilizing computer simulations to compute the electric field distribution over time. The goal of this study is to determine the optimal geometric electrode configurations and input waveform relative phase shifts, and to estimate the

maximum treatable tumour volume for between 2 and 7 electrodes. To achieve this, we developed optimization methods that were utilized to form multi-electrode IMT configuration and programming rules for between 2 and 7 electrodes, to enable future applications to *in vitro* and *in vivo* preclinical models and patient-specific human tumour scenarios.

2.2 Materials and Methods

2.2.1 Electric Field Simulation

The *in-silico* tumour and electrode models were created in COMSOL Multiphysics (v5.4). Material properties were assigned to each geometrical entity in the model, including tumour, electrodes, and surrounding media. The optimization procedure in the present study does not depend on tumour site/location, though we require the electrical properties of the tumour and surrounding tissue. Since the electrical properties in the brain are most well-known, these simulations were completed using human brain and tumour tissue as an example. A literature search of measured electrical properties of human brain and tumour tissues at 200 kHz was performed, and standard relative dielectric ϵ and conductivity σ values for external tumour treating fields simulation and treatment planning were used^{7-9,14-15,22}, originally obtained from *in vivo* measurements on living tissues at comparable frequencies between 50 and 100 kHz²⁴⁻²⁷. The relative dielectric and conductivity values for the tumour were 2000 and 0.24 S/m respectively, and for the normal surrounding grey matter brain, 3000 and 0.25 S/m^{7-9,14-15,22,24-27}. White matter and grey matter can be incorporated as needed, since surrounding brain tissue depends on the tumour location. These conductivity and dielectric values were used to demonstrate the methods, but the pipeline allows users to input any necessary electrical properties. The example electrode material used here was platinum-iridium with a relative permittivity of 1²⁸ and conductivity of 5.278×10^6 S/m²⁹. The electrodes were assigned a 0.8 mm radius to represent the upper range in deep brain stimulation electrode size³⁰⁻³³, with variable contact height to allow for adequate depth coverage, location in polar coordinates (r, θ) , and input voltage sinusoidal waveforms $(A \sin(2\pi ft - \varphi))$, where A is the amplitude, f is the frequency of 200 kHz, t is the time, and φ is the

phase shift. Non-ablative input voltage amplitudes of 2 and 4 V were applied in this study.

The tumour volume was given a variable diameter to allow for the computation of maximum tumour size versus number of electrodes. The total electrode contact height used was the tumour diameter + 2 mm, to ensure adequate coverage at the poles, and for multiple contact electrodes, the spacing between contacts was 0.5 mm³⁰⁻³³. The height of exposed electrode contact is held constant between single, dual and three contact models. Starting with 2 single contact electrodes, the number of electrodes was increased to 3, 4, 5, 6 and 7, and the number of contacts per electrode was also increased to 2 and 3 to further demonstrate our optimization algorithm in 3 dimensions (Figure 2.1).

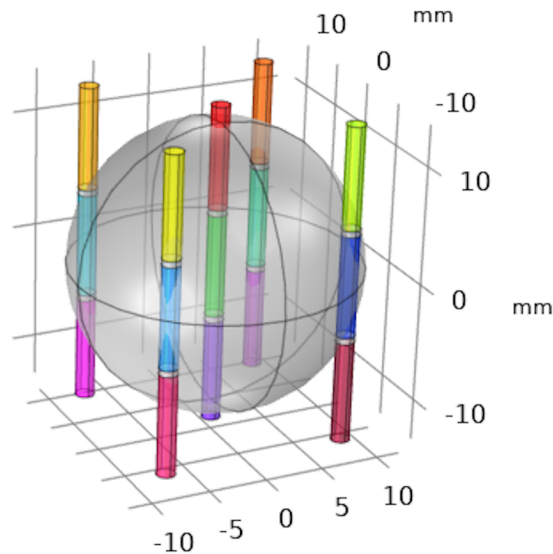


Figure 2.1: Geometry of a 5 electrode, 3 contact tumour model (grey) created in COMSOL. Total of 15 contacts, each with separately programmable input waveforms highlighted by different colours. The tumour is surrounded by normal tissue.

Using the AC/DC module in COMSOL Multiphysics, each electrode contact was given a separately programmed input voltage waveform terminal boundary. Any spacing between multiple contacts was insulated, satisfying $\mathbf{n} \cdot \mathbf{J} = 0$ where \mathbf{n} is the normal vector on the boundary, and \mathbf{J} is the current density. Electrical insulation was also assumed on the

outer boundary of the surrounding material. On internal boundaries between media with different electrical properties, continuity is maintained by the boundary condition $\mathbf{n}_2 \cdot (\mathbf{J}_1 - \mathbf{J}_2) = 0$, where subscripts 1 and 2 indicate the different media. A free tetrahedral mesh was created for the model, with varying sizes depending on the volume material. A time-dependent study was used to compute the electric field at 16 time points over half a period of the sinusoidal waveform. Using the electric currents user interface in COMSOL, a finite-element method was used to compute the electric field distribution on mesh points for our model. The governing equations for the finite element computation are Ohm's law (2.1), the equation of continuity (2.2), and Gauss' law (2.3):

$$\mathbf{J}(\mathbf{x}, t) = \sigma \mathbf{E}(\mathbf{x}, t) \quad (2.1)$$

$$\frac{\partial \rho(\mathbf{x}, t)}{\partial t} + \nabla \cdot \mathbf{J}(\mathbf{x}, t) = 0 \quad (2.2)$$

$$\nabla \cdot \varepsilon \mathbf{E}(\mathbf{x}, t) = \rho(\mathbf{x}, t) \quad (2.3)$$

where $\mathbf{J}(\mathbf{x}, t)$ is the current density as a function of location \mathbf{x} and time t , σ is the conductivity, $\mathbf{E}(\mathbf{x}, t)$ is the location and time dependent electric field, $\rho(\mathbf{x}, t)$ is the charge density and ε is the dielectric constant.

2.2.2 Sensitivity Analysis

In the present models of constant voltage stimulation, the impedance magnitude $|\mathbf{Z}|$ of the tissue,

$$|\mathbf{Z}| = \left(\left(\frac{1}{R} \right)^2 + (2\pi f C)^2 \right)^{-0.5} \quad (2.4)$$

depends on resistance $R \propto 1/\sigma$, frequency f and capacitance $C \propto \varepsilon$. COMSOL was used to simulate the resistance and capacitance, and therefore impedance of the spherical tumour models. Depending on the number of electrodes, contacts and the geometrical configuration of each model, the resistance ranged from 100-400 Ω , and the capacitance was $\sim 10^{-10}$ F. Based on the maximum simulated resistance of 400 Ω , and the capacitance of 10^{-10} F, the impedance was calculated (Eqn. 2.4) for a range of frequencies from 0 to 4

MHz. The resistance term of the impedance (R^{-2}) dominated the capacitance term ($(2\pi fC)^2$) up to 2 MHz ($R^{-1} > 2\pi fC$). Above 2 MHz, the capacitance term dominated ($R^{-1} < 2\pi fC$). For the frequency range in this study (200 kHz), the resistance and therefore conductivity dominate the impedance. The sensitivity of the impedance to changes in frequency was examined from 0 to 4 MHz.

To examine the sensitivity of electric field distributions to changes in frequency, the electric field was simulated for the most complex 5 electrode geometry for a range of frequencies between 0 and 4 MHz. For each frequency, the resultant electric field matrices for 16 time points were averaged to obtain the temporal electric field magnitude \bar{E} . The relative difference E_{diff} in the temporal average electric field magnitude \bar{E} was calculated relative to the field map at the reference frequency f_{ref} of 200 kHz.

$$E_{diff} = \frac{|\bar{E}(f) - \bar{E}(f_{ref})|}{\bar{E}(f_{ref})} \quad (2.5)$$

Temporal average electric field maps were considered equivalent when E_{diff} was less than 1%. The sensitivity of electric field to changes in tumour conductivities were also analyzed (Eqn. 2.5), with f and f_{ref} in (Eqn. 2.5) replaced with σ and σ_{ref} . Conductivities between 0.01 and 1 S/m were analyzed. The relative dielectric constant sensitivity was analyzed with f and f_{ref} in (Eqn. 2.5) replaced with ϵ and ϵ_{ref} respectively for dielectrics ranging from 10 to 5000.

2.2.3 Optimization Algorithm

The optimization of the electric field coverage was coded in MATLAB and the COMSOL MATLAB Livelink used to connect our COMSOL model to our MATLAB code. We used the following least square objective function:

$$F = \frac{1}{N_s} \sum_j \Theta(E_{pres} - \bar{E}_j) (\bar{E}_j - E_{pres})^2 \quad (2.6)$$

where the sum is over the voxel j , N_s is the number of voxels in the tumour volume, Θ is the Heaviside function, E_{pres} is the prescription electric field threshold, and \bar{E}_j is the time average electric field magnitude,

$$\bar{E}_j = \frac{1}{N_t} \sum_i E_{i,j} \quad (2.7)$$

where the sum is over time point i , and N_t is the number of time points. This objective has been repurposed from radiotherapy³⁴ to be used specifically for IMT delivery, and when minimized, optimizes the electric field coverage of the tumour over time. The Heaviside function was chosen to distinguish between covered voxels ($\bar{E}_j \geq E_{pres}$) and uncovered voxels ($\bar{E}_j < E_{pres}$), and the square difference term accounts for the contribution of uncovered voxels. The farther away a voxel is from the prescription field, the more it will affect the objective. Depending on tumour type, this prescription field can be changed to any necessary field magnitude. While externally delivered electric field optimizations typically maximize the average field to the tumour due to the inherently homogeneous nature of external delivery^{9,33}, the nature of implanted electrodes, where the large electric fields and steep field gradients present near the electrode contact surface dominate the electric field average. While the average electric field to the tumour could be maximized using such objective functions, this could result in areas of the tumour not being covered by the desired field threshold in the case of implanted electrodes. Similar to brachytherapy, where a target volume is optimized to be covered by the prescription dose²³, we chose an objective function to allow optimization of the extent of tumour coverage with a more homogeneous electric field distribution to minimize cold spots^{34,35}.

The algorithm includes an option to minimize the field delivered to regions outside the tumour volume, by adding a weighted term to the objective function,

$$G = \frac{1}{N_s} \sum_j \Theta(E_{pres} - \bar{E}_j) (\bar{E}_j - E_{pres})^2 + w \frac{1}{N_n} \sum_k (\overline{ES}_k)^2 \quad (2.8)$$

where w is the weighting factor, the second sum is over the normal tissue voxel k , N_n is the number of voxels in the surrounding normal tissue, and \overline{ES}_k is the time average electric field magnitude of normal tissue voxels. The weighting factor w can be adjusted

based on the importance of tissue sparing, and in this example a weighting factor of 0.1 was chosen based on trial optimizations (w ranging from 0.05 to 1.00) to balance tumour coverage with the avoidance of critical tissue³⁵. In addition to incorporating tissue sparing, weighted terms can be added to account for different tumour regions requiring different field thresholds depending on growth activity.

The optimization parameters used in this study were the location of each electrode (r, θ) (bounded to within tumour volume), and the phase shift φ (0 to 2π radians) of each electrode contacts input waveform. Models with between 2 and 7 electrodes with 1 to 3 contacts per electrode were investigated on spherical tumours up to 5.5 cm in diameter. The number of variables depends on the number of electrodes, and the number of contacts per electrode. In the present study, we held one electrode angle θ and one contact phase φ constant at 0 as the reference. Therefore, if n is the number of electrodes and c is the number of contacts, a full parameter optimization contains $2n + nc - 2$ variables.

For each iteration of variables in the optimization algorithm, the electric field over time was computed in COMSOL, and the resultant field was linearly interpolated on a $100 \times 100 \times 100$ grid of equally spaced points covering the tumour volume. As our first step, we employed only electric field values within the tumour volume in the evaluation of the objective function.

To determine which optimization strategy would best fit this problem, we first determined whether our objective function was convex³⁶. A function F is convex if for all points in the domain $(\vec{x}, \vec{y}) \in \mathbb{R}^n$ and all $\lambda \in [0, 1]$:

$$F(\lambda\vec{x} + (1 - \lambda)\vec{y}) \leq \lambda F(\vec{x}) + (1 - \lambda)F(\vec{y}). \quad (2.9)$$

By showing a single counter example to this inequality, we demonstrated that the problem is non-convex. This convexity test can be found in the supplementary materials (Appendix C).

In addition to this problem being non-convex for full location with phase optimizations, the computation of the gradient of our objective, which must be estimated by finite differences, is unreliable due to the mesh grid discretization of the electric field.

Due to the non-convexity of our problem and the unreliability of the gradient, we chose to customize the pattern search method, a gradient free, direct search optimization strategy for this study³⁷. This approach allows for a broader search of the parameter space, to help avoid falling into a local minimum. Each time the algorithm finds a better solution, the parameter step size is increased. Conversely, if no better point is found, the step size is decreased. The pattern search method was implemented using a custom MATLAB function that minimized our objective within certain bounds with a given starting point. Due to the uniqueness of our problem in determining IMT treatment parameters, a custom algorithm was developed. Within the algorithm, once the locations of the electrodes are selected for a given iteration, we made use of superposition of electric field from each electrode to optimize for its phase of the stimulation voltage. Such superposition of the electric field allows us to calculate the electric field once only and repeatedly use it during the voltage phase optimization. To avoid bias of user inputted starting points, parameter starting points were determined using $2n$ random samples of parameter space, and to improve convergence rate, the objective function was evaluated for those $2n$ samples, and the parameters resulting in the best objective were used as the starting point³⁸⁻³⁹. The overall pipeline of the optimization algorithm begins with the creation of the COMSOL model, with manual input of tumour volume (either simple geometry or any irregular shape) and tissue dielectric and conductivity properties, choice of optimization parameters and bounds (location, relative phase shift), choice of objective function (no tissue sparing or tissue sparing), and lastly, the pattern search optimization which evaluated the objective function based on the COMSOL simulations.

2.2.4 Robustness of the Pattern Search Algorithm

The robustness of our pattern search algorithm was evaluated for the 5 electrode 3 contact full phase optimization (14 variables relative to the top contact of electrode 1). Each of the 14 electrode contacts was assigned a random relative phase shift starting point for the optimization. The pattern search optimization was repeated for 50 more random starting

points to evaluate the convergence of the pattern search algorithm to the optimal solution. The algorithm was considered converged to an optimal solution³⁷⁻³⁹ when the change in parameter value (step size) for an iteration was less than 1% of the range of the parameter (when phase shift parameter changes reached 0.063 radians ($\frac{2\pi}{100}$), and location changes were below 0.3 mm)³⁸⁻³⁹. The starting parameters, optimal parameters, starting objective value, optimal objective value and number of iterations were all considered for each run of the algorithm.

2.2.5 Spherical Tumour Optimal Configurations, Phase Shift and Maximum Treatable Tumour Size

The maximum treatable tumour size for each number of electrodes was estimated by using the optimal geometric and phase configurations found by our algorithm. Since the optimal location within each configuration is dependent on the tumour size, the specific electrode locations were optimized for a range of tumour sizes. The electric field distributions for these optimal locations were then evaluated for the percentage of tumour volume covered by 95% of the prescription field (1 V/cm). We defined the maximum treatable tumour size as the spherical diameter with at least 95% of the volume covered by a 95% time average field “dose”. This threshold was adopted from the minimum standard for radiotherapy treatment planning⁴⁰⁻⁴¹. We began by optimizing the location and phase shifts of up to 7 electrode systems with single contact electrodes. Once we understood this, we optimized the configuration for electrodes with 2 and then 3 contacts.

2.2.6 Tissue Sparing

The optimization algorithm was applied to a tissue sparing example, where a 2.5 cm diameter spherical tumour was intersected by a 1.8 cm diameter cylindrical organ to be spared, creating a non-spherical target volume. The weighing factor in the objective G was set to $w = 0.1$ in this example. A full location and phase shift optimization of a 5-electrode single contact model was implemented in this investigation.

2.3 Results

2.3.1 Sensitivity Analysis

A sensitivity analysis was performed to investigate frequency, conductivity, and dielectric constant effects on the electric field. There was less than 1% change in impedance over the range of 0-350 kHz relative to the 200 kHz impedance value. The relative difference in temporal average electric field maps was found to be less than 1% for frequencies ranging from 0 to 500 kHz relative to the 200 kHz reference field map. The relative difference in electric field maps was found to be less than 1% for conductivities ranging from 0.2 to 0.3 S/m relative to the 0.24 S/m reference field map, and dielectric constants between 500 and 4000 had equivalent field maps within 1% difference relative to the 2000 dielectric reference field map.

2.3.2 Robustness of the Pattern Search Algorithm

Our custom pattern search algorithm was robust in finding a global minimum of our optimization problem for the most complex case of full 14 variable phase optimization for the 5 electrode 3 contact model. For the 50 random starting parameter points, the optimization converged to a global optimum 45 times. The start and end objective values for all 50 runs are plotted in Figure 2.2. Due to the large number of local minima and many equivalent global minima (due to symmetry) in our problem, and the uncertainty in the objective function value (due to the discretization of the electric field), the algorithm was considered successful in finding a global minimum if the same objective value was reached to within a certain tolerance.

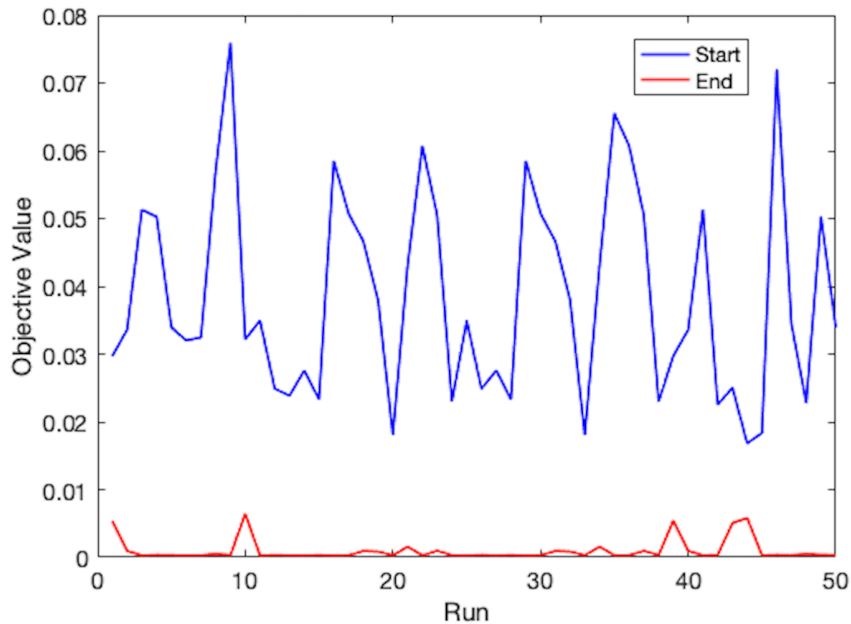


Figure 2.2: Objective function value for starting random parameters and final minimized objective value for 50 runs with different random starting parameters.

2.3.3 Spherical Tumour Optimal Configurations, Phase Shift and Maximum Treatable Tumour Size

Single contact electrodes:

Beginning with single contact electrodes and a spherical tumour model, we were able to use our optimization algorithm to find the configurations and relative phase shifts that resulted in the largest and most uniform electric field coverage over time. We then compared these optimal results to the field coverage when stimulating 2 V amplitude waveforms or ground electrodes were used, with no phase shifting.

The optimization of the 2-electrode model was completed in terms of the separation, and relative phase shift. The result was as expected, with maximally separated waveforms, with electrode 2 phase shifted π radians from electrode 1. We found that for the 2-electrode system, the maximum tumour diameter it can cover is 1.2 cm, with electrodes placed at $r = 4$ mm from the center. The temporal average electric field map of the optimal configuration is found in Figure 2.3, as well as the corresponding field animation

over time. This result matched the expected solution of completely out of phase sine waves, to create the maximum electric potential difference (hence maximum electric field) between electrodes.

We found that for a 3-electrode system, the maximum tumour diameter it can treat is 1.7 cm. Using maximum tumour size of 1.7 cm diameter, the optimal configuration found from our optimization was equally spaced input waveforms with phase shifts of $2\pi/3$ and $4\pi/3$ radians relative to electrode 1. The optimal geometrical configuration was with electrodes placed equidistant from the center, and each other. For this 1.7 cm diameter tumour volume, the optimal distance from the center was 6 mm. As can be seen in Figure 2.3(a(ii))'s corresponding animation, these parameters lead to an electric field that rotates over time, encompassing the whole tumour volume, with no stagnant 'cold spots'. Since we are dealing with a spherically symmetric model, we expect that electrodes spaced equidistant from each other and from the center of the sphere would be optimal. In addition, to create the most homogeneous electric field over time, maximally separated phase shifted input sine waves would lead to a symmetrically rotating electric field, which matched the optimization results.

For the 4-electrode model, the optimal configuration was all four electrodes placed equidistant from each other, with maximally separated input waveforms (phase shifts of 0.5π , π , 1.5π relative to electrode 1) to create a symmetrically rotating electric field. We found that for a 4-electrode system, the maximum tumour diameter that can be treated is 2.1 cm, for which the optimal distance from the center for each electrode was 7.5 mm.

Using a 5-electrode system, the maximum tumour diameter that can be treated is 2.5 cm with 2 V input waveforms. The optimal solution for this case was an electrode placed in the center, with 4 equally spaced surrounding electrodes. The phase shifts relative to the center electrode were 0.5π , 1.5π , 0.5π , 1.5π respectively. For a 2.5 cm diameter tumour, the optimal distance from the center was 11 mm. Field maps and animations of optimal solutions for both 4 and 5 electrode models can be found in Figure 2.3(a). For the 5-electrode model, we compared the optimal results to the non-optimized configuration with no use of phase shifting (Figure 2.3(b)). Since the electric field varied within the

tumour volume, a cumulative electric field volume histogram (EVH)^{6,9} was used to summarize the tumour coverage. We plotted the absolute tumour volume versus electric field strength in the EVH, indicating the minimum electric field strength that covers a certain volume of the tumour (Figure 2.3(c)). For the 5-electrode configuration when no phase shifting is used, less than 20% of a 2.5 cm diameter tumour volume is covered by 1 V/cm, but for the optimized phase shifting case, 95% of the tumour volume is covered. This large tumour coverage increase can be observed when introducing phase shift to models with any number of electrodes.

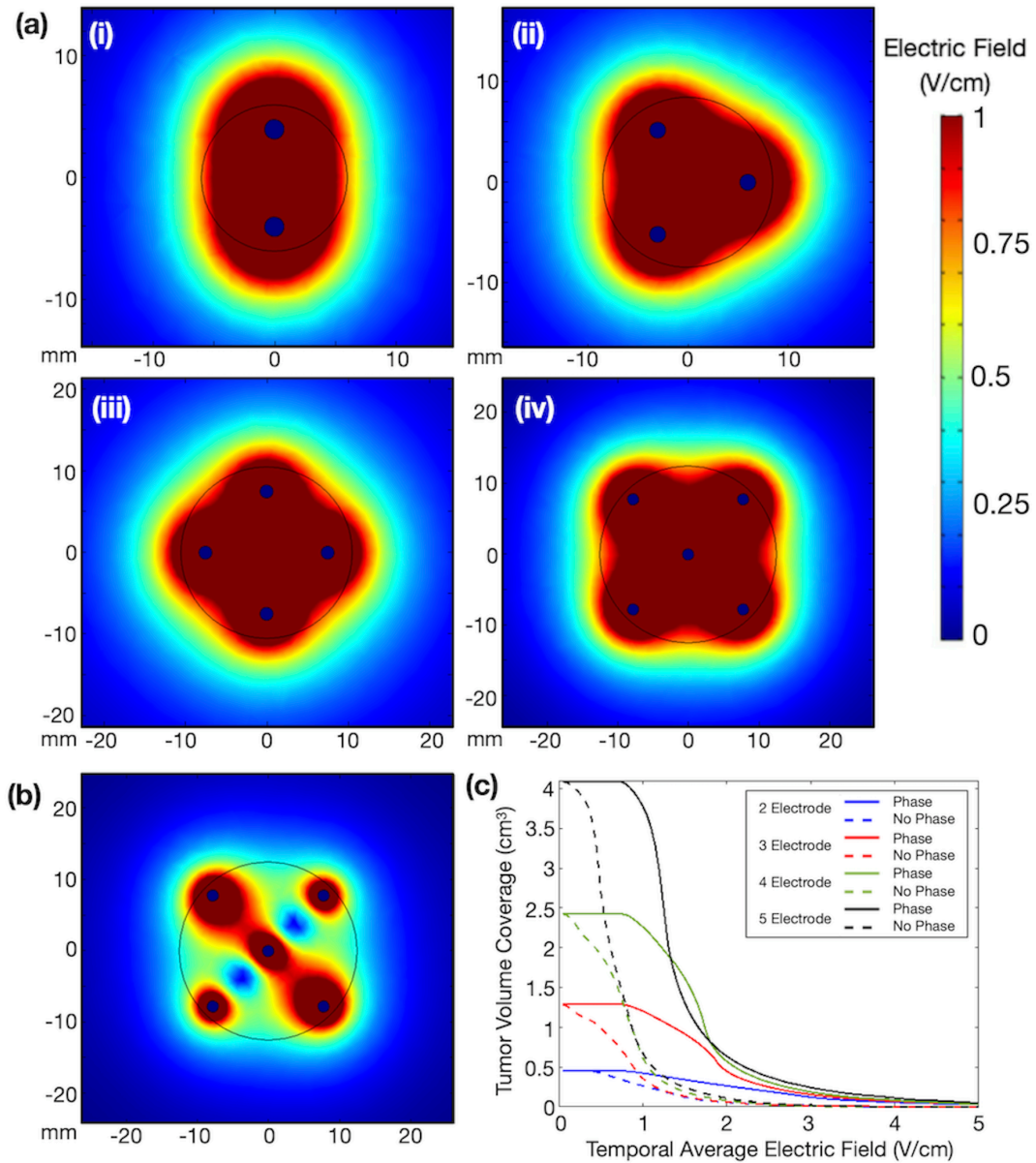


Figure 2.3: Average temporal electric field maps and corresponding animations of field coverage over time for (a) 2, 3, 4, and 5 optimally placed electrodes in cross sections of corresponding maximum tumour volumes (black circle). (b) 5-electrode configuration with no phase shifting (centre, upper left, bottom right: 2 V amplitude stimulating electrodes, upper right and bottom left: 0 V ground electrodes). 2, 3, and 4 electrode figures with no phase shifting can be found in Appendix C (Figure C.1). (c) Electric field volume histogram of the tumour volume (cm³) receiving at least a

certain temporal average electric field value (V/cm) for both optimized phase shift and no phase shift cases.

Our methods were extended to investigate the optimal configurations and phase settings for 6 and 7 electrode models. For 6 electrodes, up to 2.94 cm diameter tumours can be covered using 2 V input waveforms with the optimal location of each electrode (r, θ) in mm and radians of $(0,0)$, $(13.75, 0)$, $(13, 0.413\pi)$, $(11.5, 0.850\pi)$, $(14.75, 1.2 \pi)$, $(11.5, 1.588\pi)$. The corresponding optimal phase shifts were 0 , 0.618π , 1.460π , 0.372π , 0.938π , and 1.603π radians. Next for 7 electrodes, up to 3.34 cm diameter tumours can be covered with a configuration of one central electrode, with 6 equally spaced surrounding electrodes at 13.2 mm from the centre. The optimal phase shifts of the surrounding electrodes alternate between 0.550π and 1.436π , similar to the 5-electrode configuration. By using the optimal configurations found above, the maximum treatable tumour size (i.e., that with 95% coverage at 95% of the 1 V/cm prescription field) can be determined for each number of electrodes with 2 V and 4 V input waveforms (Figure 2.4).

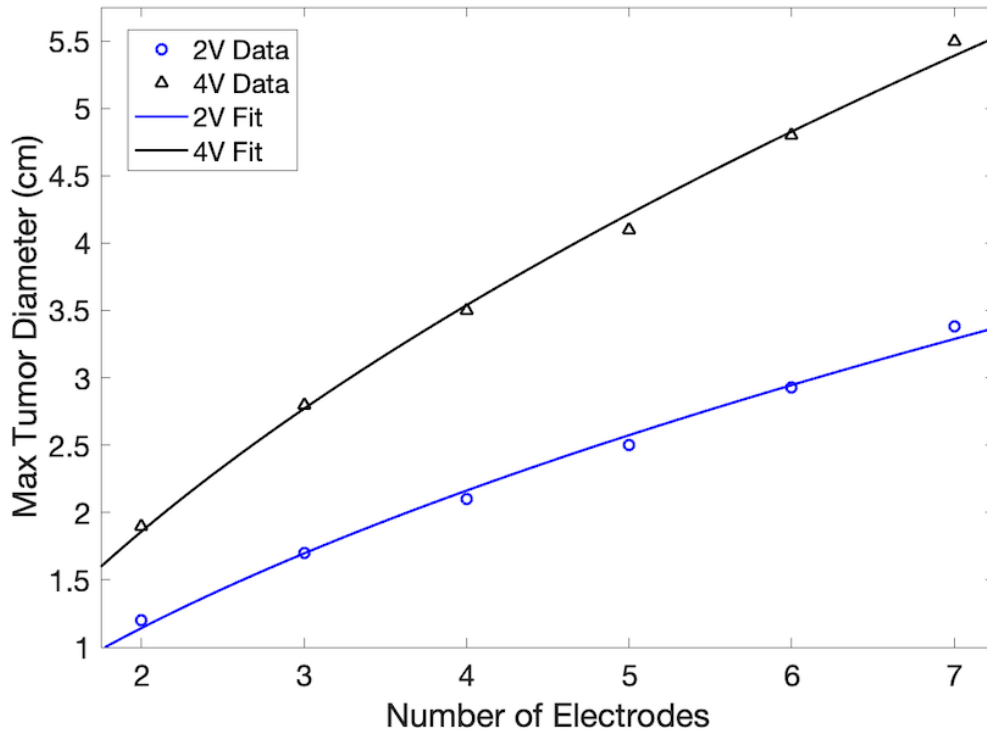


Figure 2.4: Maximum treatable tumour diameter (95% coverage of 95% of prescription 1 V/cm) for 2, 3, 4, 5, 6 and 7 single contact electrodes at both 2 V and 4 V input sine wave amplitudes. The data was fit to a function of $d = a\sqrt{n} + b$, where d is the tumour diameter, n is the number of electrodes, and a and b are fit parameters. With 7 electrodes, at 4 V, with optimal location and phase shift, tumours up to 5.5 cm diameter could be treated.

Multi-Contact Electrodes:

We further applied our optimization methods to multi-contact electrode models, with 2 or 3 contacts per electrode. The phase shift parameters of each additional contact were added to the optimization. Starting with a dual contact, 5 electrode model, the optimal configuration is equally spaced electrodes around a central electrode with phase shifts of the top contacts of $0, 0.6\pi, 1.4\pi, 0.6\pi, 1.4\pi$, and the bottom contacts $0, 0.4\pi, 1.6\pi, 0.4\pi, 1.6\pi$, relative to the top center electrode. When increasing the number of contacts to 2, our algorithm found an improvement in the objective function value when separating the phase of the top and bottom contact on an electrode. Compared to the optimal single

contact configuration $(0.5\pi, 1.5\pi, 0.5\pi, 1.5\pi)$, the top contacts were shifted by $+0.1\pi$, -0.1π , $+0.1\pi$, -0.1π , and the bottom contacts were shifted by -0.1π , $+0.1\pi$, -0.1π , $+0.1\pi$ (Figure 2.5).

Our algorithm was further applied to the 5-electrode, 3 contact model, where optimal phase shifts of contacts were $0, 0.37\pi, 1.63\pi, 0.37\pi, 1.63\pi$ for top contacts, $0.10\pi, 0.51\pi, 1.58\pi, 0.51\pi, 1.58\pi$ for middle contacts and $0.40\pi, 0.80\pi, 1.35\pi, 0.80\pi, 1.35\pi$ for bottom contacts, relative to the top center contact. By adding a third contact to each electrode the objective was further improved, and each contact on an electrode had separated phase shift (Figure 2.5). For single contact electrodes the electric field vectors rotate in cross sectional planes perpendicular to the electrode length. The addition of multiple contacts per electrode results in electric fields that vary in all three dimensions over time (Figure 2.6). These additional contact phase parameters increase the flexibility of field shaping to cover any tumour shape and result in electric field vector rotation in three dimensions.

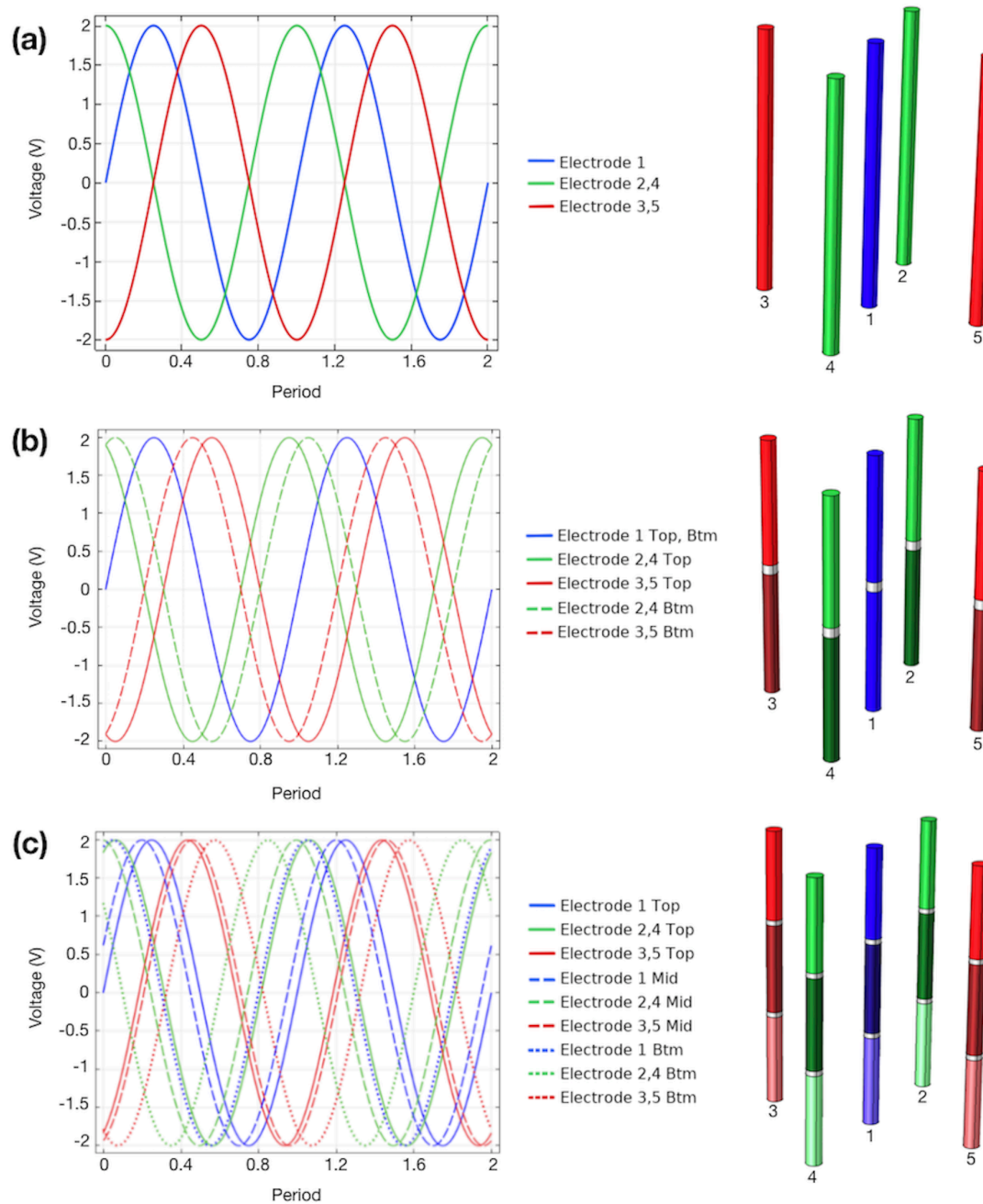


Figure 2.5: Input voltage sine waves of optimal phase shift configurations with corresponding contact geometries for (a) single contact, (b) 2 contacts, and (c) 3 contacts. Two periods of the waveforms are shown. Contacts of the same colour have the same phase shift, contacts of different hue of the same colour differ slightly in phase shift and different colours differ maximally in phase shift.

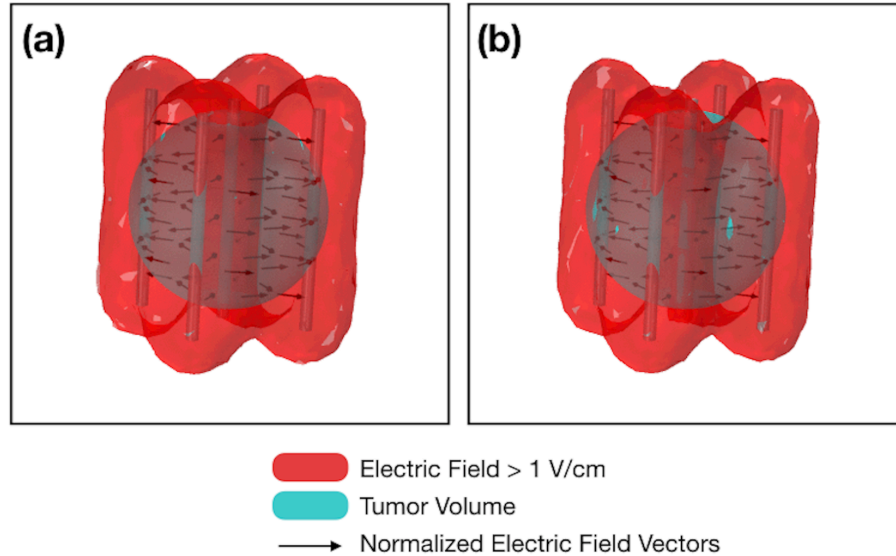


Figure 2.6: Animations of 1 V/cm isosurface coverage (red) of tumour volume (cyan) over time. Normalized electric field vectors show the field direction over time for both (a) single contact, 5 electrode and (b) 3-contact, 5 electrode models.

2.3.4 Tissue Sparing

Our algorithm was applied to the tissue sparing example, where optimal electrode placements (r, θ) were found to be $(0, 0)$, $(11, 0.37\pi)$, $(9, 0.75\pi)$, $(9, 1.25\pi)$, and $(11, 1.63\pi)$. Optimal phase shifts were 0 , 0.10π , 1.55π , 0.45π , and 1.9π radians. The input voltage required to ensure 95% of the tumour volume was covered by 95% of 1 V/cm was 2.4 V. The time average electric field map of the optimized configuration and corresponding EVH (Figure 2.7) highlight the coverage of the tumour volume with 1 V/cm electric field, while minimizing the field to the spared tissue.

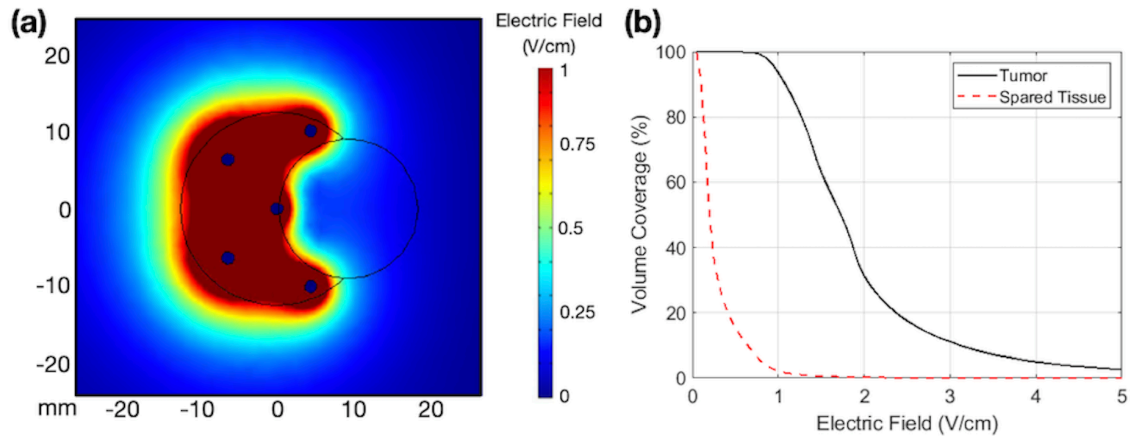


Figure 2.7: (a) Average temporal electric field maps and corresponding animations of field coverage over time for a 5-electrode tissue sparing example with optimally placed and programmed electrodes. (b) Electric field volume histogram of the percent tumour volume and spared tissue receiving at least a certain temporal average electric field value (V/cm).

2.4 Discussion

We have demonstrated that the problem of determining IMT treatment parameters can be cast as a mathematical optimization problem. Based on our results, it is clear that the use of relative phase shifts in the programming of electrode contacts allows for the custom design of location and time dependent electric vector fields that markedly enhance tumour coverage compared to non-phase shift settings (Figures 2.3, 2.6). By optimizing these parameters in addition to the electrode geometrical configuration and specific locations, we were able to maximize therapeutic field coverage for spherical tumours up to 5.5 cm diameter and incorporate tissue sparing.

From the optimization results presented in section 2.3.3. and figure 2.3 we have learned that for 2 to 4 electrodes, it is optimal to place electrodes equidistant from each other, and the centre, with equally spaced relative phase shifts. For 5 electrodes, with the increase in treatable tumour size, it becomes optimal to place an electrode in the centre, with 4 equally spaced surrounding electrodes. In general, the uniform distribution of electrodes within the tumour volume is the optimal configuration for all models we tested (Figure

2.3). Based on this knowledge, optimizations could be improved by starting with electrodes uniformly distributed and optimizing the distance from the centre and phase configurations for specific tumours.

By increasing the number of electrodes used, the maximum treatable spherical tumour diameter is increased from < 1 cm for a single stimulating electrode to 1.2 cm, 1.7 cm, 2.1 cm, 2.5 cm, 2.9 cm, and 3.4 cm for 2, 3, 4, 5, 6 and 7 electrodes respectively for a 2 V amplitude input waveform (Figure 2.4). By increasing the input voltage amplitude to 4 V, the treatable tumour diameter is increased to 1.9 cm, 2.8 cm, 3.5 cm, 4.1 cm, 4.8 cm, and 5.5 cm respectively (Figure 2.4). The results presented for maximum tumour diameter versus number of electrodes (Figure 2.4) were fit to the function $d = a\sqrt{n} + b$, as we expect that with additional electrodes, this relationship will approach an approximate square root dependence. The reason is as follows: Adding electrodes does not impact the ability to cover the longitudinal axis of the tumour (electrode length is always sufficient to cover this axis), but it does change the coverage of the cross-sectional plane of the tumour volume. Placement and phase shift optimization will spread the voltage gradients between electrodes spatially, maximizing the electric field coverage. As a result, after optimized for placement and phase shifts, each electrode will cover a similar area. Therefore, adding an electrode will increase the coverage area approximately linearly. Since the target coverage cross-sectional area varies with the square root of target radius (or diameter), we concluded that the target diameter coverage would vary with the square root of the number of electrodes. Up to the small range of 7 electrodes, the maximally covered tumour diameter almost appears to be linearly dependent on the number of electrodes.

In contrast to the additive effects of radioisotopes in brachytherapy, electric fields produced from multiple sources follow vector addition, leading to possible increased or decreased electric field strengths. The field cancellation feature can be exploited in tissue sparing situations. Hence, finding the locations and phase shifts to maintain sufficient field coverage within the tumour become increasingly complex and unintuitive with each additional electrode and the inclusion of critical structures. Such relationships will be further investigated in future studies. Incorporating tissue sparing into the objective

function resulted in the tumour volume being covered by the desired 1 V/cm electric field, while minimizing the field delivered to an intersecting sensitive structure (Figure 2.7, section 2.3.4.). The configuration and phase setting rules presented in this study (Figure 2.3, section 2.3.3.) were found to apply to frequencies up to 500 kHz, tumour conductivities between 0.2 and 0.3 S/m, and tumour dielectrics between 500 and 4000 (section 2.3.1.).

These results provide a set of rules as initial number, configurations, and parameters for patient-specific IMT treatment planning, where the size of tumour will be used to determine the number of electrodes required to cover that volume. If the patient tumour is approximately spherical, such as diffuse intrinsic pontine gliomas⁴², the configurations and phase settings outlined here for 2-7 electrodes could be used with distance from centre optimization. If the patient tumour shape is irregular, the configurations and settings could be used as a starting point for a full location and phase optimization. The optimization methods and results presented here will be validated by applying our methods to *in vitro*, *in vivo* and in human brain phantom experiments in the future.

This phase shifting approach to temporal electric field delivery maximizes the size of tumours that are possible to treat, while minimizing the number of electrodes. In addition, by incorporating multiple individually programmable contacts on each electrode, we were able to further improve the field coverage, and field shaping. Being able to control and optimize the distribution of the electric field produced, these methods could be further applied to irregularly shaped patient-specific tumour contours in the future. Multiple contacts on each electrode increase the flexibility of our model, to adapt the electric fields to any tumour shape. Our objective function was also updated to incorporate tissue sparing and could be further modified to include tumour tissue inhomogeneity weighting terms or adding a penalty term that would minimize the amount of power a configuration would require. In addition to increasing the magnitude of the temporal field coverage, incorporating relative phase shifts results in the electric field vector continuously changing direction. It has yet to be determined whether changing the direction of the electric field facilitates tumour cell death, but our method provides the capability to examine this hypothesis by designing experiments to investigate rotating

field effects on the dielectrophoretic force hypothesis^{14,43-45}, mitotic spindle microtubule interaction hypothesis^{14,43-45}, and cell membrane effects⁴⁶. The application of our algorithm to design an *in vitro* experiment to investigate rotating fields can be found in the appendix. Such data could play a substantial role in informing future IMT advances.

Limitations of this study include the use of equal depth parallel electrodes. In reality, electrodes could have different insertion angles with different insertion depths. In future studies, this could be rectified by incorporating electrode angle and depth into the optimization simulations and by varying the input voltage amplitudes along the contacts of each electrode to compensate for differing separations along the electrode length. The tumour models investigated in this study utilized scalar conductivity, and while the sensitivity analysis showed anisotropies between 0.2 and 0.3 S/m would have minimal effect (<1%) on the electric field (section 2.3.1.), anisotropies outside this range could impact the distribution. Future studies will include patient-specific planning with anisotropies. Another limitation is that implanted electrodes result in a steep field gradient near the electrode surface, and while our optimization alleviated this and maximized the coverage, inhomogeneous fields remained as in brachytherapy. Similar to the comparison between external beam radiotherapy and brachytherapy, external electric field delivery could create more homogeneous fields, but the internal delivery has its benefits, such as reaching tumours in the deep brain and brainstem with more sparing capability for organs at risk and providing a continuous treatment with no devices directly attached to the scalp which requires a shaved head. Heating mechanisms associated with implanted electrodes were also considered, to ensure that implanting electrodes at IMT voltages (2 V - 4 V) and frequency (200 kHz) would not result in adverse tissue heating or theoretical limitations to clinical implementation. At the low voltages proposed for IMT, Joule heating would theoretically contribute <0.8°C to tissue directly adjacent the electrode surface, falling off with distance from the electrode⁴⁷. At the intermediate frequency of 200 kHz, heating from dielectric losses are negligible, with the dielectric relaxation time of brain tissue remaining below the input waveform period, minimizing dielectric losses^{5,10-11,48}. Limitations in the optimization algorithm pipeline include long computation times and manual input requirements which will need to be rectified before clinical implementation.

These baseline optimizations were performed on spherical tumour models in order to determine a set of rules for IMT treatment planning optimization. The optimization methods have been designed to allow users to input the required tissue electrical properties, import the tumour volume, choose the field threshold, and perform an optimization to find optimal electrode programming and placement. The incorporation of multiple separately programmable contacts on each electrode could allow for the optimization of irregularly shaped tumours to produce unique field coverage patterns. In addition, our algorithm can incorporate tissue sparing and organs at risk to minimize field exposure outside of the tumour. Overall, our optimization algorithm could be applied to any patient-specific tumour model, for different electrode designs and optimization parameters.

2.5 Conclusions

Our methods for temporally optimizing the electric field coverage with respect to relative phase shift programming, geometrical configurations, electrode and contact numbers for IMT are the first of their kind and have the adaptability to be able to incorporate a wider range of optimization parameters and tumour shapes/types in future investigations. This study has provided a baseline investigation and presentation of an optimization method for multi-electrode IMT, considering spherical tumour models. Current limitations include the use of parallel electrodes of equal depth, and the electric field inhomogeneities inherent to internal electrode placement. Overall, we have demonstrated the capability to optimize electrode placement and stimulation settings using methods developed specifically for IMT. These baseline tumour electrode configurations and phase setting rules are a critical first step in developing a patient-specific treatment planning system for IMT.

2.6 Appendix

Proposed In Vitro Experiment

Our optimization algorithm was used to design a multi-electrode in vitro experiment to test the effects of electric field rotation. Four electrodes of 0.8 mm radius in a 1.75 cm

radius in vitro dish were simulated in COMSOL. We first utilized our optimization algorithm to determine the 4-electrode geometry and input voltage amplitude of each electrode that results in a 1 V/cm amplitude rotating electric field within a $0.5 \text{ cm} \times 0.5 \text{ cm}$ viewing window. The updated objective function $F = \frac{1}{N_s} \sum_j (\overline{E}_j - E_{pres})^2$ is the square difference of the average temporal electric field and the prescription 1 V/cm field.

The closer the majority of voxels are to 1 V/cm, the lower the objective value. Since we are looking at a 4-electrode rotating model, phase shifts for this optimization were set to $0, 0.5\pi, \pi, 1.5\pi$ radians, and electrodes were equally spaced. The optimization algorithm was used to find the optimal input voltage and distance from the center of the electrodes, to ensure a continuous 1 V/cm is applied in the viewing window. Next, our optimization algorithm was used to determine the placement of electrodes and amplitude of input square waves that result in a 1 V/cm non-rotating electric field.

We found that equally spaced electrodes placed 1.5 cm from the center with input voltage amplitudes of 5.17 V led to a continuously rotating electric field of 1.00 ± 0.01 V/cm temporal average within the viewing window. The non-rotating electric field optimization resulted in all 4 electrodes placed 1.27 cm from the center at angles of ± 0.488 and ± 2.663 radians with alternating input voltages of 5.17 V and 0 V. This led to a time average electric field of 1.00 ± 0.03 V/cm (Figure 2.8).

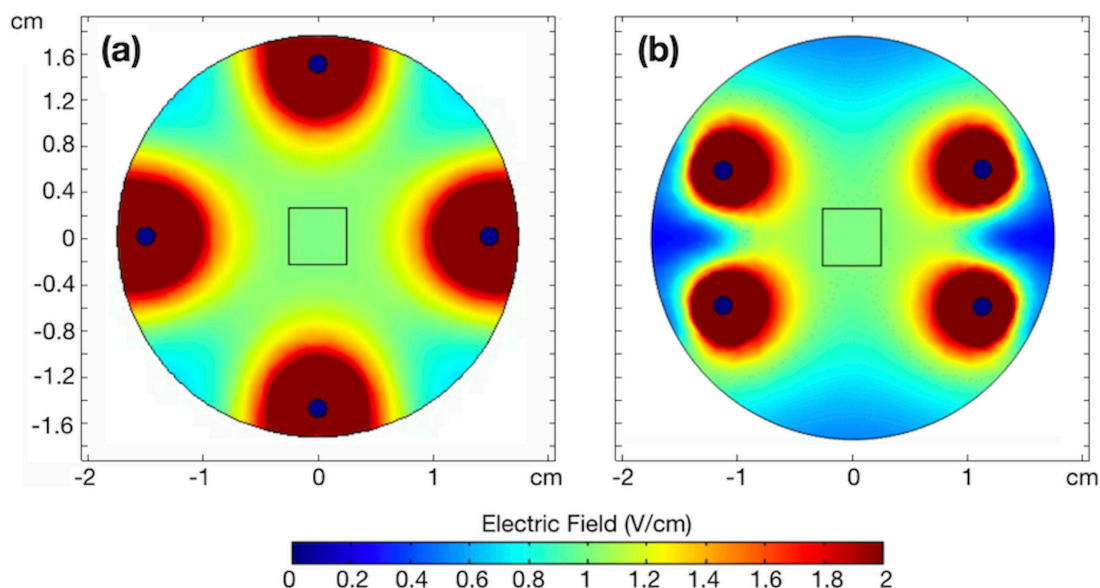


Figure 2.8: Time average electric field magnitude (V/cm) for (a) rotating electric field and (b) non-rotating electric field. (Animation includes field vectors).

2.7 Acknowledgements

This work was supported in part by NSERC CGS-M (E.I.), NSERC Discovery Grant, Cancer Research Society, and Western Innovation Fund.

2.8 Conflicts of Interest

M.O.H. and S.S. are inventors on the following patent applications that are assigned to “London Health Sciences Centre Research Inc.” (the applicant): PCT/CA2016/050556 entitled “Intratumoral Modulation Therapy” and corresponding national phase applications in Canada, United States, Europe and China. E.W., M.O.H., T.P., and S.S. are inventors on the following patent application that is assigned to “London Health Sciences Centre Research Inc.” (the applicant): US provisional Serial No. 62/962,553 entitled “Planning and delivery of dynamically oriented electric field for biomedical applications”. The authors have no other competing interests.

2.9 References

1. Hottinger AF, Pacheco P, Stupp R. Tumor treating fields: A novel treatment modality and its use in brain tumors. *Neuro Oncol.* 2016;18(10):1338-49. doi:10.1093/neuonc/now182.
2. Swanson KD, Lok E, Wong ET. An Overview of Alternating Electric Fields Therapy (NovoTTF Therapy) for the Treatment of Malignant Glioma. *Curr Neurol Neurosci Rep.* 2016;16(1):8. doi:10.1007/s11910-015-0606-5.
3. Stupp R, Taillibert S, Kanner A, et al. Effect of tumor-treating fields plus maintenance temozolomide vs maintenance temozolomide alone on survival in patients with glioblastoma a randomized clinical trial. *JAMA - J Am Med Assoc.* 2017;318(23):2306-2316. doi:10.1001/jama.2017.18718.
4. Kirson ED, Dbaly V, Tovarys F, et al. Alternating electric fields arrest cell proliferation in animal tumor models and human brain tumors. *Proc Natl Acad Sci U S A.* 2007;104(24):10152-10157. doi:10.1073/pnas.0702916104.
5. Kirson ED, Gurvich Z, Schneiderman R, et al. Disruption of cancer cell replication by alternating electric fields. *Cancer Res.* 2004;64(9):3288-3295. doi:10.1158/0008-5472.can-04-0083.
6. Lok E, San P, Hua V, Phung M, Wong ET. Analysis of physical characteristics of Tumor Treating Fields for human glioblastoma. *Cancer Med.* 2017;6(6):1286-1300. doi:10.1002/cam4.1095.
7. Wenger C, Salvador R, Basser PJ, Miranda PC. Improving Tumor Treating Fields Treatment Efficacy in Patients with Glioblastoma Using Personalized Array Layouts. *Int J Radiat Oncol Biol Phys.* 2016;94(5):1137-43. doi:10.1016/j.ijrobp.2015.11.042.
8. Wenger C, Salvador R, Basser PJ, Miranda PC. The electric field distribution in the brain during TTFields therapy and its dependence on tissue dielectric properties and anatomy: A computational study. *Phys Med Biol.* 2015;60(18):7339-57. doi:10.1088/0031-9155/60/18/7339.
9. Korshoej AR, Saturnino GB, Rasmussen LK, Von Oettingen G, Sørensen JCH, Thielscher A. Enhancing predicted efficacy of tumor treating fields therapy of glioblastoma using targeted surgical craniectomy: A computer modeling study. *PLoS One.* 2016;11(10):e0164051. doi:10.1371/journal.pone.0164051.
10. Deweyert A, Iredale E, Xu H, Wong E, Schmid S, Hebb MO. Diffuse intrinsic pontine glioma cells are vulnerable to low intensity electric fields delivered by intratumoral modulation therapy. *J Neurooncol.* 2019;143:49-56. doi:10.1007/s11060-019-03145-8.
11. Di Sebastiano AR, Deweyert A, Benoit S, et al. Preclinical outcomes of Intratumoral Modulation Therapy for glioblastoma. *Sci Rep.* 2018;8:7301. doi:10.1038/s41598-018-25639-7.

12. Xu H, Bihari F, Whitehead S, Wong E, Schmid S, Hebb MO. In vitro validation of intratumoral modulation therapy for glioblastoma. *Anticancer Res.* 2016;36(1):71-80.
13. Naveh A, Bomzon Z, Farber O, et al. Transducer array configuration optimization for treatment of pancreatic cancer using Tumor Treating Fields (TTFields). *Cancer Res.* 2018;78(13): 2. doi:10.1158/1538-7445.AM2018-3204.
14. Wenger C, Miranda PC, Salvador R, et al. A Review on Tumor-Treating Fields (TTFields): Clinical Implications Inferred From Computational Modeling. *IEEE T Bio-Med Eng.* 2018;11:195-207. doi:10.1109/RBME.2017.2765282.
15. Miranda PC, Mekonnen A, Salvador R, Basser PJ. Predicting the electric field distribution in the brain for the treatment of glioblastoma. *Phys Med Biol.* 2014;59(15):4137-47. doi:10.1088/0031-9155/59/15/4137.
16. Sung J, Seo J, Jo Y, Yoon M, Hwang SG, Kim EH. Development of a Method for Improving the Electric Field Distribution in Patients Undergoing Tumor-Treating Fields Therapy. *J Korean Phys Soc.* 2018;73:1577-1583. doi:10.3938/jkps.73.1577.
17. Cubo R, Fahlström M, Jiltsova E, Andersson H, Medvedev A. Calculating deep brain stimulation amplitudes and power consumption by constrained optimization. *J Neural Eng.* 2019;16(1):016020. doi:10.1088/1741-2552/aaceb7.
18. Adeyanju OO, Al-Angari HM, Sahakian AV. The optimization of needle electrode number and placement for irreversible electroporation of hepatocellular carcinoma. *Radiol Oncol.* 2012;46(2):126-135. doi:10.2478/v10019-012-0026-y.
19. Garcia PA, Kos B, Rossmeisl Jr JH, Pavilha D, Miklavčič D, Davalos RV. Predictive therapeutic planning for irreversible electroporation treatment of spontaneous malignant glioma. *Med Phys.* 2017;44(9):4968-4980. doi:10.1002/mp.12401.
20. Ballo MT, Urman N, Lavy-Shahaf G, Grewal J, Bomzon Z, Toms S. Correlation of Tumor Treating Fields Dosimetry to Survival Outcomes in Newly Diagnosed Glioblastoma: A Large-Scale Numerical Simulation-Based Analysis of Data from the Phase 3 EF-14 Randomized Trial. *Int J Radiation Oncol Biol Phys.* 2019;104(5):1106-1113. doi:10.1016/j.ijrobp.2019.04.008.
21. Korshoej AR, Sørensen JCH, von Oettingen GB, Poulsen FR, Thielscher A. Optimization of tumor treating fields using singular value decomposition and minimization of field anisotropy. *Phys Med Biol.* 2019;64(4): 9. doi:10.1088/1361-6560/aafe54.
22. Korshoej AR, Hansen FL, Thielscher A, von Oettingen GB, Sørensen JCH. Impact of tumor position, conductivity distribution and tissue homogeneity on the distribution of tumor treating fields in a human brain: A computer modeling study. *PloS One.* 2017;12(6):e0179214. doi:10.1371/journal.pone.0179214.
23. Dutreix A. Can we compare systems for interstitial therapy? *Radiother Oncol.* 1988;13(2):127-135. doi:10.1016/0167-8140(88)90033-3.

24. Gabriel C, Peyman A, Grant EH. Electrical conductivity of tissue at frequencies below 1 MHz. *Phys Med Biol*. 2009;54:4863-4878. doi:10.1088/0031-9155/54/16/002.
25. Latikka J, Kuurne T, Eskola H. Conductivity of living intracranial tissues. *Phys Med Biol*. 2001;46:1611-1616. doi:10.1088/0031-9155/46/6/302.
26. Stoy RD, Foster KR, Schwan HP. Dielectric properties of mammalian tissues from 0.1 to 100 MHz: a summary of recent data. *Phys Med Biol*. 1982;27(4):501-513. doi:10.1088/0031-9155/27/4/002.
27. Latikka J, Eskola H. The Resistivity of Human Brain Tumours In Vivo. *Ann Biomed Eng*. 2019;47(3):706-713. doi:10.1007/s10439-018-02189-7.
28. Lourtioz JM, Benisty H, Berger V, Gerard JM, Maystre D, Tchelakov A. Photonic Crystals: Towards Nanoscale Photonic Devices. *Springer*. 2008; pp. 122-123.
29. CSNDT Conductivity of Materials. Eddy Current Testing Manual on Eddy Current Method, Non-Destructive Testing Magazine Sept/Oct 1955, Cosgrove Article.
30. Amon A, Alesch F. Systems for deep brain stimulation: review of technical features. *J Neural Transm (Vienna)*. 2017;124(9):1083-1091. doi:10.1007/s00702-017-1751-6.
31. Butson C, McIntyre C. Role of electrode design on the volume of tissue activated during deep brain stimulation. *J Neural Eng*. 2006;3(1):1-8. doi:10.1088/1741-2560/3/1/001.
32. Alonso F, Latorre MA, Goransson N, Zsigmond P, Wardell K. Investigation into Deep Brain Stimulation Lead Designs: A Patient-Specific Simulation Study. *Brain Sci*. 2016;6(3). doi:10.3390/brainsci6030039.
33. Anderson DN, Osting B, Vorwerk J, Dorval AD, Butson CR. Optimized programming algorithm for cylindrical and directional deep brain stimulation electrodes. *J Neural Eng*. 2018;15(2):026005. doi:10.1088/1741-2552/aaa14b.
34. Wieser HP, Cisternas E, Wahl N, et al. Development of the Open-Source Dose Calculation and Optimization Toolkit matRad. *Med Phys*. 2017;44(6):2556-2568. doi:10.1002/mp.12251.
35. Orton CG, Bortfeld TR, Niemierko A, Unkelbach J. The role of medical physicists and the AAPM in the development of treatment planning and optimization. *Med Phys*. 2008;35(11):4911-4923. doi:10.1118/1.2990777.
36. Boyd SP, Vandenberghe L. *Convex Optimization*. Cambridge University Press. 2004.
37. Amaran S, Sahinidis NV, Sharda B, Bury SJ. Simulation optimization: a review of algorithms and applications. *Ann Oper Res*. 2016;240(1):351-380. doi:10.1007/s10479-015-2019-x.
38. Nocedal J, Wright SJ. *Numerical Optimization*. New York: Springer; 2006.
39. Lange K. *Optimization*. New York: Springer; 2013.

40. International Commission on Radiation Units and Measurements. ICRU Report 62: Prescribing, recording and reporting photon beam therapy (Supplement to ICRU report 50). 1999.
41. Murthy KK, Shukeili KA, Kumar SS, Davis CA, Chandran RR, Namrata S. Evaluation of dose coverage to target volume and normal tissue sparing in the adjuvant radiotherapy of gastric cancers: 3D-CRT compared with dynamic IMRT. *Biomed Imaging Interv J*. 2010;6(3):e29. doi:10.2349/bijj.6.3.e29.
42. Matthew RK, Rutka JT. Diffuse Intrinsic Pontine Glioma: Clinical Features, Molecular Genetics, and Novel Targeted Therapeutics. *J Korean Neurosurg Soc*. 2018;61(3):343-351. doi:10.3340/jkns.2018.0008.
43. Wenger C, Giladi M, Bomzon Z, Salvador R, Bassar PJ, Miranda PC. Modeling Tumor Treating Fields (TTFields) application in single cells during metaphase and telophase. *Conf Proc IEEE Eng Med and Biol Soc*. 2015;6892-5. doi:10.1109/EMBC.2015.7319977.
44. Gera N, Yang A, Holtzman TS, Lee SX, Wong ET, Swanson KD. Tumor treating fields perturb the localization of septins and cause aberrant mitotic exit. *PLoS One*. 2015;10(5):e0125269. doi:10.1371/journal.pone.0125269.
45. Berkelmann L, Bader A, Meshksar S, et al. Tumor-treating fields (TTFields): Investigations on the mechanism of action by electromagnetic exposure of cells in telophase/cytokinesis. *Sci Rep*. 2019;9:7362. doi:10.1038/s41598-019-43621-9.
46. Chang E, Patel CB, Pohling C, et al. Tumor treating fields increases membrane permeability in glioblastoma cells. *Cell Death Discov*. 2018;4:113. doi:10.1038/s41420-018-0130-x.
47. Elwassif MM, Kong Q, Vazquez M, Bikson M. Bio-heat transfer model of deep brain stimulation-induced temperature changes. *J Neural Eng*. 2006;3(4)306-315. doi:10.1088/1741-2560/3/4/008.
48. Lok E, Sajo E. Fundamental Physics of Tumor Treating Fields. In: Wong E. *Alternating Electric Fields Therapy in Oncology*. Springer. 2016;15-27.

Chapter 3

3 Planning System for the Optimization of Electric Field Delivery using Implanted Electrodes for Brain Tumour Control

This chapter was adapted from the published article entitled “Planning system for the optimization of electric field delivery using implanted electrodes for brain tumor control” by Erin Iredale, Brynn Voigt, Adam Rankin, Kyungho W. Kim, Jeff Z. Chen, Susanne Schmid, Matthew O. Hebb, Terry M. Peters, and Eugene Wong, Medical Physics, 49(9):6055-6067 (2022). Permission to reproduce can be found in Appendix A.

3.1 Introduction

Electric fields from low intensity voltage sources are showing increasing promise as a treatment modality for brain cancer¹⁻¹⁰. Intratumoural Modulation Therapy (IMT) is an emerging technique intended to restrict tumour growth by applying low intensity electric fields using bio-electrodes implanted within or adjacent to tumour volumes⁷⁻¹⁰. Preclinical *in vitro* and *in vivo* investigations into the application of 200 kHz, low intensity (± 2.00 V stimulation) electric fields to glioblastoma (GBM) and diffuse intrinsic pontine glioma (DIPG) cells have shown the efficacy of this modality as a monotherapy⁹, and in conjunction with chemotherapy and radiation⁸. A single stimulating electrode paradigm was implemented in these early studies, but computer simulations and optimization studies have since prompted the use of multiple stimulating electrodes with optimized relative phase shifts of input waveforms to increase the coverage capacity of the IMT fields⁷. The previous IMT optimization study⁷ established a method for temporally maximizing tumour coverage from IMT electric fields. This algorithm allowed for electrode location and stimulation phase shift parameters to be optimized for multiple electrodes, each with multiple separately programmable contacts. The phase shifting of each electrode contacts' sinusoidal voltage waveform creates an electric field that rotates in 3D in both directionality and intensity, over the waveform period. A simplified spherical tumour model with parallel electrodes was used in this previous

study, which requires extension into patient-specific models with non-parallel electrodes defined by insertion and tip coordinates.

While the primary mechanism of low intensity electric fields has yet to be definitively elucidated, there are several mechanisms that have been suggested to play a role in selective tumour control. These include anti-mitotic mechanisms, enhanced cell membrane permeability, increased immunogenic cell death, impairment of DNA repair, anti-migratory, and autophagic influences¹¹⁻¹⁵. The most well supported theories remain anti-mitotic, where mitotic spindle and septin ring formation are impacted in metaphase and cytokinesis respectively¹⁶⁻¹⁸, and impact on cell membrane permeability, which has been observed experimentally¹⁹. While the synergistic mechanisms of action and their effects on tumour control are still under investigation, the applied electric field is the basis of each proposed mechanism. With tumour control found experimentally to depend on electric field intensity and frequency¹⁷, maximizing the tumour coverage with threshold electric field magnitudes is the current therapy objective.

A review of the published literature on treatment planning systems that simulate the electric field from electrode sources highlighted both external and internal electrode applications. The clinical use of an external electric field device for glioblastoma (NovoTTFTM), using a treatment planning system (NovoTALTM)^{2,4,20-22} establishes personalized array layouts, found through simulation studies to enhance electric field coverage to certain brain regions²³. A recent optimization study of electric fields from the external device highlighted the importance of minimizing the anisotropy of electric field components while maintaining field intensity²⁴, supporting the use of rotating fields in IMT. Similarly, both deep brain stimulation (DBS) to treat neurological disorders²⁵⁻³⁰ and irreversible electroporation (IRE) to ablate tumour volumes³¹⁻³⁵ require electric field and implanted electrode trajectory planning to reach the target volume. Stereoelectroencephalography (SEEG) uses multiple depth electrodes implanted in the brain to identify seizure zones, with robotic and computer assisted trajectory planning gaining interest³⁶⁻³⁸. Treatment planning systems play a large role in radiotherapy, including brachytherapy³⁹⁻⁴⁶, where the radiation dose to patient-specific targets and organs at risk (OAR) are analyzed and treatments are planned accordingly. IMT differs

from external electric fields devices in that electrodes are implanted directly in or adjacent tumour volumes, requiring trajectory planning of multiple electrodes. Advantages of long-term implanted IMT electrodes compared to external electric field devices are the potential for improved quality of life, similar to DBS, which is well tolerated, and the potential to reach tumours deep in the brain. The goal of IMT is to cover a large tumour volume ($> 1 \text{ cm}^3$) with intermediate frequency (200 kHz) electric field using multiple electrodes, to avoid neural activation, as opposed to DBS where a small volume ($\sim 1 \text{ mm}^3$) is commonly targeted by one or two low frequency electrodes ($\sim 130 \text{ Hz}$) to initiate neural activation³⁰. While the goal of electroporation is to ablate a tumour volume using multiple electrodes³³, the permanent implantation and low intensity nature of IMT fields requires additional optimization considerations, where we maximize the electric field tumour coverage with minimal input voltage, achieved by optimizing relative phase shifts of the delivered waveforms between electrode contacts⁷. Lastly, radiotherapy treatments consider the delivered ionizing radiation dose to the tumour volume and nearby organs at risk, whereas IMT considers non-ionizing electric fields that interfere with one another. The differences between IMT and other modalities necessitate the creation of a custom treatment planning system for IMT.

To accompany ongoing *in vitro* and *in vivo* validations of IMT, the preparation for future single center patient safety and efficacy trials will require a way to plan animal and patient-specific electrode trajectories and stimulation programming to cover their tumour with a threshold electric field. Precursory pathways from preclinical to clinical investigations substantiate the need for a treatment planning system to be developed. To advance this technology to allow clinical testing, optimal treatment parameters and electrode configurations on a patient-specific basis are required. In this study, the treatment stimulation parameters and electrode placement are determined by designing a treatment planning system that utilizes and expands upon the IMT optimization algorithm previously established⁷. The goal of this study is to amalgamate the numerous steps in the optimization pipeline into a cohesive, user-friendly system using the 3D Slicer^{47,48} platform and to validate the trajectories and plan in a brain phantom. All planning steps are accessed in a single application with ordered steps, with options for pre-operative or post-operative planning, human or preclinical *in vivo* animal planning, and different

electrode models (multi-contact cylindrical electrodes, custom electrode arrays, or preclinical multi-electrode wire constructs).

The completed system allows the user to upload, segment and smooth the patient magnetic resonance imaging (MRI) or computed tomography (CT) data, plan the electrode trajectories, and optimize the electrode tip location, phase shift, and voltage parameters. The treatment planning system was validated by completing a treatment plan on a phantom brain model and implanting the electrodes using a neurosurgical robot (Neuromate[®])⁴⁹ to demonstrate the full treatment pipeline, encompassing implantation, field delivery, and post-operative planning adjustment. The IMT treatment planning system development provides an essential step in advancing future clinical studies.

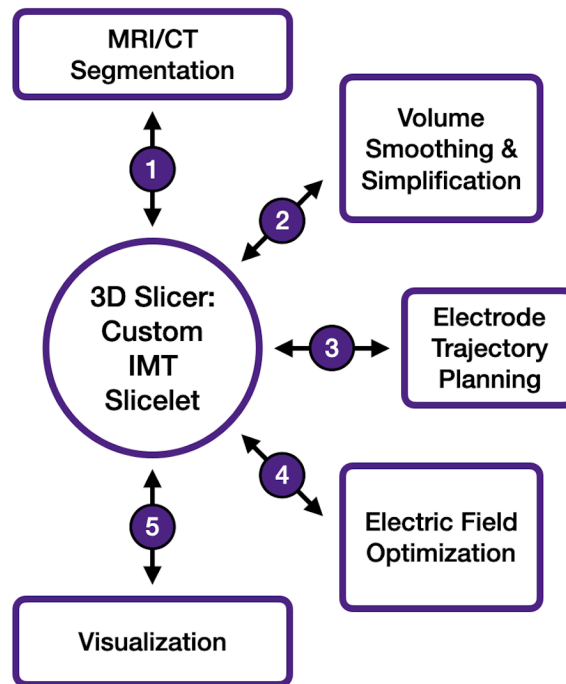


Figure 3.1: Pipeline of custom IMT Slicelet in 3D Slicer including the tissue segmentation, smoothing and simplification of segmented volumes (custom module), electrode trajectory planning (custom module), electric field optimization (custom module) and the visualization of the completed optimized treatment plan (custom module).

3.2 Materials and Methods

3.2.1 Slicelet Design

The user interface for the IMT treatment planning system was developed in a custom 3D Slicer application, called a Slicelet⁵⁰. A Slicelet is a custom coded application that combines all necessary modules into a numbered pipeline. The design of the custom IMT Slicelet (Figure 3.1) begins with the setup, which includes patient selection and DICOM import (create new patient or open existing patient), the selection of patient type (human or preclinical), and the patient status (pre-operative or post-operative) (Appendix D: Figure D.1(a)).

After setup of the patient model, the planning process includes five main steps: 1) segmentation of brain, tumour, organ at risk, and surgical resection cavity volumes, 2) the smoothing of the segmented volumes, 3) the planning of electrode implantation coordinates, 4) the optimization of tip coordinates, phase shift and voltage amplitude, and 5) visualization of results. Step 1 is included as the built-in segmentation module in 3D slicer, where users can segment the brain and tumour regions using any of the existing 3D Slicer segmentation features including paint, draw, erase, level tracing, fill between slices, threshold, margin, smoothing and islands. Steps 2-4 are custom coded modules explained in sections 3.2.2-3.2.3. Step 5 is the custom coded visualization module, which displays the numerical results of the optimization (electrode coordinates, phase shift, voltage amplitude) in tables. The electrode locations are also visualized as an interactive 3D model of the brain, tumour, and electrodes. An electric field volume histogram (EVH) is displayed showing the percent of tumour (and organ at risk) volume covered by at least the corresponding electric field. The resulting time average electric field maps are displayed on the MR or CT image as coronal, sagittal, and axial interactive slices. Built-in 3D Slicer Models⁵¹ and Volumes⁵² modules were added to allow users to adjust the DICOM image parameters and 3D volume displays.

3.2.2 Smoothing and Electrode Implantation Modules

The custom smoothing module (Appendix D: Figure D.1(b)) utilizes the Python command line interface to access selected MeshLab (v2021.05) filters to smooth and

simplify brain, tumour, organ at risk, and surgical resection cavity volumes. The selected filter options include Quadratic Edge Collapse Decimation (simplification), Laplacian Smooth, HC Laplacian Smooth, Uniform Mesh Resampling, Clustering Decimation (simplification), Smooth Face Normals and Merge Close Vertices. A Run Filters button allows users to continue smoothing and simplifying with different filters until the target file size is reached (<100 kB). Real time display of the smoothed volumes and contours on image slice views are included to ensure accuracy is maintained and volumes haven't been oversimplified.

The custom electrode implantation module (Appendix D: Figure D.1(c)) uses the Python command line interface for the placement of fiducial points. Based on the number of electrodes selected, the locations of the insertion and tip coordinates for each electrode are selected on the MR or CT image by the user. Also included is the ability to import existing electrodes.

3.2.3 Optimization Module

The optimization module (Appendix D: Figure D.1(d)) requires connection to pre-existing MATLAB (v2021a) code⁷ that communicates with COMSOL Multiphysics (v5.4) for model creation and electric field computation at each iteration using the COMSOL-MATLAB Livelink. A MATLAB function was created to connect to the Livelink automatically and run the optimization code. This function is connected to the 3D Slicer module graphical user interface (GUI) inputs using the 3D Slicer MATLAB Bridge. The existing optimization code was updated to automatically generate a unique COMSOL model based on the user inputs at the start of an optimization (smoothed volumes, patient type (human or preclinical), pre-operative or post-operative, organ at risk or resection cavity presence). The COMSOL model build generates cylindrical multi-contact electrodes with customizable contact height, spacing, and radius, with default values included (0.800 mm radius, 5.00 mm contact height, 1.00 mm contact spacing) for human models, or wire electrodes (0.125 mm radius, 3.00 mm contact height) for preclinical models.

To automatically generate cylindrical electrodes in COMSOL, the insertion coordinate, electrode length, and spherical coordinates of the electrode trajectory are required. Electrode length (Eqn. 3.1), and spherical coordinates θ (Eqn. 3.2) and Φ (Eqn. 3.3) are calculated for each electrode using the insertion coordinates (x_{in}, y_{in}, z_{in}) and tip coordinates $(x_{tip}, y_{tip}, z_{tip})$.

$$L = \sqrt{(x_{in} - x_{tip})^2 + (y_{in} - y_{tip})^2 + (z_{in} - z_{tip})^2} \quad (3.1)$$

$$\theta = \cos^{-1} \left[-\frac{(z_{in} - z_{tip})}{L} \right] \quad (3.2)$$

$$\Phi = -\frac{y_{in} - y_{tip}}{|y_{in} - y_{tip}|} \cos^{-1} \left[-\frac{x_{in} - x_{tip}}{\sqrt{(x_{in} - x_{tip})^2 + (y_{in} - y_{tip})^2}} \right] \quad (3.3)$$

Contacts are generated along the electrode length by using calculated coordinates (x_c, y_c, z_c) for each contact based on the contact spacing cs , contact length cl and contact number n (Eqn. 3.4).

$$x_c = x_{in} + (x_{tip} - x_{in}) \left[\frac{L - n(cl + cs) - cs}{L} \right] \quad (3.4)$$

At each iteration of the pattern search optimization, the electric field is calculated from the COMSOL model for the list of iteration parameters. The mesh size for all geometrical entities is dependent on the material, with electrodes and contacts as a fine mesh size (1.73 mm - 13.8 mm element size), tumour as a normal mesh (3.11 mm - 17.3 mm element size), and surrounding brain as a course mesh (4.84 mm - 25.9 mm element size). Validation of the material dependent mesh sizes was completed to ensure convergence to the more accurate solution using the finest material independent mesh sizes (0.035 mm – 3.5 mm). The use of different mesh sizes allows for preservation of accuracy within the tumour volume and around electrodes while minimizing nodes in the surrounding brain to improve computation time. The electric field is computed using COMSOL's AC/DC electric currents module, in the frequency domain at 200 kHz. To improve computation time, the electric field “kernel” is computed for each electrode contact at 1 V with all remaining contacts at 0 V. This allows for the superposition of

electric field (summation of electric field vectors from each voltage source contribution) to be used to compute the electric field distribution in MATLAB for the set of phase shift and voltage amplitude parameters for that geometry. For each electrode location change, the “kernel” fields are calculated in COMSOL, and for each phase shift or voltage change, only the superposition calculation is required as the “kernel” fields only need to be calculated upon a location change.

The previous requirement for manual MATLAB command line inputs was removed and replaced by buttons and boxes in the Slicelet GUI. The necessary inputs are set to default values, and include voltage amplitude limit (2V), prescription electric field (1 V/cm), brain and tumour electrical conductivity and dielectric (0.25 S/m and 3000 for brain, 0.24 S/m and 2000 for tumour^{23,53-60}), nearby organ at risk, the electrical properties and weighting factor of the organ at risk, and electrical properties of a surgical resection cavity. The choice of optimization type includes two options per electrode optimization: phase shift only, or location + phase shift. Three options are included for individual contact optimization: phase shift only, voltage amplitude only, or phase shift + voltage amplitude. The desired field coverage percentage, the use of a random starting point, and the option to save the COMSOL model file are all additional user selections.

Initial geometrical conditions for the optimization of electrode trajectories and programming are the user selected insertion and tip coordinates of each electrode. Insertion coordinates remain fixed, and the tip coordinates are an optimization variable, along with phase shift and voltage amplitude. A gradient free pattern search technique was used in the planning system, due to the non-convexity of the objective function⁷, to broadly search parameter space. The success of an iteration at finding an improved objective value determines if parameter step size is increased (successful) or decreased (unsuccessful) at the next iteration. The pattern search algorithm first minimizes the objective function f (Eqn. 3.5), which maximizes the voxels covered by the prescription electric field E_{pres} while simultaneously maximizing the electric field of uncovered voxels and minimizing the electric field to nearby organs at risk.

$$f = \frac{1}{N_s} \sum_{j \in S} H(E_{pres} - \bar{E}_j)(\bar{E}_j - E_{pres})^2 + w \frac{1}{NOAR} \sum_{i \in OAR} \bar{E}_i^2 \quad (3.5)$$

The Heaviside function (H) term differentiates tumour voxels j covered and uncovered by the prescription field, and the squared difference term weighs voxels with time average electric field \bar{E}_j closer to the prescription field preferably. The weighted OAR term minimizes the time average field \bar{E}_i to the OAR voxel i . The OAR weighting factor w is by default 0 unless an OAR is present. N_s represents the number of voxels in the tumour, and N_{OAR} is the number of voxels in the organ at risk volume.

The optimization of electric field conformity is included as a second step, to minimize the power consumption of active electrode contacts and to shape the field in 3D, by minimizing the electric field outside of the tumour while maintaining field coverage inside the tumour. The default objective function f (Eqn. 3.5) is changed to the inverse conformity index CI^{-1} (Eqn. 3.6) when this option is selected:

$$CI^{-1} = \frac{V_{E_{pres}}}{TV_{E_{pres}}} \quad (3.6)$$

where $V_{E_{pres}}$ is the total volume covered by at least the prescription electric field, and $TV_{E_{pres}}$ is the tumour volume covered by at least the prescription electric field. The inverse of the conformity index objective CI^{-1} is minimized by the pattern search algorithm, to minimize the electric field outside of the tumour. Display boxes show the prescription field coverage percentage and conformity index of the optimized electric field.

3.2.4 Planning System Testing

The complete treatment planning system pipeline was tested using two DICOM MRI datasets: a sample built-in 3D Slicer T1-weighted MRI of a human brain with a 3.5 cm diameter tumour⁶¹, and a T1-weighted MRI of a realistic brain phantom with a 1.9 cm diameter tumour in the frontal lobe (Synaptive Simulate, Toronto Canada)⁶². The human MRI was used to test the human pre-operative, post-operative surgical resection cavity, and pre-operative with organ at risk planning pathways. The phantom MRI was used to test the human pre-operative pathway using single and multiple insertion sites. The brain and tumour visible on MR images manually segmented using the paint, fill between

slices, draw, and smoothing features. The electrode dimensions used for the phantom model were customized in the planning system to mimic AdTech SEEG electrodes (Surgi-One Medical Technologies Inc. 0.430 mm radius, 2.29 mm contact height, 1.71 mm spacing). SEEG electrodes (0.860 mm diameter) were chosen over larger diameter DBS electrodes (1.27 mm)⁶³ based on the contact height and number of contacts per electrode (10) that would be sufficient to cover tumours with IMT fields. Optimization parameters for these models were chosen as the default values with a voltage limit of 4.00 V, prescription electric field of 1 V/cm, 95.0% desired tumour coverage, brain conductivity 0.25 S/m, brain dielectric 3000, tumour conductivity 0.24 S/m, and tumour dielectric 2000^{23,53-60}.

3.2.5 Phantom Electrode Implantation

Validation of the full pipeline implementation included a pre-operative CT of a brain phantom (Synaptive), used to plan the tip coordinates, phase shift and voltage amplitude of a four-electrode, dual entry model on a virtual 1.7 cm diameter tumour. The insertion and optimized tip coordinates, and planning CT were input to the neurosurgical robot (Neuromate[®]) planning system (NeuroinspireTM)⁶⁴ for registration to the robot coordinate system using the NeurolocateTM fiducial apparatus and frameless patient registration module. A 2.11 mm diameter cannula fixed to the robot arm with an adaptor was used to place each electrode. The phantom was secured to the robot table using a cranial stabilization frame (Mayfield[®]). Post-implantation CT imaging was performed on the phantom and analyzed for geometrical accuracy and post-operative treatment planning.

Electric field is established by applying voltages and their phase shifts across electrodes. For each electrode, phase shift and voltage programming was applied as per phase shift optimization and voltage scaling results for the phantom CT model, to deliver the 1 V/cm electric field treatment to the tumour. The voltage drop and simulated electric field distribution was validated by measuring the voltage at two measurement electrodes, and various contacts on the stimulating electrodes. A four-channel waveform generator (Highland Technology T340 4-channel compact function generator) was programmed based on optimized voltage and phase shift parameters and connected to five contacts per

stimulating electrode using custom BNC to five measurement probe cables. The voltage waveform at the measurement electrode locations was measured using a four-channel oscilloscope (Siglent SDS1104X-E). Uncertainties in voltage measurement values from the waveform generator and oscilloscope were added in quadrature as ± 40 Hz for frequency and ± 0.03 V for recording electrodes and ± 0.05 V for measurement contacts on the active electrodes. Uncertainties in the computer simulations were comprised of uncertainty in electrical properties (phantom conductivity $\pm 1.0 \times 10^{-7}$ S/m, phantom dielectric ± 1.0 , electrode insulation $\pm 1.0 \times 10^{-4}$ S/m) and trajectory (± 1.10 mm). A parameter sweep for all uncertainty parameters and the effects on voltage and electric field tumour coverage was performed for each measurement scenario to obtain electrode contact specific simulation uncertainties.

3.3 Results

3.3.1 Slicelet Design

The completed custom IMT Slicelet (Appendix D: Figure D.1) contains all necessary planning steps within the workflow illustrated by Figure 3.1. All components and modules of the custom IMT Slicelet were tested for functionality. No user interaction with external software was required and the entire user experience of IMT treatment planning was contained within the Slicelet. Live connection between 3D Slicer and the MATLAB-COMSOL Livelink during optimization was successfully observed.

3.3.2 Smoothing and Electrode Implantation Modules

The smoothing module was demonstrated on segmented volumes from the human, and phantom MRI datasets. Brain and tumour volumes were smoothed and simplified to < 100 kB and were successfully implemented in the patient-specific COMSOL model build. A combination of the filters included in the module were required to reduce the file size while maintaining accuracy of the segmentations. The electrode implantation module was also tested on the human and phantom MRI datasets. For the human case, six electrodes were placed on the MRI from two burr holes (three electrodes per entry point) by selecting the insertion and tip coordinates of each electrode. For the phantom scenario,

four electrodes were placed from either a single insertion site or two different insertion sites.

3.3.3 Optimization Module

The five main optimization types (electrode phase shift, electrode location + phase shift, individual contact phase shift, individual contact voltage amplitude, and individual contact phase shift + voltage amplitude) were tested for functionality on the human and phantom models. Optimal parameters that provide the necessary tumour coverage by the prescribed electric field were determined by the optimization algorithm. Any electrode contacts that did not contribute to the tumour coverage, were automatically turned off to minimize the number of active contacts. The different electrode models (human multi-contact cylindrical electrodes, human custom electrode array and preclinical electrode constructs) were operational within the COMSOL model build and MATLAB optimization algorithm. The scale voltage option increased the voltage applied to each electrode until the desired tumour coverage was achieved. The location change option successfully updated the electric field map display considering the change in electrode coordinates.

3.3.4 Planning System Testing

The full planning pipeline was tested on both human and phantom models. Upon completion of an optimization, the resulting stimulation parameter tables, electrode coordinates table, electric field maps, 3D geometry, and EVH were displayed (Appendix D: Figure D.2, D.3, D.4). The results of a patient plan were accessible for future viewing by loading the visualization from the patient file. Full pipeline implementation using our planning system was achievable for the tested pre-operative dual-entry human (Figure 3.2(a,b)), single-entry human (Figure 3.2(c,d)) and phantom models. The optimized results of the human dual-entry six electrode plan were electrodes spaced throughout the tumour volume (Figure 3.2(a)), covering 95.9% of the tumour volume with 1 V/cm, with a conformity index of 0.69. One electrode only required one active contact, one required three active contacts, one required four active contacts, and three required five active contacts. The voltage amplitude applied to active contacts ranged from 1.48 V to 4.00 V,

resulting in electric fields that were conformal to the tumour volume (Figure 3.2(b)). The optimized six electrode single entry human model contained electrodes evenly distributed through the tumour (Figure 3.2(c)), covering 95.6% of the tumour with 1 V/cm, with a conformity index of 0.69. Four electrodes required four active contacts, one required five and one required six, with applied voltage amplitudes ranged from 0.63 V to 4.00 V, to shape the electric field to cover the tumour (Figure 3.2(d)).

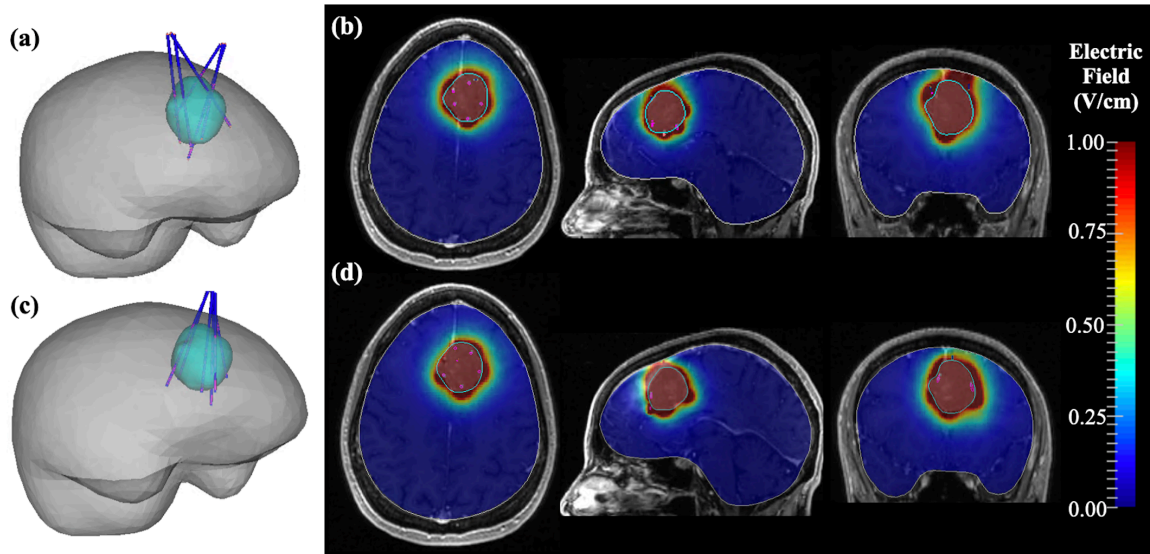


Figure 3.2: Results of electric field optimization for the (a) dual entry six-electrode human model with electrode location results displayed as the 3D geometry of brain (grey), tumour (cyan), electrodes (blue) and active contacts (magenta). The resulting electric fields (b) are displayed on selected axial, sagittal, and coronal cross sections superimposed on the MRI. Further numerical results of optimal phase shift, voltage amplitude, and electrode trajectories can be found in Appendix D (Figure D.2). Results of electric field optimization for the (c) six-electrode single entry human model with 3D geometry and (d) resulting electric fields displayed on selected axial, sagittal and coronal cross sections superimposed on the MRI. Further numerical results of optimal phase shift, voltage amplitude, and electrode trajectories can be found in Appendix D (Figure D.3).

All plans were set to cover 95.0% of the tumour volume with 1 V/cm, which was achieved in all cases. Conformity index optimization preserved this tumour coverage

while decreasing the electric field outside of the tumour and minimizing the number of active contacts. To optimize all parameters (electrode tip coordinates, individual contact phase shift, and voltage amplitude), the most efficient approach was to begin with the electrode location + phase shift optimization, followed by voltage scaling. The plan is further refined to determine optimal phase shift of the individual contacts on each electrode, and conformity index optimization of phase shift and voltage per electrode contact. Optimization results for all tested plans determined that electric fields could be shaped in 3D to cover the tumour volume over time.

3.3.5 Phantom Electrode Implantation

Pre-operative CT imaging was performed on the brain phantom and imported into the IMT treatment planning system, where a 1.7 cm diameter tumour was simulated. The optimization of electrode locations and phase shift of 2.20 V waveforms resulted in relative phase shifts of each electrode as 0° , 71.9° , 170.6° , and 235.3° to cover 96.1% of the tumour volume with 1 V/cm (Figure 3.3).

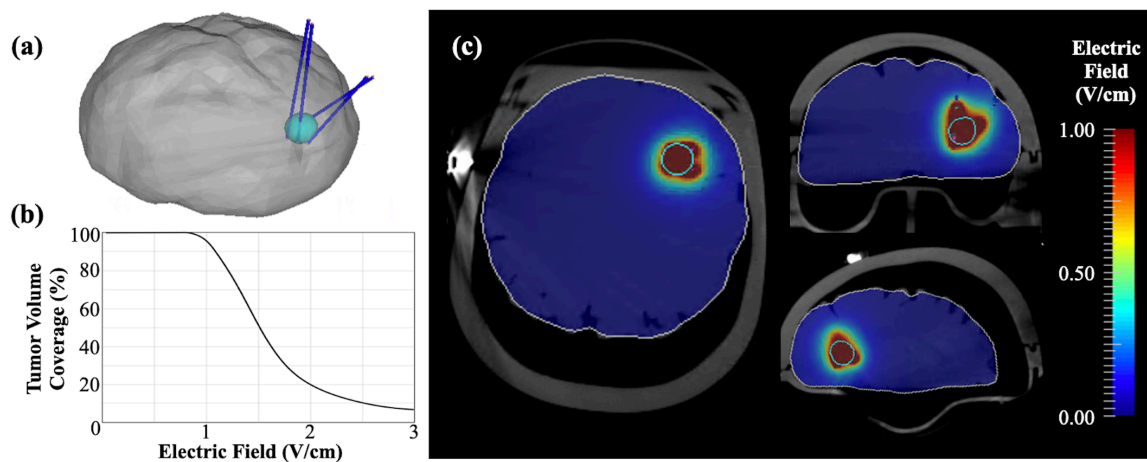


Figure 3.3: Results of electric field optimization for the four-electrode dual entry CT phantom model. Electrode location results displayed as (a) 3D geometry of brain phantom model. Electrode location results displayed as (a) 3D geometry of brain phantom model. Electrode location results displayed as (a) 3D geometry of brain phantom model. Electrode location results displayed as (a) 3D geometry of brain phantom model. Electrode location results displayed as (a) 3D geometry of brain phantom model. Numerical electric field coverage results are displayed as the (b) EVH of tumour coverage, and (c) resulting electric fields are displayed on selected axial, coronal and sagittal cross sections superimposed on the phantom MRI. Further numerical results of optimal

phase shift, voltage amplitude, and electrode trajectories can be found in Appendix D (Figure D.4).

The phantom brain and skull were attached to the robot (Figure 3.4(a)) with the stabilization frame and the fiducial apparatus attached to the robot arm (Figure 3.4(b)). The phantom pre-operative planning CT and planned electrode coordinates were registered to the robot operative setup CT with the planning system and frameless patient registration module. The four electrodes were placed through the cannula (Figure 3.4(c)) according to the optimization results, and the two recording electrodes were also implanted. CT imaging was acquired with a Medtronic O-Arm post-implantation (Figure 3.4(d)) and electrodes were successfully viewed in the resulting image (Figure 3.4(e)).

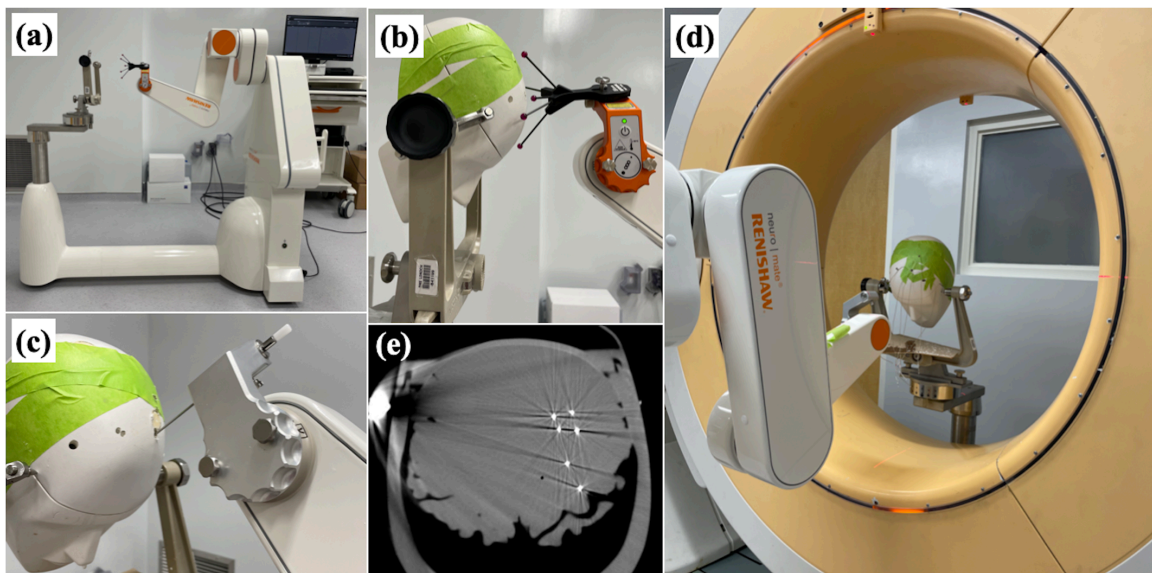


Figure 3.4: Robotic electrode implantation setup including (a) the Neuromate[®] robot with Mayfield[®] head frame and Neurolocate[™] fiducial apparatus attached, and the workstation running the Neuroinspire[™] electrode implantation planning system. (b) Phantom skull housing the brain phantom attached to the head frame with robot moved into Neurolocate[™] registration position. (c) Cannula placement through drilled hole in skull at registered implant trajectory and depth. (d) CT imaging setup of post-implantation of electrodes and (e) the resulting CT image of

the six implanted electrodes in the axial plane showing the four stimulating electrodes (top) and the two measurement electrodes (bottom).

The planned voltage waveforms were applied to the four electrodes, with five active contacts on each electrode (Figure 3.5(a)), and the voltage over time was measured at the two recording electrodes. Measurements were also obtained from disconnected middle contacts on each active electrode (Figure 3.5(b,c)). The frequency of all recorded continuous sinusoidal waveforms was $200 \text{ kHz} \pm 40 \text{ Hz}$. The post-operative CT was used to simulate the actual implant geometry (Figure 3.5(b)), with a calculated average Euclidian trajectory offset of 1.10 mm compared to the planned geometry. Simulation results of the voltage at measurement electrode contacts yielded electrical conductivity and dielectric of the phantom as 6.0 e-7 S/m and 5.0 respectively, and a conductivity of 5.0 e-4 S/m for the electrodes insulated section between electrode contacts.

Comparison between the measured voltage amplitudes and simulated voltages with maximum measurement and average simulation uncertainties are plotted in Figure 3.5(c). Voltage amplitudes were recorded at the distal contacts on measurement electrodes for the planned 20 contact stimulation, and additional measurements were obtained for 19 contact stimulation and 16 contact stimulation, with corresponding active contacts (colour highlighted contacts in Figure 3.5(b)) replaced with measurement probes (Figure 3.5(c)). Uncertainties in electrical properties and trajectories resulted in voltage simulation average uncertainties ranging from $\pm 0.01 \text{ V}$ to $\pm 0.06 \text{ V}$. The uncertainty of electrical properties did not impact the tumour coverage within $p < 0.01$. The average 1.10 mm trajectory uncertainty of each electrode impacted the electric field tumour coverage by a maximum of 2.6%. The simultaneous measurement of voltage waveforms from the center contacts on the four stimulating electrodes allowed for validation of delivered phase shift between contacts within 5.8° average uncertainty, resulting in a maximum impact of 0.4% and average impact of 0.03% on electric field tumour coverage.

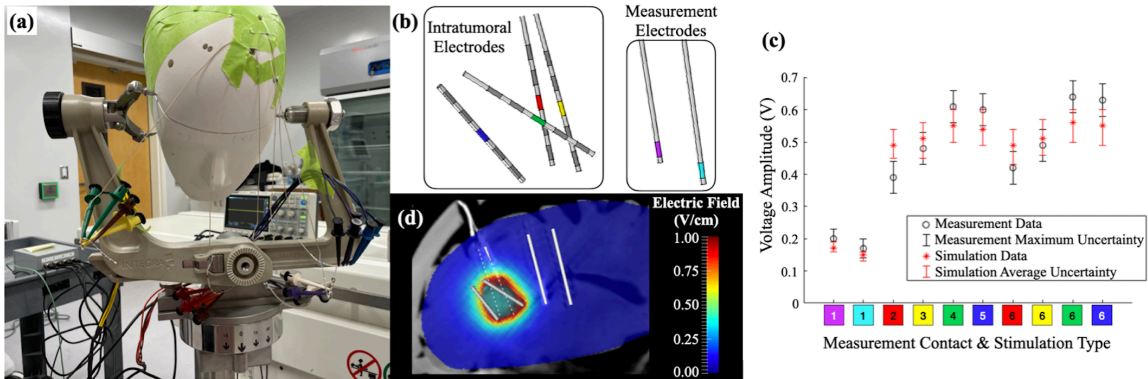


Figure 3.5: (a) Post-implantation phantom with four electrodes stimulated with four-channel waveform generator, connected to five contacts per electrode (20 total stimulating contacts), and two additional measurement electrodes. (b) Simulated geometry of electrode construct with measurement contacts highlighted in different colours. (c) Voltage measurement and simulation results, with colours corresponding to measurement contacts on electrode geometry, for various stimulation types (1: Full 20 contact stimulation, 2-5: 19 contact stimulation with corresponding electrode contact replaced with measurement prong, and 6: 16 contact stimulation with all middle contacts replaced with measurement prongs). (d) Sagittal slice of post-operative treatment planning results with electric field superimposed on the CT and implanted electrodes projections (white) and tumour (cyan).

A post-operative plan using actual implant coordinates from the post-operative CT (Figure 3.4(e)) was performed to validate post-operative planning capability of the treatment planning system (Figure 3.5(d)). Post-operative planning found optimal parameters at actual implant locations as 2.20 V with phase shifts of 0° , 39.6° , 142.0° , 220.9° resulting in 95.4% tumour coverage with four active contacts on two electrodes, and five active contacts on the remaining two electrodes.

3.4 Discussion

In this study a custom IMT planning system was developed to map electric field distributions for human and preclinical models. 3D Slicer provided a suitable platform to create a custom coded Slicelet for our customized planning modules. External software

modules were integrated into the system as background processes, removing user interaction with MeshLab, COMSOL, or MATLAB. The treatment planning pipeline was semi-automated, with fully automated COMSOL patient-specific model builds and MATLAB optimization code. Time-saving processes were also implemented into the MATLAB optimization, including the superposition of electric fields for objective calculation, custom mesh and interpolation matrix sizes, and rounding of parameters to 0.1 mm for location, 0.01 radians for phase shift, and 0.01 V for voltage amplitude. These updates resulted in an 8.3x speed improvement for location-based optimizations, and a 208x speed improvement for phase shift and voltage amplitude optimizations.

Different electrode types were utilized in the system including multi-contact human scale cylindrical electrodes defined by insertion and tip coordinates, and options for custom electrode arrays, and preclinical multi-electrode wire constructs. Electric field treatment parameters, including electrode locations, phase shifts and voltage amplitude were planned within the optimization module to maximize electric field coverage to the tumour over time. Conformity index optimization allowed for electric fields to be shaped in 3D to cover the tumour volume, while minimizing the field outside of the tumour. The optimized electric fields are visualized on interactive MRI slices, and the optimal geometry is visualized as a 3D model of the brain, tumour, and electrodes. The numerical results are displayed as parameter tables and the EVH graph to analyze the tumour volume and organ at risk coverage.

IMT is still in the early stages of development, and in order to move toward clinical trials, a treatment planning system is needed to determine the number of electrodes and their programming to accommodate tumours of different shape and size, located in any area of the brain. Different tumour types can also be considered, with electrical properties customizable for patient-specific brain and tumour characteristics. With initial electrode locations planned in the electrode implantation module, the treatment provider can ensure the electrode trajectories avoid any sensitive structures. Post-operative planning provides two essential capabilities, namely the adjustment of parameters after electrode insertion, to account for the actual implantation coordinates, and the adjustment of treatment parameters over time as the tumour volume changes shape and size throughout treatment.

Electrode encapsulation layer, brain shift, edema, and scarring over time can also be accounted for with post-operative stimulation re-optimization. The low voltage nature of IMT (akin to DBS which is regulated to ensure minimal tissue heating⁶⁵) and active electrode contact placement within tumour tissue, presents minimal risk to nearby normal tissues. The maximum surface charge density in our study was $0.08 \mu\text{C}/\text{cm}^2$ which is well below the limit of $30 \mu\text{C}/\text{cm}^2$, ensuring electric fields are safely deliverable⁶⁶. Organs at risk, such as the brainstem, were still considered in the IMT planning system, as electrode trajectories should not pass through these volumes. The optimization of electric field coverage considering the avoidance of sensitive structures and organs at risk was presented in previous work⁷.

The treatment planning system was validated by planning and robotically implanting four stimulating electrodes and two measurement electrodes in a brain phantom. The pre-operative electrode configuration was implanted into the brain phantom and planned waveforms were applied to five contacts per electrode. Voltage measurements at the active contacts and recording electrodes demonstrated the capability to validate the voltage drop and electrical properties of the model post-implantation. When stimulation to middle contacts were replaced with measurement probes (Figure 3.5), measured voltages showed larger offsets from simulations compared to separate measurement probes placed ~ 1 cm from the closest active electrode, likely due to capacitive cross talk between recording and active wires within the same electrode. The accuracy of tip coordinate separation between electrode pairs was observed as 1.10 ± 0.60 mm.

Post-operative planning was validated using the actual implant coordinates localized with post-implant CT imaging. Measurements of the voltage surrounding the treated brain phantom found all but one voltage measurement was equal to simulations within the uncertainty. The bending of the electrodes is attributed to this offset between predicted and actual voltages. While the uncertainty in the simulation electrical property parameters affects the predicted voltage measurement, the overall electric field tumour coverage remains unaffected by these uncertainties. Trajectory uncertainties showed impact on both the voltage and electric field tumour coverage. The validation of delivered phase

shift to within 1.6% provides insight on future treatment planning system updates to phase shift specificity.

Surgical electrode implantation of IMT electrodes will need to consider surgical and hardware complications associated with DBS and SEEG electrode implantation. Such risks remain low, but include hemorrhage, infection, stroke, implant misplacement and migration, and component failure^{67,68}. The success and tolerability of DBS long-term implantation supports the potential of IMT to improve patient quality of life compared to external electric field devices, other ablation techniques, radiation, and chemotherapy. Limitations of the current planning pipeline include no differentiation between necrotic core and enhancing tumour segmentation, and long computation times (~4-8 hours depending on the number of electrodes) required for location-based optimizations. The incorporation of necrotic core, white matter, grey matter, and cerebrospinal fluid (CSF) can be achieved in the future by additional segmentations and electrical parameter specification and could be implemented based on semi-automatic methods using specific MRI pulse sequences⁶⁹⁻⁷¹, and patient-specific electrical conductivity and permittivity maps⁷². Theoretically, since the active electrode contacts are within or directly adjacent the local tumour volume, the surrounding brain tissue inhomogeneities (white matter, grey matter, CSF) should not impact the results of the optimization, as has been supported by external field delivery studies^{5,73}. The long computation times associated with location-based optimizations can be addressed in the future by utilizing parallel computing. Other future work will involve addressing the accuracy of the electric fields considering uncertainties from imaging, electrode localization, and finite element discretization and investigating custom electrode arrays for surgical resection cavities. Insights on the mechanisms of action will shape future updates to the planning system, including the importance and inclusion of electric field anisotropy optimization. Concurrent *in vitro* and *in vivo* validations will lay a framework for a future single center safety trial.

The pipeline steps for planning an IMT treatment have been integrated into a single platform that consists of tissue segmentation, volume smoothing and simplification, electrode trajectory planning, electric field optimization, and results visualization. The

amalgamation of planning steps in our custom semi-automated treatment planning system has improved the time to generate a treatment plan and the accessibility to the novice user. With the results of this study, the IMT optimization algorithm has been expanded to incorporate patient-specific scenarios, establishing a platform for future use in early-stage clinical investigations.

3.5 Conclusions

The custom IMT treatment planning system and underlying optimization methods developed in this study provide an essential platform for future early clinical studies. The system provides a variety of planning options including pre-operative and post-operative, surgical resection cavity models, and preclinical models, in addition to considerations of nearby organs at risk, tissue electrical properties, and prescription electric fields. The versatility of the system to patient-specific tumour shape and size, location, and tumour type will be evaluated in a future user study on large scale patient dataset planning. Overall, we have semi-automated and coalesced all IMT planning pipeline steps into a single user interface and validated the pipeline on a phantom model. This novel IMT treatment planning system will allow for future developments of IMT, progressing this technology towards clinical trials.

3.6 Acknowledgements

This work is supported in part by NSERC CGS-D (E.I), NSERC Idea to Innovation Grant (E.W.), NSERC Discovery Grant (E.W.), Cancer Research Society (M.O.H.), the Canada Foundation for Innovation (CFI) (T.P.) and the Western Innovation Fund (M.O.H.). SEEG electrodes and cannulas donated by Surgi-One Medical Technologies Inc.

3.7 Conflicts of Interest

M.O.H. and S.S. are inventors on the following patent that is assigned to “London Health Sciences Centre Research Inc.” (the applicant): CA2985847 entitled “Intratumoral Modulation Therapy”. E.W., M.O.H., T.P., and S.S. are inventors on the following patent application that is assigned to “London Health Sciences Centre Research Inc.” (the

applicant): WO2021142549 entitled “Planning and delivery of dynamically oriented electric field for biomedical applications”. The authors have no other competing interests.

3.8 References

1. Stupp R, Wong ET, Kanner AA, et al. NovoTTF-100A versus physician’s choice chemotherapy in recurrent glioblastoma: A randomised phase III trial of a novel treatment modality. *Eur J Cancer*. 2012;48(14):2192-2202. doi:10.1016/j.ejca.2012.04.011
2. Stupp R, Taillibert S, Kanner A, et al. Effect of Tumor-Treating Fields Plus Maintenance Temozolomide vs Maintenance Temozolomide Alone on Survival in Patients With Glioblastoma. *JAMA*. 2017;318(23):2306. doi:10.1001/jama.2017.18718
3. Hottinger AF, Pacheco P, Stupp R. Tumor treating fields: a novel treatment modality and its use in brain tumors. *Neuro Oncol*. 2016;18(10):1338-1349. doi:10.1093/neuonc/now182
4. Swanson KD, Lok E, Wong ET. An Overview of Alternating Electric Fields Therapy (NovoTTF Therapy) for the Treatment of Malignant Glioma. *Curr Neurol Neurosci Rep*. 2016;16(1):8. doi:10.1007/s11910-015-0606-5
5. Wenger C, Miranda PC, Salvador R, et al. A Review on Tumor-Treating Fields (TTFields): Clinical Implications Inferred From Computational Modeling. *IEEE Rev Biomed Eng*. 2018;11:195-207. doi:10.1109/RBME.2017.2765282
6. Shah PP, White T, Khalafallah AM, Romo CG, Price C, Mukherjee D. A systematic review of tumor treating fields therapy for high-grade gliomas. *J Neurooncol*. 2020;148(3):433-443. doi:10.1007/s11060-020-03563-z
7. Iredale E, Deweyert A, Hoover DA, et al. Optimization of multi-electrode implant configurations and programming for the delivery of non-ablative electric fields in intratumoral modulation therapy. *Med Phys*. 2020;47(11):5441-5454. doi:10.1002/mp.14496
8. Deweyert A, Iredale E, Xu H, Wong E, Schmid S, Hebb MO. Diffuse intrinsic pontine glioma cells are vulnerable to low intensity electric fields delivered by intratumoral modulation therapy. *J Neurooncol*. 2019;143(1):49-56. doi:10.1007/s11060-019-03145-8
9. Di Sebastiano AR, Deweyert A, Benoit S, et al. Preclinical outcomes of Intratumoral Modulation Therapy for glioblastoma. *Sci Rep*. 2018;8(1):7301. doi:10.1038/s41598-018-25639-7
10. Xu H, Bihari F, Whitehead S, Wong E, Schmid S, Hebb MO. In Vitro Validation of Intratumoral Modulation Therapy for Glioblastoma. *Anticancer Res*. 2016;36:71-80.

11. Rominiyi O, Vanderlinden A, Clenton SJ, Bridgewater C, Al-Tamimi Y, Collis SJ. Tumour treating fields therapy for glioblastoma: current advances and future directions. *Br J Cancer*. 2021;124(4):697-709. doi:10.1038/s41416-020-01136-5
12. Tuszyński J, Wenger C, Friesen D, Preto J. An Overview of Sub-Cellular Mechanisms Involved in the Action of TTFields. *Int J Environ Res Public Health*. 2016;13(11):1128. doi:10.3390/ijerph13111128
13. Carrieri FA, Smack C, Siddiqui I, Kleinberg LR, Tran PT. Tumor Treating Fields: At the Crossroads Between Physics and Biology for Cancer Treatment. *Front Oncol*. 2020;10. doi:10.3389/fonc.2020.575992
14. Li X, Yang F, Rubinsky B. A Correlation Between Electric Fields That Target the Cell Membrane Potential and Dividing HeLa Cancer Cell Growth Inhibition. *IEEE Trans Biomed Eng*. 2021;68(6):1951-1956. doi:10.1109/TBME.2020.3042650
15. Li X, Yang F, Rubinsky B. A Theoretical Study on the Biophysical Mechanisms by Which Tumor Treating Fields Affect Tumor Cells During Mitosis. *IEEE Trans Biomed Eng*. 2020;67(9):2594-2602. doi:10.1109/TBME.2020.2965883
16. Kirson ED, Gurchich Z, Schneiderman R, et al. Disruption of Cancer Cell Replication by Alternating Electric Fields. *Cancer Res*. 2004;64(9):3288-3295. doi:10.1158/0008-5472.CAN-04-0083
17. Kirson ED, Dbalý V, Tovaryš F, et al. Alternating electric fields arrest cell proliferation in animal tumor models and human brain tumors. *Proc Natl Acad Sci*. 2007;104(24):10152-10157. doi:10.1073/pnas.0702916104
18. Giladi M, Schneiderman RS, Voloshin T, et al. Mitotic Spindle Disruption by Alternating Electric Fields Leads to Improper Chromosome Segregation and Mitotic Catastrophe in Cancer Cells. *Sci Rep*. 2016;5(1):18046. doi:10.1038/srep18046
19. Chang E, Patel CB, Pohling C, et al. Tumor treating fields increases membrane permeability in glioblastoma cells. *Cell Death Discov*. 2018;4(1):113. doi:10.1038/s41420-018-0130-x
20. Connelly J, Hormigo A, Mohilie N, Hu J, Chaudhry A, Blondin N. Planning TTFields treatment using the NovoTAL system-clinical case series beyond the use of MRI contrast enhancement. *BMC Cancer*. 2016;16(1):842. doi:10.1186/s12885-016-2890-0
21. Chaudhry A, Benson L, Varshaver M, et al. NovoTTFTM-100A System (Tumor Treating Fields) transducer array layout planning for glioblastoma: a NovoTALTM system user study. *World J Surg Oncol*. 2015;13(1):316. doi:10.1186/s12957-015-0722-3
22. Benson L. Tumor Treating Fields Technology: Alternating Electric Field Therapy for the Treatment of Solid Tumors. *Semin Oncol Nurs*. 2018;34(2):137-150. doi:10.1016/j.soncn.2018.03.005
23. Wenger C, Salvador R, Bassar PJ, Miranda PC. Improving Tumor Treating Fields Treatment Efficacy in Patients With Glioblastoma Using Personalized Array

- Layouts. *Int J Radiat Oncol.* 2016;94(5):1137-1143. doi:10.1016/j.ijrobp.2015.11.042
24. Korshoej AR, Sørensen JCH, von Oettingen G, Poulsen FR, Thielscher A. Optimization of tumor treating fields using singular value decomposition and minimization of field anisotropy. *Phys Med Biol.* 2019;64(4):04NT03. doi:10.1088/1361-6560/aafe54
 25. Adair DSP, Gomes KS, Kiss ZHT, Gobbi DG, Starreveld YP. Tactics: an open-source platform for planning, simulating and validating stereotactic surgery. *Comput Assist Surg.* 2020;25(1):1-14. doi:10.1080/24699322.2020.1760354
 26. Bériault S, Subaie F Al, Collins DL, Sadikot AF, Pike GB. A multi-modal approach to computer-assisted deep brain stimulation trajectory planning. *Int J Comput Assist Radiol Surg.* 2012;7(5):687-704. doi:10.1007/s11548-012-0768-4
 27. Liu Y, Konrad PE, Neimat JS, et al. Multisurgeon, Multisite Validation of a Trajectory Planning Algorithm for Deep Brain Stimulation Procedures. *IEEE Trans Biomed Eng.* 2014;61(9):2479-2487. doi:10.1109/TBME.2014.2322776
 28. Essert C, Fernandez-Vidal S, Capobianco A, et al. Statistical study of parameters for deep brain stimulation automatic preoperative planning of electrodes trajectories. *Int J Comput Assist Radiol Surg.* 2015;10(12):1973-1983. doi:10.1007/s11548-015-1263-5
 29. Essert C, Haegelen C, Lalyis F, Abadie A, Jannin P. Automatic computation of electrode trajectories for Deep Brain Stimulation: a hybrid symbolic and numerical approach. *Int J Comput Assist Radiol Surg.* 2012;7(4):517-532. doi:10.1007/s11548-011-0651-8
 30. Krauss JK, Lipsman N, Aziz T, et al. Technology of deep brain stimulation: current status and future directions. *Nat Rev Neurol.* 2021;17(2):75-87. doi:10.1038/s41582-020-00426-z
 31. Garcia PA, Kos B, Rossmeis JH, Pavliha D, Miklavčič D, Davalos R V. Predictive therapeutic planning for irreversible electroporation treatment of spontaneous malignant glioma. *Med Phys.* 2017;44(9):4968-4980. doi:10.1002/mp.12401
 32. Stillström D, Sandu R-M, Freedman J. Accuracy of Electrode Placement in IRE Treatment with Navigated Guidance. *Cardiovasc Intervent Radiol.* 2021;44(6):968-975. doi:10.1007/s00270-020-02762-5
 33. Ding L, Moser M, Luo Y, Zhang W, Zhang B. Treatment Planning Optimization in Irreversible Electroporation for Complete Ablation of Various Sized Cervical Tumors: A Numerical Study. *J Biomech Eng.* 2021;143(1). doi:10.1115/1.4047551
 34. Edd JF, Davalos R V. Mathematical Modeling of Irreversible Electroporation for Treatment Planning. *Technol Cancer Res Treat.* 2007;6(4):275-286. doi:10.1177/153303460700600403
 35. Gong L, Yao C, Dong S, Zhao Y. The optimization of the treatment planning for achieving complete ablation of tumor during irreversible electroporation by genetic

- algorithm. In: *2017 IEEE 21st International Conference on Pulsed Power (PPC)*. Vol 2017-June. IEEE; 2017:1-6. doi:10.1109/PPC.2017.8291223
36. Vakharia VN, Sparks R, Misericchi A, et al. Computer-Assisted Planning for Stereoelectroencephalography (SEEG). *Neurotherapeutics*. 2019;16(4):1183-1197. doi:10.1007/s13311-019-00774-9
 37. Nowell M, Sparks R, Zombori G, et al. Comparison of computer-assisted planning and manual planning for depth electrode implantations in epilepsy. *J Neurosurg*. 2016;124(6):1820-1828. doi:10.3171/2015.6.JNS15487
 38. González-Martínez J, Bulacio J, Thompson S, et al. Technique, Results, and Complications Related to Robot-Assisted Stereoelectroencephalography. *Neurosurgery*. 2016;78(2):169-180. doi:10.1227/NEU.0000000000001034
 39. Narayanasamy G, Saenz DL, Defoor D, Papanikolaou N, Stathakis S. Dosimetric validation of Monaco treatment planning system on an Elekta VersaHD linear accelerator. *J Appl Clin Med Phys*. 2017;18(6):123-129. doi:10.1002/acm2.12188
 40. Peters S, Schiefer H, Plasswilm L. A treatment planning study comparing Elekta VMAT and fixed field IMRT using the varian treatment planning system eclipse. *Radiat Oncol*. 2014;9(1):153. doi:10.1186/1748-717X-9-153
 41. Ding C, Saw CB, Timmerman RD. Cyberknife stereotactic radiosurgery and radiation therapy treatment planning system. *Med Dosim*. 2018;43(2):129-140. doi:10.1016/j.meddos.2018.02.006
 42. Bodensteiner D. RayStation: External beam treatment planning system. *Med Dosim*. 2018;43(2):168-176. doi:10.1016/j.meddos.2018.02.013
 43. Mzenda B, Mugabe K V., Sims R, Godwin G, Loria D. Modeling and dosimetric performance evaluation of the RayStation treatment planning system. *J Appl Clin Med Phys*. 2014;15(5):29-46. doi:10.1120/jacmp.v15i5.4787
 44. Xia P, Murray E. 3D treatment planning system—Pinnacle system. *Med Dosim*. 2018;43(2):118-128. doi:10.1016/j.meddos.2018.02.004
 45. Jameson MG, Ohanessian L, Batumalai V, Patel V, Holloway LC. Comparison of Oncentra[®] Brachy IPSA and graphical optimisation techniques: a case study of HDR brachytherapy head and neck and prostate plans. *J Med Radiat Sci*. 2015;62(2):168-174. doi:10.1002/jmrs.107
 46. Shwetha B, Ravikumar M, Supe SS, Sathiyam S, Lokesh V, Keshava SL. Dosimetric evaluation of two treatment planning systems for high dose rate brachytherapy applications. *Med Dosim*. 2012;37(1):71-75. doi:10.1016/j.meddos.2010.12.015
 47. 3D Slicer. 3D Slicer image computing platform. <https://www.slicer.org>.
 48. Fedorov A, Beichel R, Kalpathy-Cramer J, et al. 3D Slicer as an image computing platform for the Quantitative Imaging Network. *Magn Reson Imaging*. 2012;30(9):1323-1341. doi:10.1016/j.mri.2012.05.001

49. Renishaw. neuromate® robotic system for stereotactic neurosurgery. <https://www.renishaw.com/en/neuromate-robotic-system-for-stereotactic-neurosurgery--10712>.
50. 3D Slicer. Slicelets. <https://www.slicer.org/wiki/Documentation/Nightly/Developers/Slicelets>.
51. 3D Slicer. Models Module. <https://www.slicer.org/wiki/Documentation/4.3/Modules/Volumes>.
52. 3D Slicer. Volumes Module. <https://www.slicer.org/wiki/Documentation/4.3/Modules/Volumes>.
53. Wenger C, Salvador R, Basser PJ, Miranda PC. The electric field distribution in the brain during TTFIELDS therapy and its dependence on tissue dielectric properties and anatomy: a computational study. *Phys Med Biol*. 2015;60(18):7339-7357. doi:10.1088/0031-9155/60/18/7339
54. Korshoej AR, Saturnino GB, Rasmussen LK, von Oettingen G, Sørensen JCH, Thielscher A. Enhancing Predicted Efficacy of Tumor Treating Fields Therapy of Glioblastoma Using Targeted Surgical Craniectomy: A Computer Modeling Study. Debinski W, ed. *PLoS One*. 2016;11(10):e0164051. doi:10.1371/journal.pone.0164051
55. Miranda PC, Mekonnen A, Salvador R, Basser PJ. Predicting the electric field distribution in the brain for the treatment of glioblastoma. *Phys Med Biol*. 2014;59(15):4137-4147. doi:10.1088/0031-9155/59/15/4137
56. Korshoej AR, Hansen FL, Thielscher A, von Oettingen GB, Sørensen JCH. Impact of tumor position, conductivity distribution and tissue homogeneity on the distribution of tumor treating fields in a human brain: A computer modeling study. Debinski W, ed. *PLoS One*. 2017;12(6):e0179214. doi:10.1371/journal.pone.0179214
57. Gabriel C, Peyman A, Grant EH. Electrical conductivity of tissue at frequencies below 1 MHz. *Phys Med Biol*. 2009;54(16):4863-4878. doi:10.1088/0031-9155/54/16/002
58. Latikka J, Kuurne T, Eskola H. Conductivity of living intracranial tissues. *Phys Med Biol*. 2001;46(6):1611-1616. doi:10.1088/0031-9155/46/6/302
59. Stoy RD, Foster KR, Schwan HP. Dielectric properties of mammalian tissues from 0.1 to 100 MHz; a summary of recent data. *Phys Med Biol*. 1982;27(4):501-513. doi:10.1088/0031-9155/27/4/002
60. Latikka J, Eskola H. The Resistivity of Human Brain Tumours In Vivo. *Ann Biomed Eng*. 2019;47(3):706-713. doi:10.1007/s10439-018-02189-7
61. 3D Slicer. Sample Data. <https://www.slicer.org/wiki/SampleData>.
62. Synaptive Medical. BrightMatter™ Simulate: Remarkably life-like brain tissue models. <https://www.synaptivemedical.com/products/simulate/>.

63. Butson CR, McIntyre CC. Role of electrode design on the volume of tissue activated during deep brain stimulation. *J Neural Eng.* 2006;3(1):1-8. doi:10.1088/1741-2560/3/1/001
64. Renishaw. neuroinspire™ neurosurgical planning software. <https://www.renishaw.com/en/neuroinspire-neurosurgical-planning-software--8244>.
65. Elwassif MM, Datta A, Rahman A, Bikson M. Temperature control at DBS electrodes using a heat sink: experimentally validated FEM model of DBS lead architecture. *J Neural Eng.* 2012;9(4):046009. doi:10.1088/1741-2560/9/4/046009
66. Cogan SF, Ludwig KA, Welle CG, Takmakov P. Tissue damage thresholds during therapeutic electrical stimulation. *J Neural Eng.* 2016;13(2):021001. doi:10.1088/1741-2560/13/2/021001
67. Fenoy AJ, Simpson RK. Risks of common complications in deep brain stimulation surgery: management and avoidance. *J Neurosurg.* 2014;120(1):132-139. doi:10.3171/2013.10.JNS131225
68. Mullin JP, Shriver M, Alomar S, et al. Is SEEG safe? A systematic review and meta-analysis of stereo-electroencephalography-related complications. *Epilepsia.* 2016;57(3):386-401. doi:10.1111/epi.13298
69. Singh MK, Singh KK. A Review of Publicly Available Automatic Brain Segmentation Methodologies, Machine Learning Models, Recent Advancements, and Their Comparison. *Ann Neurosci.* 2021;28(1-2):82-93. doi:10.1177/0972753121990175
70. Wang Y, Wang Y, Zhang Z, et al. Segmentation of gray matter, white matter, and CSF with fluid and white matter suppression using MP2RAGE. *J Magn Reson Imaging.* 2018;48(6):1540-1550. doi:10.1002/jmri.26014
71. Dora L, Agrawal S, Panda R, Abraham A. State-of-the-Art Methods for Brain Tissue Segmentation: A Review. *IEEE Rev Biomed Eng.* 2017;10:235-249. doi:10.1109/RBME.2017.2715350
72. Michel E, Hernandez D, Lee SY. Electrical conductivity and permittivity maps of brain tissues derived from water content based on T₁-weighted acquisition. *Magn Reson Med.* 2017;77(3):1094-1103. doi:10.1002/mrm.26193
73. Wenger C, Bomzon Z, Salvador R, Basser PJ, Miranda PC. Simplified realistic human head model for simulating Tumor Treating Fields (TTFields). In: *2016 38th Annual International Conference of the IEEE Engineering in Medicine and Biology Society (EMBC)*. Vol 2016-October. IEEE; 2016:5664-5667. doi:10.1109/EMBC.2016.7592012

Chapter 4

4 Spatiotemporally Dynamic Electric Fields for Brain Cancer Treatment: An In Vitro Investigation

This chapter was adapted from the published article entitled “Spatiotemporally dynamic electric fields for brain cancer treatment: an in vitro investigation” by Erin Iredale, Abdulla Elsaleh, Hu Xu, Paul Christiaans, Andrew Deweyert, John Ronald, Susanne Schmid, Matthew O. Hebb, Terry M. Peters, and Eugene Wong, Physics in Medicine and Biology, 68:085012 (2023). Permission to reproduce can be found in Appendix A.

4.1 Introduction

New treatments for glioblastoma (GBM) are imperative, as it remains the most common incurable primary brain cancer¹. The clinical treatment standard for GBM is currently surgical resection followed by concurrent chemotherapy (temozolomide) and radiotherapy¹, but survival outcomes remain poor. Advancements in the field of electrotherapy have given rise to the use of low intensity, non-ablative electric fields to control the growth of brain tumours²⁻¹⁰. Our group has shown that the delivery of tumour suppressing electric fields using implantable bioelectrodes, termed intratumoural modulation therapy (IMT), is efficacious in preclinical investigations⁸⁻¹⁰ using a single stimulating electrode. Electric fields of intermediate frequency (200 kHz) produced from low voltage (2 V) sources impede the growth of high grade gliomas, including GBM, while non-neoplastic neurons and brain tissue remains relatively unaffected^{8,9}. We and others have demonstrated computer simulations to be useful tools to analyze and plan electric field distributions in realistic preclinical and clinical scenarios¹¹⁻¹⁸. Electric field simulations of single electrode *in vitro* IMT models suggest that while the coverage is sufficient for preclinical models, improvements in the extent of such coverage would be required to advance to human scale tumours^{8,9,11,12}. This has been suggested through the use of multiple electrodes programmed with different relative phase shifts of the input voltage waveforms, which has been shown to theoretically increase tumour coverage and homogeneity^{11,12}.

Previous IMT computer simulation, optimization and treatment planning studies^{11,12} have highlighted the theoretical benefit of using spatiotemporally dynamic (rotating) electric fields to increase electric field coverage over time. The optimization of relative phase shifts of input waveforms results in electric fields that rotate during the waveform period. These fields are scalable to cover human-size tumours, using low voltage waveforms (2-4 V) that produce sufficient field magnitude (~ 1 V/cm) to suppress human GBM cell viability^{2,4,19,20}. We have shown that a previously established IMT optimization algorithm¹² and treatment planning system¹¹ are applicable to *in vitro*, *in vivo*, and human tumour scenarios with phase shift, voltage and electrode location optimization parameters. Rotating fields provide increased field coverage and homogeneity compared to non-rotating fields, partly explaining why rotating fields are more effective. In addition, the telophase dielectrophoresis mechanism of action suggests field direction could play a role, supported previously with analysis of cell survival vs. division axis with parallel orientation showing a significant decrease in cell viability²¹. In 2D, rotating electric fields would provide a full 360 degrees of field direction, impacting dividing cells equally, regardless of division axis. While rotating electric fields are theoretically beneficial, there has yet to be *in vitro* field measurements or investigation of the impacts on GBM cell survival. The validation of delivered electric field is imperative for accurate stimulation and requires measurement of the delivered voltage and programming adjustment for each experiment trial. In this study, the electrical conductivity of the *in vitro* media DMEM was measured and employed in our computer simulations used to map the electric field. It was also used to determine the required voltage programming. An *in vitro* IMT device was designed, developed, and used to deliver rotating electric fields to patient derived GBM cells. The effects of spatiotemporally dynamic electric fields of different (a) magnitudes, (b) rotation, (c) frequency, and (d) interference were evaluated with experiments designed using supporting computer simulations. Improved field delivery validation and simulation based reprogramming methods established in this study provide a framework for future preclinical and clinical investigations. The cell response to various field patterns gives insight to the optimization goals implemented in the planning system in the future.

4.2 Materials and Methods

4.2.1 In Vitro Electrical Conductivity Measurement

To ensure that the desired electric field is being delivered to the target, the reduction in voltage induced by the low impedance of the culturing medium must first be considered so that the input voltage can be adjusted to account for this loss. This voltage drop is measured *in vitro* to determine the electrical conductivity and ensure that the electric field simulations are accurate. The electric fields produced from IMT electrodes *in vitro* were simulated in COMSOL Multiphysics (v5.4) at 200 kHz, where experimental geometries were replicated to provide an accurate representation of the electric field distribution over time. We measured the conductivity of our culturing media in a 3.5 cm diameter *in vitro* dish with 2 mL of Dulbecco's Modified Eagle Medium (DMEM) at 37°C (Figure 4.1). A 0.25 mm diameter platinum wire electrode was placed 2.6 cm away from a grounded electrode.

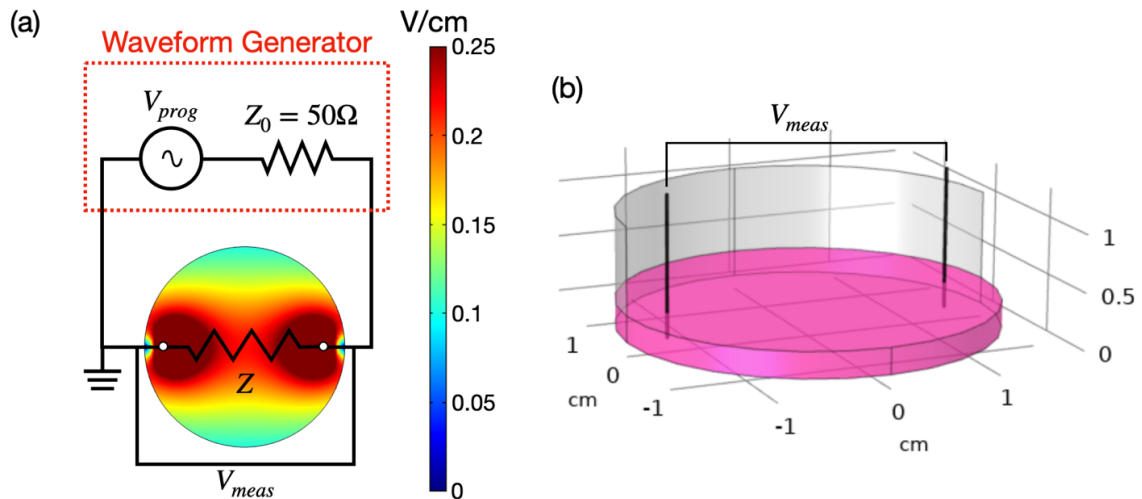


Figure 4.1: *In vitro* electrical conductivity measurement (a) circuit diagram with waveform generator programmed to V_{prog} and internal impedance Z_0 , connected to the *in vitro* setup with impedance Z , voltage across the dish of V_{meas} , and electric field map simulated from the (b) geometry of the *in vitro* setup.

We measured the impedance of the *in vitro* circuit by accounting for the internal resistance that is present in waveform generators. The relationship between the

programmed input voltage V_{prog} and the voltage delivered across the load V_{meas} is dependent on the internal resistance of the waveform generator (50Ω) and the impedance of the load Z .

$$V_{meas} = V_{prog} \frac{Z}{Z+50\Omega} \quad (4.1)$$

The low load impedance would result in an appreciably lower measured voltage compared to the programmed voltage, requiring an adjustment to the input voltage to make up for this voltage drop. We determined the impedance of the system using the programmed voltage V_{prog} and measurements of the delivered voltage V_{meas} .

A waveform generator (Highland Technology T340 four-channel compact function generator) programmed to a 2 V amplitude sine wave at 200 kHz frequency was applied to one electrode while the other was grounded. An oscilloscope (Siglent SDS1104X-E) was used to measure the voltage amplitude when the circuit is open (V_{prog}) and when the circuit is closed (V_{meas}) (Figure 4.1(a)), with each measurement repeated three times. The medium's electrical properties were determined by comparing the measured system impedance *in vitro* to the simulated impedance values for a range of DMEM electrical conductivities (0.1 S/m to 2 S/m), and a range of permittivity constants (1 to 1000) computed in COMSOL.

4.2.2 Electrode Construct Design Optimization

In vitro experiments to validate simulated electric field began with the choice of well size and the design of a custom four electrode IMT electrode construct. The electrode geometry containing four, 0.45 mm diameter platinum-iridium wire electrodes was created in COMSOL, along with 1 mL of DMEM with electrical conductivity determined from the *in vitro* measurement, and a dielectric constant of $80^{22,23}$. In COMSOL, electrical insulation was applied on all outer boundaries and stimulating voltage controlled sinusoidal waveform ($V = A \sin(2\pi ft - \phi)$) terminal boundaries on the wire electrode surfaces were applied with experiment and electrode specific voltage amplitude A , phase shift ϕ , and frequency f . A tetrahedral mesh was created for the geometry for computing the electric field. Electrode separation and programming (voltage and phase

shift) was determined using the custom IMT optimization algorithm^{11,12} to cover the central 6 mm diameter with a homogeneous 1 V/cm time averaged electric field. The electrode separations were then used to produce the electrode construct in a 24-well plate, a well sizing that most closely represents the maximum coverable tumour diameter of 2.1 cm using four electrodes at 2 V found previously¹².

4.2.3 Experiment Design Optimization

The *in vitro* experiments were designed using electric field simulations. The IMT optimization algorithm^{11,12} was utilized to optimize electrode voltage and phase shift programming with respect to electric field target coverage and homogeneity, and to compare different field amplitudes and programming scenarios. The voltage drop was considered in all cases, where the simulated impedance and desired voltage was used in Equation 4.1 to determine the programmed input voltage necessary to produce the desired electric field.

The first experiment (a) investigated the electric field dose-response curve of rotating fields at 200 kHz. All models used the fixed phase shift configuration (0, $\pi/2$, π , and $3\pi/2$ radians) previously found optimal¹², with delivered voltage amplitudes selected for 1 V/cm, 1.5 V/cm, and 2 V/cm dish coverage. Cell survival results S were then fitted to an adapted linear quadratic (LQ) model $S = A(e^{-(\alpha E + \beta E^2)} - 1) + 1$, where E is the electric field intensity, and fit parameters of A , α and β .

The next set of experiments compared (b) rotating vs. non-rotating fields at 1 V/cm, (c) 200 kHz vs. 10 kHz rotating fields at 1 V/cm, and (d) constructive vs. destructive interference. The rotating experimental arms used the phase shifted configuration (0, $\pi/2$, π , and $3\pi/2$ radians)¹², with voltage amplitudes selected to cover the dish with a field of 1 V/cm at either 200 kHz (ideal frequency for GBM²⁴) or 10 kHz (maximum available frequency for existing implantable stimulation devices²⁵). The non-rotating arm contained a pair of ground and a pair of in phase stimulating electrodes with voltage selected to deliver 1 V/cm at 200 kHz, where the pattern of adjacent ground and stimulating electrodes was previously found to produce constructive interference when no phase shifting was used¹². A final configuration investigated the importance of field

optimization and homogeneity, by using a destructive interference configuration (producing a field of 0 V/cm at the center of the region of interest) with alternating ground and stimulating electrodes at i) the same input voltage and ii) the same total system power as the rotating constructive interference scenario.

4.2.4 In Vitro IMT Model

GBM cells employed in this study were derived from patient tumours^{9,10}, and had been transfected with the firefly luciferase gene to enable bioluminescence imaging (BLI) for cell viability evaluation. Two cell lines (labelled GBM23 and GBM25) were used in this study. Cells were cultured in DMEM with 10% fetal bovine serum at 37°C, 5% CO₂, passaged at 80% confluence by splitting 1:2 using 0.25% trypsin with 0.91 mM ethylenediaminetetraacetic acid (EDTA). Culture media was changed twice weekly. GBM cells (3×10^4) were plated with 1 mL of DMEM in four wells of a 24-well plate and fitted with the custom-designed four electrode IMT delivery device. The stimulation was delivered using a four-channel waveform generator (Highland Technology T340) and a four-channel oscilloscope (Siglent SDS1104X-E) was used to validate the voltages and phase shifts delivered by each electrode. Experimental wells received continuous three-day stimulation (72 hours) with experiment specific voltage and phase shift IMT waveforms applied to each electrode. Sham wells contained the electrode hardware but received no stimulation.

Cell viability was analyzed after the treatment period using BLI where 8 μ L of 150 μ g/mL D-luciferin (PerkinElmer) was added to the culture media, the emission intensity captured (IVIS Lumina XRMS, PerkinElmer) and the mean photon flux measured (Living Image, Xenogen). Measurement data are presented as mean \pm standard deviation. Biological data sets were analyzed in MATLAB (v2022a) for normality²⁶, and compared using a 2-sample, 2-tailed *t* test, with results presented as mean \pm standard error and significance assumed at $p < 0.05$.

4.3 Results

4.3.1 In Vitro Electrical Conductivity Measurement

Measurement of the delivered voltage *in vitro* resulted in a mean (\pm standard deviation) difference $V_{prog} - V_{meas}$ of 0.14 ± 0.01 V, with voltage ratio V_{prog}/V_{meas} of 1.08 ± 0.01 , corresponding to an impedance of $625 \pm 34 \Omega$. In this model, for the range of frequencies 10-200 kHz, the impact of permittivity variations are negligible and the impedance and resistance are equivalent ($Z \approx R$), since the inverse resistance (0.0088 S) term dominates the capacitance (4.2416×10^{-12} F) term $2\pi fC$ (5×10^{-6} F/s) in the parallel RC impedance formula. With the electrical conductivity σ inversely proportional to resistance, and in our case, the impedance Z , conductivity can be expressed as $\sigma = CZ^{-1}$. The proportionality constant C is geometry dependent and was computed in COMSOL as 933.7 m^{-1} for this specific geometrical configuration (two electrodes placed 2.6 cm apart in a 3.5 cm diameter *in vitro* dish with 2 mL DMEM at 37°C). Using this relation and the measured impedance of $625 \pm 34 \Omega$, the conductivity of DMEM is determined to be 1.5 ± 0.1 S/m, which was then used in future *in vitro* simulations.

4.3.2 Electrode Construct Design Optimization

The optimal electrode configuration was four equally spaced electrodes, each placed 6.3 mm from the center of a 1.56 cm diameter well (24-well plate). This configuration covers the well with a homogeneous 1 V/cm electric field when electrodes are programmed to deliver 1.06 V sine waves with equally spaced phase shifts ($0, \pi/2, \pi,$ and $3\pi/2$ radians). The 24-well plate provides a balance between human scale and reasonably delivered voltages (1-4 V). A custom electrode construct using this geometrical configuration was manufactured on a printed circuit board (PCB) with the capability to stimulate three dishes simultaneously with one sham dish (Figure 4.2).

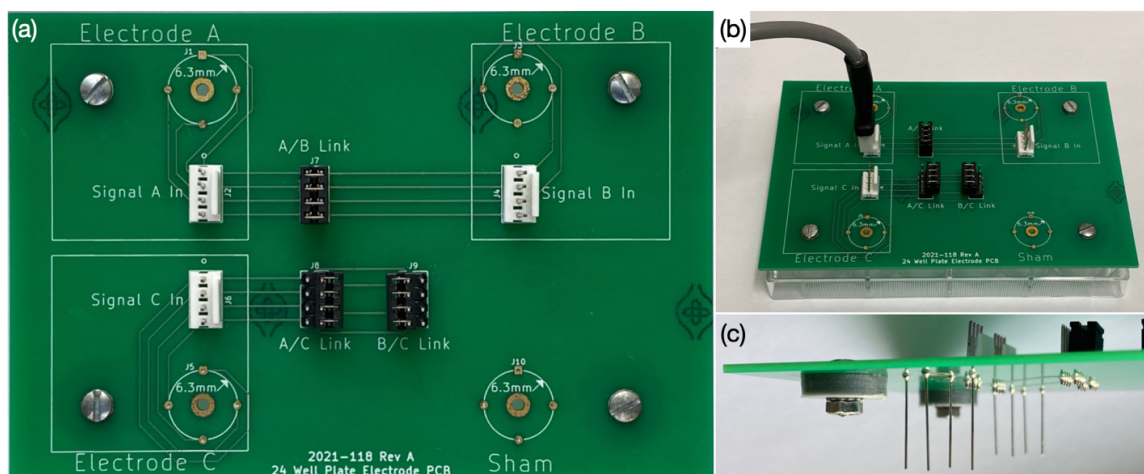


Figure 4.2: Custom designed printed circuit board (PCB) including (a) three stimulating electrode wells labelled “Electrode A”, “Electrode B” and “Electrode C”, and a Sham well. Each well is individually stimulated via the Signal In connector (white) or can be connected to other wells to provide identical stimulation using the corresponding links (A/B Link, A/C Link, B/C Link). Four Platinum Iridium wire electrodes are included in each well, located 6.3 mm from the center. (b) PCB fitted to the 24-well plate and connected to a 4-channel waveform generator with unique stimulation delivered to each electrode in well “Electrode A”. The A/B Link is connected in this case to provide identical stimulation to the top two wells. (c) The wire electrodes extend below the PCB, with a length that touches the bottom of the well.

4.3.3 Experiment Design Optimization

The optimal stimulation for the 200 kHz (and 10 kHz) rotating 1 V/cm average electric field in experiment (a) and (c) (Figure 4.3) is to apply equally spaced phase shifts (0 , $\pi/2$, π , and $3\pi/2$ radians) to each electrode with 1.06 V amplitude sinusoidal waveforms. The impedance for this model was computed in COMSOL to be 113Ω , with a current amplitude of 9.41 mA, and an average power of 4.99 mW per electrode, for a total of 20.0 mW for this configuration. An explanation of impedance and current calculations are included in the supplementary materials. Field magnitudes of 1.5 V/cm and 2 V/cm for this rotating field required programmed voltage increases to 1.59 V and 2.12 V respectively (with an accompanying increase in current and power).

The non-rotating electric field in experiment (b) (Figure 4.3) contains two consecutive stimulating electrodes with 0 phase shift, and two consecutive ground electrodes, and a voltage of 2.3 V applied to the two stimulating electrodes, resulting in 1 V/cm field coverage. The simulated impedance was calculated to be 225 Ω , with a current amplitude of 10.2 mA and average power of 11.7 mW per active electrode, for a total power dissipation of 23.5 mW for this configuration.

For the final experiment (d), alternating ground and 1.06 V stimulating electrodes (same voltage as rotating scenario) produced a field of 0 V/cm in the center of the dish (Figure 4.3). This configuration resulted in an impedance of 171 Ω , current of 6.19 mA, and average power of 3.28 mW per electrode (6.56 mW total). The resulting electric field had an average 0.6 V/cm magnitude over the whole well, with the central 3 mm radius being covered with only 0.2 V/cm. Adjusting the voltage in this configuration to 1.86 V resulted in a total system power of 20.0 mW, the same as the rotating scenario, and an average electric field of 1 V/cm to the whole dish and 0.4 V/cm to the central 3 mm.

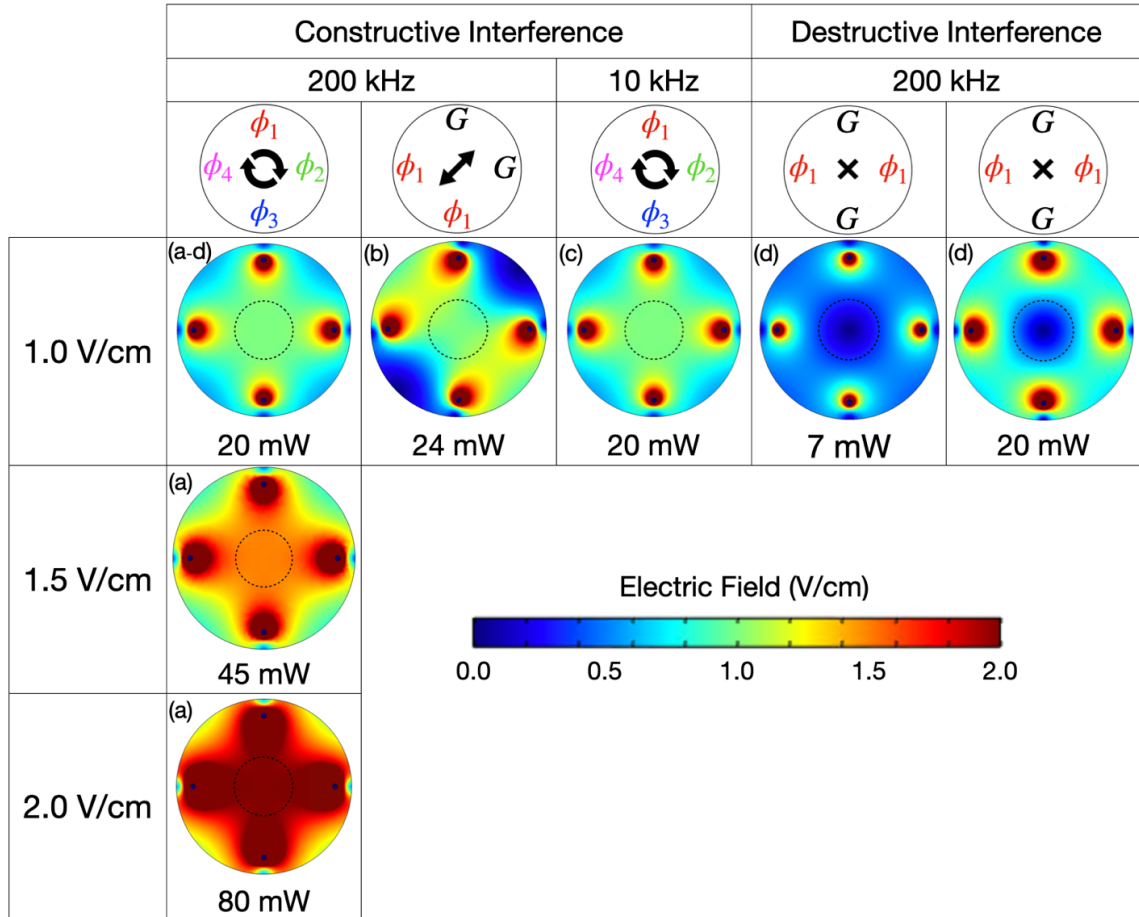


Figure 4.3: Summary of *in vitro* experiment designs, beginning with (a) 200 kHz rotating electric fields at magnitudes of 1, 1.5 and 2 V/cm, to determine the cell survival curve. Voltage and phase parameters were optimized for electric field coverage at the corresponding magnitude and homogeneity to the central 3 mm radius. Rotating fields were delivered with different voltage waveforms $V(t) = A\sin(2\pi ft - \phi_n)$ to each electrode ($n=1,2,3,4$), where A is the voltage amplitude, t is time, f is the frequency, and ϕ_n is the phase shift. Experiment (b) compares field rotation to no rotation by grounding (G) two adjacent electrodes and (c) compares a different rotating field frequency of 10 kHz, all with voltage configurations optimized to cover the central 3 mm radius with 1 V/cm. (d) Destructive interference configurations contain alternating ground (G) and stimulating electrodes: voltage matched (left) or power matched (right) to the rotating scenario,

resulting in a field cancellation to 0 V/cm in the center. See Appendix E for animation of this figure.

The programmed voltage required to deliver the correct voltage to the electrodes (compensating for the load impedance-induced voltage drop) was validated at the time of each experiment by measuring the delivered voltage with a four-channel oscilloscope, with results summarized in the supplementary materials (Figure E.1).

4.3.4 In Vitro IMT Model

Exposure of GBM23 cells to field magnitudes of 1 V/cm, 1.5 V/cm and 2 V/cm yielded field intensity dependent BLI peak signal, corresponding to mean cell viability fraction, of 0.58 ± 0.05 (n=6), 0.37 ± 0.03 (n=6), and 0.021 ± 0.006 (n=6) relative to sham (Figure 4.4). Cell survival results S were fit to a modified linear quadratic (LQ) model $S = A(e^{-(\alpha E + \beta E^2)} - 1) + 1$, where E is the electric field intensity, with best fit parameters to be $A = 25.1$, $\alpha = 0.012$ and $\beta = 0.0038$. This curve fit had an R-square value of 0.95.

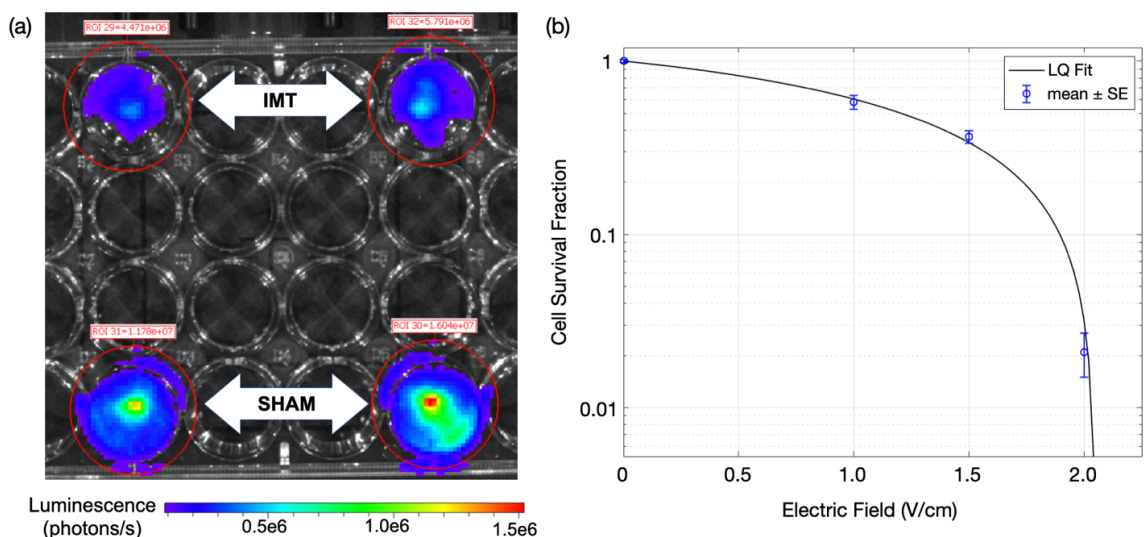


Figure 4.4: (a) Bioluminescence image after 3 days of 1.5 V/cm average IMT electric fields to the top two wells. Bottom two wells were not stimulated, to provide two sham conditions. (b) The cell survival curve for increasing electric field magnitudes. Data is plotted as the mean \pm standard error in blue, and the data was fit to a linear quadratic model $S = A(e^{-(\alpha E + \beta E^2)} - 1) + 1$ in black ($R^2=0.95$).

Comparison between 200 kHz rotating and non-rotating fields at 1 V/cm, as well as 10 kHz rotating fields were analyzed for cell lines GBM23 and GBM25, where no statistical differences in cell viability were observed (Figure 4.5). Rotating electric fields at 1 V/cm resulted in mean 0.53 ± 0.03 viability fraction (n=12), non-rotating 1 V/cm fields resulted in 0.55 ± 0.06 viability (n=12, p=0.84), and 10 kHz rotating resulted in 0.49 ± 0.04 cell viability fraction (n=12, p=0.39). Applying a non-rotating electric field at the same voltage as the rotating case, but with destructive interference at 200 kHz to both cells lines resulted in a mean 0.99 ± 0.02 (n=12) cell viability fraction relative to sham, statistically significant compared to the optimized rotating case with 0.53 ± 0.03 viability relative to sham (p<0.001). Using the same power consumption as the rotating case, the destructive interference model applied to GBM23 cells resulted in a mean 0.66 ± 0.03 viability relative to sham, statistically significant (n=6, p<0.01) when compared to the rotating case performed in parallel, with 0.47 ± 0.04 viability relative to sham (Figure 4.6).

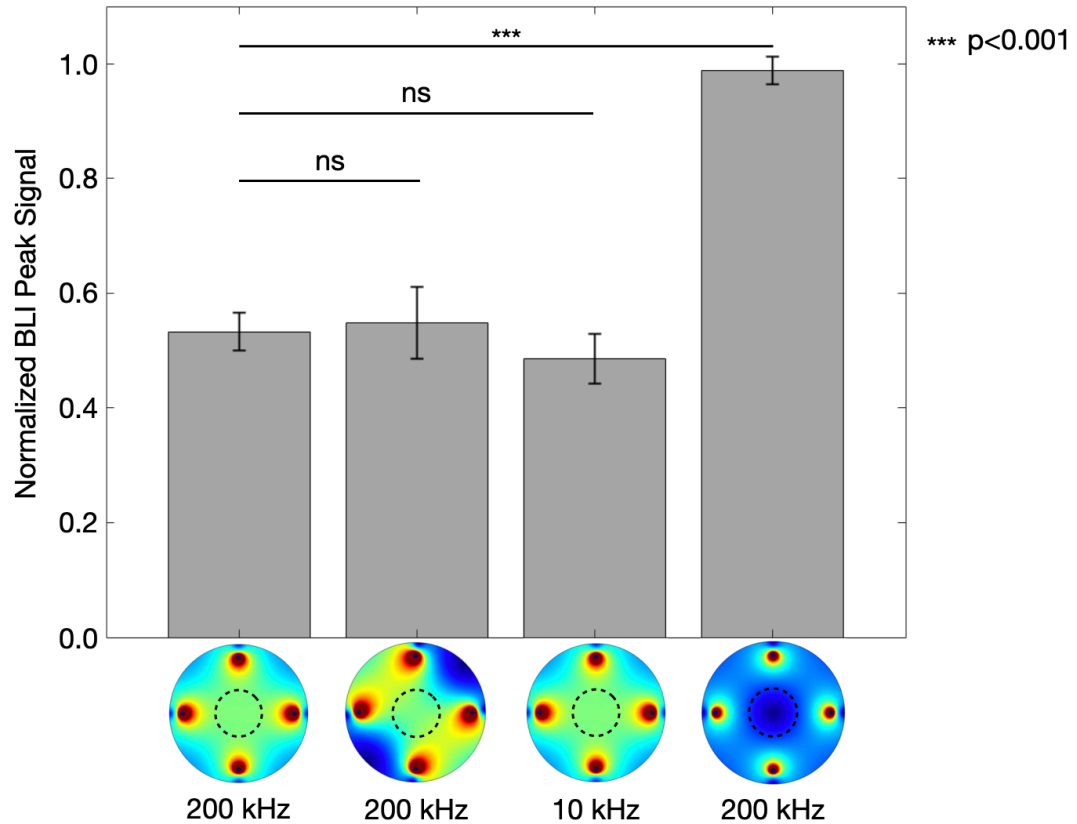


Figure 4.5: Mean of the BLI peak signal normalized to sham \pm standard error, proportional to the cell survival, for the cases of constructive interference 200 kHz rotating fields (0.53 ± 0.03 , $n=12$), 200 kHz non-rotating (0.55 ± 0.06 , $n=12$), 10 kHz rotating fields (0.49 ± 0.04 , $n=12$), and destructive interference 200 kHz voltage matched non-rotating fields (0.99 ± 0.02 , $n=12$).

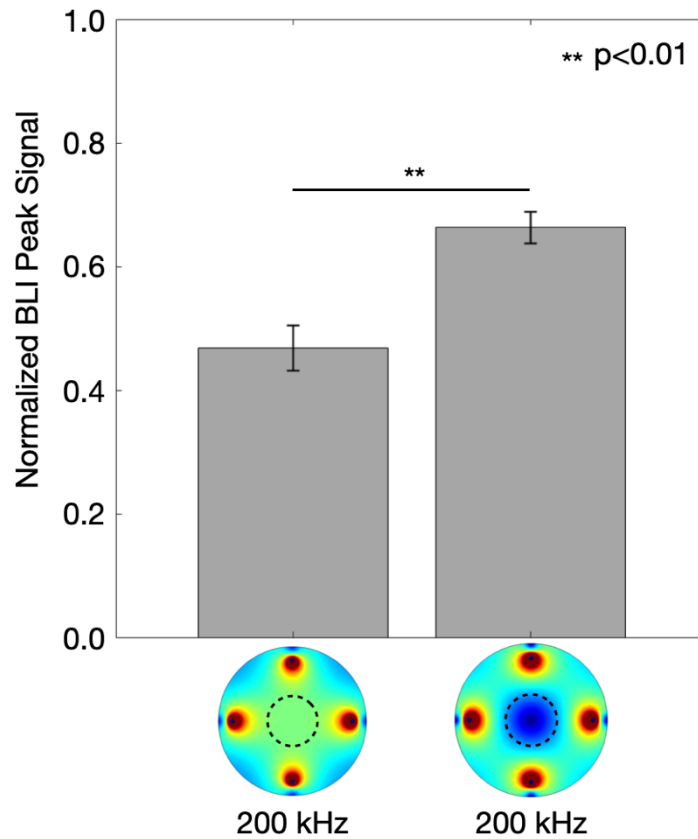


Figure 4.6: Mean of the BLI peak signal normalized to sham \pm standard error, proportional to the cell survival, for the cases of constructive interference 200 kHz rotating fields (0.47 ± 0.04 , $n=6$) and destructive interference power matched (0.66 ± 0.03 , $n=6$).

4.4 Discussion

In this study, the theoretical improvement to target coverage and homogeneity from rotating electric fields generated by multiple electrodes was investigated *in vitro* for the first time. The impact of spatiotemporally dynamic electric fields on GBM cell viability was investigated by first validating that the desired electric field was delivered to preclinical models, by adjusting the programmed voltage to account for the voltage drop. The measured delivered voltage for a two-electrode *in vitro* scenario was used to determine the electrical conductivity of the *in vitro* media as 1.5 ± 0.1 S/m, using a geometrically accurate COMSOL simulation model. With the electrical conductivity

known, COMSOL simulations can be used to determine the necessary applied voltage that is required to produce the desired electric field at the target. For preclinical experiments, the simulated voltage adjustment was also validated prior to stimulation by measuring the delivered voltage to the circuit. The electrical conductivity for DMEM computed in this study was compared to values presented in the literature. Due to the temperature sensitivity of electrical conductivity, only literature comparisons at 37°C were considered. Furthermore, below 10 MHz, electrolytic conductivity is considered frequency independent²⁶. Compared to the value for DMEM of 1.5 ± 0.1 S/m determined in section 4.3.1; the literature value of 1.4 ± 0.1 S/m²³ matches our measurement within the uncertainty.

Computer simulations of the *in vitro* experimental model, used in conjunction with the IMT optimization algorithm to design a four-electrode IMT device provided a platform to demonstrate the impact of rotational fields. Electrodes placed 6.3 mm from the center of a 24-well plate most closely represented the largest spherical tumour volume coverable with four electrodes, previously found to be a 2.1 cm diameter tumour with electrodes placed 7.5 mm from the center¹². For this geometry to produce optimal fields, each electrode must be separately programmable, a key feature of the IMT PCB and accompanying four-channel waveform generator. Expansion to the use of multiple electrodes in IMT has been theoretically supported^{11,12}, with the impact on cell viability investigated for the first time in this work.

The custom IMT *in vitro* delivery device and experiments were implemented on patient derived GBM cell lines and cell viability was observed with BLI. Rotating fields were effective at reducing cell viability in a field intensity dependent manner. Cell survival results S were fit to a modified LQ model with an R-square value of 0.95. This data fit suggests that, similar to radiotherapy, cells exposed to IMT fields have intrinsic linear and quadratic parameters, α and β , that influence cell survival (Figure 4.4). With efficacy found to be dependent on not only field intensity, but field direction and exposure time²⁸, it is important to consider such factors. Current external electric field devices provide only two field directions and have just begun to consider the impact of fractional anisotropy in the brain on the resulting intratumoural electric field. For *in vitro* studies

such as the current investigation, fractional anisotropy is not present, but when expanding IMT to patient models, the fractional anisotropy should be considered for impacts on rotating fields applied with intratumoural electrodes.

We did not find statistical difference in response between the spatiotemporal dynamic rotating electric field case vs. the non-rotating case with both delivering the same field magnitude within the 3 mm radius in the center. However, the optimized rotating field had almost 20% lower power consumption (20.0 mW) compared to the non-rotating case (23.5 mW). We also noted that the non-rotating case exhibited field cancellations on the edges of the well, whose impact would be considerable for targets exceeding ~3 mm radius. For the above reasons, spatiotemporally dynamic fields are preferred over their non-rotating counterparts. Interestingly, cell viability was not significantly different between 200 kHz and 10 kHz rotating fields, suggesting that previously thought inefficacious frequencies^{6,16,21,29} could be effective with the rotating paradigm in certain cell lines. Furthermore, when we compared the two cell lines, the survival of GBM23 and GBM25 cells were not significantly different for the 200 kHz rotating scenario ($58 \pm 5\%$ vs. $48 \pm 3\%$) ($p=0.13$), the 10 kHz scenario ($54 \pm 7\%$ vs. $43 \pm 5\%$) ($p=0.23$), or the destructive interference voltage matched case ($97 \pm 4\%$ vs. $101 \pm 3\%$) ($p=0.45$) but were significantly different ($69 \pm 6\%$ vs. $40 \pm 7\%$) for the non-rotating scenario ($p=0.01$) (Figure E.2).

Through destructive interference, we created a central “cold zone” of 0.2 V/cm in the central 3 mm radius of a well with average 0.6 V/cm field, by using the same stimulation voltages as the rotating electric field case, yielding $99 \pm 2\%$ viability experimentally. We then applied the same system power and whole well electric field (1 V/cm) as the rotating case, with a central field of 0.4 V/cm, yielding $66 \pm 3\%$ cell viability experimentally, compared to $47 \pm 4\%$ for the rotating case. This suggests that even though we applied the same stimulation voltages, or the same system power, optimization of field homogeneity is critical for IMT field planning, and supports the methods previously established in IMT optimizations^{11,12}.

Evaluating the efficacy of spatiotemporally dynamic fields experimentally provides insight for future treatment planning optimization goals. Both field coverage and homogeneity will continue to be included as the objective goals with optimization parameters of phase shift, voltage, and electrode placement. Incorporation of field rotation minimizes both field cold spots and power consumption. These qualities are impactful when translating IMT to the patient setting, where maximum coverage with minimal input current is vital to maximizing battery life of IMT implantable waveform generators. We can always do more: more replicates, more cell lines, and/or more comparisons, but we hope we have satisfactorily demonstrated how we designed and implemented a PCB that made performing *in vitro* experiments with multi-electrode stimulations consistent.

4.5 Conclusions

In this proof-of-concept study, the improved impact of electric field optimization was supported through *in vitro* GBM cell survival analysis. Electrical conductivity measurement of DMEM provided accurate optimizable computer simulations, used to determine required voltage, and calculate current and power. *In vitro* experiments designed and applied to patient derived GBM cells highlighted the considerations and effectiveness of using computerized optimization techniques to design subject-specific spatiotemporally dynamic IMT electric fields that minimize power delivered and cold spots within the treatment fields. With a patient-specific dose response of rotating electric fields established, future IMT studies can compare variation between patients, and determine the necessary inputs required for optimization techniques. The concept of spatiotemporally dynamic fields created through optimizing stimulation parameters can be utilized in future translational applications in rodents and patients, to further IMT development.

4.6 Acknowledgements

This work is supported in part by NSERC CGS-D (E.I), NSERC Idea to Innovation Grant (E.W.), NSERC Discovery Grant (E.W.), Cancer Research Society (M.O.H.), the Canada Foundation for Innovation (CFI) (T.P.) and the Western Innovation Fund (M.O.H.).

4.7 Conflicts of Interest

M.O.H. and S.S. are inventors on the following patent that is assigned to “London Health Sciences Centre Research Inc.” (the applicant): CA2985847 entitled “Intratumoral Modulation Therapy”. E.W., M.O.H., T.P., and S.S. are inventors on the following patent application that is assigned to “London Health Sciences Centre Research Inc.” (the applicant): WO2021142549 entitled “Planning and delivery of dynamically oriented electric field for biomedical applications”. The authors have no other competing interests.

4.8 References

1. Nam JY, de Groot JF. Treatment of Glioblastoma. *J Oncol Pract.* 2017;13(10):629-638. doi:10.1200/JOP.2017.025536
2. Swanson KD, Lok E, Wong ET. An Overview of Alternating Electric Fields Therapy (NovoTTF Therapy) for the Treatment of Malignant Glioma. *Curr Neurol Neurosci Rep.* 2016;16(1):8. doi:10.1007/s11910-015-0606-5
3. Shah PP, White T, Khalafallah AM, Romo CG, Price C, Mukherjee D. A systematic review of tumor treating fields therapy for high-grade gliomas. *J Neurooncol.* 2020;148(3):433-443. doi:10.1007/s11060-020-03563-z
4. Hottinger AF, Pacheco P, Stupp R. Tumor treating fields: a novel treatment modality and its use in brain tumors. *Neuro Oncol.* 2016;18(10):1338-1349. doi:10.1093/neuonc/nov182
5. Fabian D, Eibl M del PGP, Alnahhas I, et al. Treatment of glioblastoma (GBM) with the addition of tumor-treating fields (TTF): A review. *Cancers (Basel).* 2019;11(2). doi:10.3390/cancers11020174
6. Kirson ED, Dbalý V, Tovaryš F, et al. Alternating electric fields arrest cell proliferation in animal tumor models and human brain tumors. *Proc Natl Acad Sci.* 2007;104(24):10152-10157. doi:10.1073/pnas.0702916104
7. Lok E, San P, Hua V, Phung M, Wong ET. Analysis of physical characteristics of Tumor Treating Fields for human glioblastoma. *Cancer Med.* 2017. doi:10.1002/cam4.1095
8. Deweyert A, Iredale E, Xu H, Wong E, Schmid S, Hebb MO. Diffuse intrinsic pontine glioma cells are vulnerable to low intensity electric fields delivered by intratumoral modulation therapy. *J Neurooncol.* 2019;143(1):49-56. doi:10.1007/s11060-019-03145-8
9. Di Sebastiano AR, Deweyert A, Benoit S, et al. Preclinical outcomes of Intratumoral Modulation Therapy for glioblastoma. *Sci Rep.* 2018;8(1):7301. doi:10.1038/s41598-018-25639-7

10. Xu H, Bihari F, Whitehead S, Wong E, Schmid S, Hebb MO. In Vitro Validation of Intratumoral Modulation Therapy for Glioblastoma. *Anticancer Res.* 2016;36:71-80.
11. Iredale E, Voigt B, Rankin A, et al. Planning system for the optimization of electric field delivery using implanted electrodes for brain tumor control. *Med Phys.* 2022;49(9):6055-6067. doi:10.1002/mp.15825
12. Iredale E, Deweyert A, Hoover DA, et al. Optimization of multi-electrode implant configurations and programming for the delivery of non-ablative electric fields in intratumoral modulation therapy. *Med Phys.* 2020;47(11):5441-5454. doi:10.1002/mp.14496
13. Wenger C, Miranda PC, Salvador R, et al. A Review on Tumor-Treating Fields (TTFields): Clinical Implications Inferred From Computational Modeling. *IEEE Rev Biomed Eng.* 2018;11:195-207. doi:10.1109/RBME.2017.2765282
14. Wenger C, Salvador R, Bassar PJ, Miranda PC. The electric field distribution in the brain during TTFields therapy and its dependence on tissue dielectric properties and anatomy: a computational study. *Phys Med Biol.* 2015;60(18):7339-7357. doi:10.1088/0031-9155/60/18/7339
15. Miranda PC, Mekonnen A, Salvador R, Bassar PJ. Predicting the electric field distribution in the brain for the treatment of glioblastoma. *Phys Med Biol.* 2014;59(15):4137-4147. doi:10.1088/0031-9155/59/15/4137
16. Wenger C, Giladi M, Bomzon Z, Salvador R, Bassar PJ, Miranda PC. Modeling Tumor Treating Fields (TTFields) application in single cells during metaphase and telophase. In: *Proceedings of the Annual International Conference of the IEEE Engineering in Medicine and Biology Society, EMBS.* ; 2015. doi:10.1109/EMBC.2015.7319977
17. Korshoej AR, Saturnino GB, Rasmussen LK, von Oettingen G, Sørensen JCH, Thielscher A. Enhancing Predicted Efficacy of Tumor Treating Fields Therapy of Glioblastoma Using Targeted Surgical Craniectomy: A Computer Modeling Study. Debinski W, ed. *PLoS One.* 2016;11(10):e0164051. doi:10.1371/journal.pone.0164051
18. Korshoej AR, Hansen FL, Thielscher A, von Oettingen GB, Sørensen JCH. Impact of tumor position, conductivity distribution and tissue homogeneity on the distribution of tumor treating fields in a human brain: A computer modeling study. Debinski W, ed. *PLoS One.* 2017;12(6):e0179214. doi:10.1371/journal.pone.0179214
19. Ballo MT, Urman N, Lavy-Shahaf G, Grewal J, Bomzon Z, Toms S. Correlation of Tumor Treating Fields Dosimetry to Survival Outcomes in Newly Diagnosed Glioblastoma: A Large- Scale Numerical Simulation-Based Analysis of Data from the Phase 3 EF-14 Randomized Trial. *Int J Radiat Oncol Biol Phys.* 2019;104(5). doi:10.1016/j.ijrobp.2019.04.008
20. Stupp R, Taillibert S, Kanner A, et al. Effect of Tumor-Treating Fields Plus Maintenance Temozolomide vs Maintenance Temozolomide Alone on Survival in

- Patients With Glioblastoma. *JAMA*. 2017;318(23):2306. doi:10.1001/jama.2017.18718
21. Kirson ED, Gurvich Z, Schneiderman R, et al. Disruption of Cancer Cell Replication by Alternating Electric Fields. *Cancer Res*. 2004;64(9):3288-3295. doi:10.1158/0008-5472.CAN-04-0083
 22. Arnold WM, Fuhr G. Increasing the permittivity and conductivity of cellular electromanipulation media. In: *Conference Record - IAS Annual Meeting (IEEE Industry Applications Society)*. Vol 2. ; 1994. doi:10.1109/ias.1994.377619
 23. Chen M-T, Jiang C, Vernier PT, Wu Y-H, Gundersen MA. Two-dimensional nanosecond electric field mapping based on cell electropermeabilization. *PMC Biophys*. 2009;2(1). doi:10.1186/1757-5036-2-9
 24. Rominiyi O, Vanderlinden A, Clenton SJ, Bridgewater C, Al-Tamimi Y, Collis SJ. Tumour treating fields therapy for glioblastoma: current advances and future directions. *Br J Cancer*. 2021;124(4):697-709. doi:10.1038/s41416-020-01136-5
 25. Megía García A, Serrano-Muñoz D, Taylor J, Avendaño-Coy J, Gómez-Soriano J. Transcutaneous Spinal Cord Stimulation and Motor Rehabilitation in Spinal Cord Injury: A Systematic Review. *Neurorehabil Neural Repair*. 2020;34(1). doi:10.1177/1545968319893298
 26. Öner M, Kocakoç ID. JMASM 49: A compilation of some popular goodness of fit tests for normal distribution: Their algorithms and MATLAB codes (MATLAB). *J Mod Appl Stat Methods*. 2017;16(2). doi:10.22237/jmasm/1509496200
 27. Grimnes S, Martinsen ØG. *Bioimpedance and Bioelectricity Basics: Third Edition*.; 2014.
 28. Korshoej AR, Sørensen JCH, von Oettingen G, Poulsen FR, Thielscher A. Optimization of tumor treating fields using singular value decomposition and minimization of field anisotropy. *Phys Med Biol*. 2019;64(4):04NT03. doi:10.1088/1361-6560/aafe54
 29. Berkelmann L, Bader A, Meshksar S, et al. Tumour-treating fields (TTFields): Investigations on the mechanism of action by electromagnetic exposure of cells in telophase/cytokinesis. *Sci Rep*. 2019;9(1):7362. doi:10.1038/s41598-019-43621-9

Chapter 5

5 General Discussion and Conclusions

The research outlined in this dissertation provide the initial development of an electric field simulation and optimization-based planning system for multi-electrode IMT. Electric field coverage to target regions was drastically improved with the incorporation of optimizable relative phase shifts, creating spatiotemporally dynamic electric fields, validated for efficacy *in vitro*. This final chapter provides an overview of each main thesis chapter with discussion of the conclusions and limitations of each section, and future directions that this thesis could support.

5.1 Overview and Research Questions

The main question that motivated this research was “*Can tumour coverage and IMT treatment efficiency be improved using multi-electrode spatiotemporally dynamic electric fields optimized using a novel treatment planning system designed specifically for IMT?*”. With IMT being a new treatment method with limited literature, the establishment of treatment planning techniques and investigation into optimal stimulation programming provides a necessary step to translating IMT to patients.

In Chapter 2, multi-electrode IMT was investigated for the first time with the question “*Can an optimization algorithm be pioneered to determine electrode configurations and programming that maximally cover human scale spherical tumours with treatment electric fields?*” With this question in mind, a pattern search optimization strategy was employed in MATLAB with a custom least square objective function that simultaneously maximizes tumour coverage with prescription electric field, and the electric field to under-dosed voxels. The optimization algorithm utilized electric field simulations in COMSOL for each iteration, where the location, voltage and phase shift programming were the optimization variables. The maximum coverage spherical tumour size was found for 2-7 electrodes, and it was found that the use of phase shift as an optimization variable created electric fields that rotated over time, improving target coverage substantially and minimizing cold spots from field cancellations. It was additionally shown that separately

programmable contacts over the electrode length could improve coverage and increase flexibility of field shaping in 3D.

Chapter 3 expanded on the knowledge gained in Chapter 2 and asked, “*Can a treatment planning system be developed specifically for IMT that incorporates patient-specific tumours and electrode trajectories?*” Considering this objective, the optimization algorithm designed in Chapter 2 was expanded to include non-parallel electrode trajectories and semi-automatic planning in a 3D Slicer based interface. The system includes modules to contour patient MR or CT images, smooth contoured brain, and tumour volumes, plan the initial electrode trajectories, optimize, and visualize the electric field and 3D electrode trajectories. This novel planning system improved on computation time by making use of electric field superposition for objective calculation. The system pipeline was validated through the robot-assisted implantation of multiple electrodes in a brain phantom. Pre-implantation images of the phantom were used to plan the treatment, and post-implantation CT images were used to validate the post-op planning pipeline for stimulation parameter adjustment accounting for trajectory inaccuracies. Planned stimulation was applied to implanted electrodes to validate the delivered electric field matched the planned field. A user guide was created to accompany the planning system, found in Appendix F.

Chapter 4 asked “*Do theoretically superior spatiotemporally dynamic fields correlate with cancer cell death?*” With Chapters 2 and 3 highlighting the theoretical benefits of spatiotemporally dynamic electric fields, it was necessary to investigate the impact of this paradigm on cancer cells. First, the electrical conductivity of the culturing media was measured to enable accurate computer simulations. The planning system developed in Chapter 3 was used to design *in vitro* experiments that compared rotating to non-rotating fields, 200 kHz to 10 kHz stimulation, and the dose response curve for patient derived GBM cell lines. A purpose-build printed-circuit board was developed to apply repeatable 4-electrode stimulation to multiple wells simultaneously. Electric fields that were optimized for target coverage with minimal field cancellations resulted in significant reduction in cell viability compared to non-optimized configurations of the same stimulation power. Cells exposed to spatiotemporally dynamic fields were found to

decrease in viability in a field dependent manner, and rotating fields at 10 kHz and 200 kHz did not show a difference in outcome.

Through the development of an optimization algorithm in Chapter 2, the development of a treatment planning system and phantom validation in Chapter 3, and *in vitro* validation in Chapter 4, it has been shown that spatiotemporally dynamic electric fields delivered using multi-electrode IMT have the capacity to cover patient-specific lesions with the target electric field.

5.2 Limitations

The work presented in this thesis contains limitations which will be discussed here, in addition to discussion on how study specific limitations were mitigated in later chapters.

The limitations to the study presented in Chapter 2 include the use of parallel electrodes of equal depth, the use of spherical tumours, manual optimization, and long computation times. To establish base electrode configurations to approximate coverable tumour size, only spherical tumours were considered with parallel electrodes of equal depth. These limitations were mitigated in Chapter 3, where irregular patient-specific tumours were considered with non-parallel electrodes of optimizable trajectory and depth. In this initial study the optimization algorithm required manual inputs to the MATLAB code and manual creation of COMSOL models. For each optimization, the number and type of optimization parameters (location, phase shift, voltage) had to be input, along with the file names and details from the COMSOL model. The COMSOL simulation file was created for each scenario (3-electrode, 4-electrode, etc.) and tumour size. These manual requirements contributed to the long computation time, and were mitigated in Chapter 3, where the algorithm was semi-automated. The COMSOL models are created automatically, and the optimization run automatically based on the user selections in the graphical user interface, removing any user interaction with MATLAB or COMSOL. Finally, the long computation times (~24 hours) for these initial optimizations were drastically reduced in Chapter 3, down to under 1 hour for phase and voltage optimization, and 4-8 hours for location-based optimizations. This was accomplished by reducing the number of required simulations by incorporating the superposition of each

electrode's electric field into the objective function calculation for any non-location parameter adjustment.

The limitations to the work in Chapter 3 include long computation times (4-8 hours) for location-based optimizations, no differentiation between necrotic core and enhancing tumour, and assumption of electrical conductivity homogeneity. While the computation time was reduced substantially from previous work, treatment plans including the optimization of electrode trajectory still require 4-8 hours to process. Parallel computing could help further reduce computation time in the future. In the current version of the planning system, the tumour is assumed as a homogeneous volume without the inclusion of a necrotic core. The different electrical properties of necrotic tissue, if present, will impact electric field distribution. The electrical conductivity in the surrounding brain is also considered homogeneous, and though the conductivity anisotropies are not expected to impact the field within the tumour, it would be beneficial to confirm this in the future.

Lastly, the *in vitro* investigation of Chapter 4 only used two patient derived GBM cell lines limiting external reproducibility, only two frequencies, no MTT data to support BLI, and no temperature measurements reported. In this work, cell lines derived from GBM tissue resected from two patients was used, but direct reproducibility of the results would require commercially available or shared cell lines. Two frequencies were investigated in this study, 200 kHz, found optimal for treating GBM¹, and 10 kHz, the highest frequency available in existing stimulation devices². A wider range of frequencies would provide a better understanding of the impact of rotating field frequency on cell viability. This study used BLI to for cell viability analysis but did not report MTT correlation with BLI. This is a consideration moving forward with *in vitro* work, in addition to now including temperature measurements to report any confounding effects.

5.3 Future Directions

With IMT still in the preclinical stages, and this thesis presenting the early establishment of a planning system and optimization strategies, there are still many avenues of research that this thesis can support moving forward including biological experiments, computational improvements, and device development.

5.3.1 Biological

Further investigations on IMT spatiotemporally dynamic electric fields *in vitro* are currently underway with spheroids and organoids, to confirm that efficacy results in 2D cultures translate to 3D. Temperature measurements are being included in this work to ensure the observed effects are non-thermal, as reported in the literature for these electric field magnitudes³⁻⁵. The impact of frequency on viability is suggested as future work since the frequency was found to be an important consideration for non-rotating fields³⁻⁶ but did not show the same effect for rotating fields, shown in Chapter 4. Experimentation on additional cell lines including commercially available GBM, other cancers, and normal neurons or fibroblasts could provide information shaping treatment planning goals. While non-rotating IMT fields have been shown to not impact normal cell function^{7,8}, it would be necessary to show this translates to rotating IMT electric fields. The impacts of duty cycle can also be investigated in tumour and normal brain organoids and spheroids⁹ treated with spatiotemporally dynamic fields.

The application of rotating fields *in vivo* is also underway in a rat model using a 3-electrode paradigm, an essential step to support future clinical translation of IMT. Tumour and non-tumour bearing rats treated with spatiotemporally dynamic IMT of different field magnitude and frequency are suggested investigations. As discussed in Chapter 1, the mechanisms of low intensity electric fields have yet to be definitively elucidated, especially when considering the spatiotemporally dynamic fields. Investigation into the role of field rotation on known potential mechanisms, especially the anti-mitotic dielectrophoretic mechanism, would be of particular interest for future work.

5.3.2 Computational

As mentioned in section 5.2, the incorporation of parallel computing could improve the computation time of the optimization component of the planning system and is worth investigating. Research into additional brain segmentations (necrotic core, enhancing tumour, white matter, grey matter, and cerebrospinal fluid¹⁰⁻¹²) and the impact on treatment plans could support whether these additional time-consuming steps are worth incorporating. At the present time the electrical conductivity of patient brain and tumour

tissue are chosen from the literature, but with variability between individuals, patient-specific brain and tumour conductivity measurements or maps could be beneficial, possibly attained through MRI techniques¹³. The accuracy of electric field simulations could also be analyzed, considering imaging, electrode localization and finite element discretization uncertainties. These potential improvements could be implemented in future versions of the planning system if supported by research findings.

So far, the planning system has focused on the treatment of unresectable solid tumours using multiple implanted multi-contact cylindrical electrodes. Research is currently underway for cases of sub-total surgical resection, where the remaining tissue surrounding the surgical resection cavity is treated with IMT fields. This type of treatment would require a different electrode design, and it has been suggested that a mesh of electrodes could cover the surrounding tissue. The optimal shape and size of the mesh electrodes, in addition to the stimulation parameters can be determined using the existing planning system with an updated “surgical resection cavity planning” option. This testing began with spherical cavities and margins to determine which electrode type (disc, ring, square or wire electrodes), size and separation had the most robust coverage capacity. It is proposed that during surgical resection, the electrode array mesh would be placed in the cavity, and post-surgery, the actual implant locations of electrodes will be localized on MRI to plan the ideal stimulation to cover the cavity margins.

5.3.3 Device Development

The final area of potential research is in the development of human IMT devices to treat solid tumours or surgical resection cavity margins. In the case of solid tumours, multi-contact implantable electrodes would be required, powered through an implantable waveform generator, similar to DBS¹⁴, but with multiple, separately programmable channels for each electrode contact. It has yet to be determined the contact height and spacing that is ideal for treatment, so this would be the first step in moving towards prototype development. This could be accomplished using the existing planning systems by adding contact height and spacing as optimization variables. For surgical resection cavity margin treatment, a prototype of an implantable electrode mesh could be

developed. These patient device prototypes would support the translation to clinical trials in the future.

5.4 Significance

IMT has shown promise as a new treatment modality for brain cancers, through preclinical investigations^{7,8}, and the three published works presented in this dissertation. The complexities of planning electric field treatment from multiple electrodes from the inherent field vector cancellations support the need for computational planning methods. The novel optimization algorithm and treatment planning system presented in Chapters 2 and 3 allow for treatment providers to plan IMT delivery to patient-specific tumours of any size and location, with chosen number of electrodes and electric field dose. The goal of an implantable IMT device would be for patients to receive treatment with no outwardly visible devices, and with an established planning system and phantom validation, IMT is one step closer to this goal. This system is of vital importance to the future application of IMT in clinical trials.

This thesis provided, for the first time, an IMT optimization strategy that uses electric field computer simulations to determine the trajectories, relative phase shift and voltage programming of multiple electrodes for patient-specific brain tumours. It has been shown that rotating electric fields provide homogeneous coverage of human scale tumours. Application of a mock IMT treatment on a realistic brain phantom highlighted the potential for human IMT using robot assisted electrode implantation. The novel use of spatiotemporally dynamic electric fields for IMT established in Chapter 2, and the associated validation of delivery potential in Chapter 3 and impact on GBM cell death in Chapter 4 has shaped the future of IMT technology. This work in combination with the ongoing preclinical work *in vitro* and *in vivo*, support future pilot clinical investigations of IMT for safety and efficacy.

As with all treatment modalities, pros and cons exist that need to be considered when choosing a strategy for each patient. Currently, the external TTFIELDS device is approved by the FDA and Health Canada for treatment of GBM. The benefits of this technique are that it is non-surgical, selectively impacts tumour growth. Conversely, external devices

are limited in their coverage capacity for tumours located in the deep brain and are associated with a negative impact on quality of life from having to maintain a shaved scalp while transporting the connected waveform generator for at least 18 hours per day. IMT provides an alternative to TTFields that applies these anti-cancer electric fields from implanted electrodes, allowing for tumours in the deep brain to be treatable, and no outwardly visible devices to improve quality of life. While there are benefits to IMT's internal placement, it is still in the preclinical stages and requires surgical intervention. Ultimately, patients who are not candidates for the external device can benefit from the present work.

5.5 References

1. Rominiyi O, Vanderlinden A, Clenton SJ, Bridgewater C, Al-Tamimi Y, Collis SJ. Tumour treating fields therapy for glioblastoma: current advances and future directions. *Br J Cancer*. 2021;124(4):697-709. doi:10.1038/s41416-020-01136-5
2. Megía García A, Serrano-Muñoz D, Taylor J, Avendaño-Coy J, Gómez-Soriano J. Transcutaneous Spinal Cord Stimulation and Motor Rehabilitation in Spinal Cord Injury: A Systematic Review. *Neurorehabil Neural Repair*. 2020;34(1):3-12. doi:10.1177/1545968319893298
3. Kirson ED, Gurvich Z, Schneiderman R, et al. Disruption of Cancer Cell Replication by Alternating Electric Fields. *Cancer Res*. 2004;64(9):3288-3295. doi:10.1158/0008-5472.CAN-04-0083
4. Kirson ED, Dbalý V, Tovaryš F, et al. Alternating electric fields arrest cell proliferation in animal tumor models and human brain tumors. *Proc Natl Acad Sci*. 2007;104(24):10152-10157. doi:10.1073/pnas.0702916104
5. Berkelmann L, Bader A, Meshksar S, et al. Tumour-treating fields (TTFields): Investigations on the mechanism of action by electromagnetic exposure of cells in telophase/cytokinesis. *Sci Rep*. 2019;9(1):7362. doi:10.1038/s41598-019-43621-9
6. Wenger C, Giladi M, Bomzon Z, Salvador R, Basser PJ, Miranda PC. Modeling Tumor Treating Fields (TTFields) application in single cells during metaphase and telophase. In: *2015 37th Annual International Conference of the IEEE Engineering in Medicine and Biology Society (EMBC)*. IEEE; 2015:6892-6895. doi:10.1109/EMBC.2015.7319977
7. Deweyert A, Iredale E, Xu H, Wong E, Schmid S, Hebb MO. Diffuse intrinsic pontine glioma cells are vulnerable to low intensity electric fields delivered by intratumoral modulation therapy. *J Neurooncol*. 2019;143(1):49-56. doi:10.1007/s11060-019-03145-8

8. Di Sebastiano AR, Deweyert A, Benoit S, et al. Preclinical outcomes of Intratumoral Modulation Therapy for glioblastoma. *Sci Rep.* 2018;8(1):7301. doi:10.1038/s41598-018-25639-7
9. Ye E, Lee JE, Lim YS, Yang SH, Park SM. Effect of duty cycles of tumor-treating fields on glioblastoma cells and normal brain organoids. *Int J Oncol.* 2022;60(1). doi:10.3892/ijo.2021.5298
10. Singh MK, Singh KK. A review of publicly available automatic brain segmentation methodologies, machine learning models, recent advancements, and their comparison. *Ann Neurosci.* 2021;28(1-2):82-93. doi:10.1177/0972753121990175
11. Wang Y, Wang Y, Zhang Z, et al. Segmentation of gray matter, white matter, and CSF with fluid and white matter suppression using MP2RAGE. *J Magn Reson Imaging.* 2018;48(6):1540-1550. doi:10.1002/jmri.26014
12. Dora L, Agrawal S, Panda R, Abraham A. State-of-the-art methods for brain tissue segmentation: a review. *IEEE Rev Biomed Eng.* 2017;10:235-249. doi:10.1109/RBME.2017.2715350
13. Michel E, Hernandez D, Lee SY. Electrical conductivity and permittivity maps of brain tissues derived from water content based on T1-weighted acquisition. *Magn Reson Med.* 2017;77(3):1094-1103. doi:10.1002/mrm.26193
14. Krauss JK, Lipsman N, Aziz T, et al. Technology of deep brain stimulation: current status and future directions. *Nat Rev Neurol.* 2021;17(2):75-87. doi:10.1038/s41582-020-00426-z

Appendices

Appendix A – Permission to Reproduce Content

JOHN WILEY AND SONS LICENSE TERMS AND CONDITIONS

Jan 17, 2023

This Agreement between Ms. Erin Iredale ("You") and John Wiley and Sons ("John Wiley and Sons") consists of your license details and the terms and conditions provided by John Wiley and Sons and Copyright Clearance Center.

License Number 5471481080419

License date Jan 17, 2023

Licensed Content Publisher John Wiley and Sons

Licensed Content Publication Medical Physics

Licensed Content Title Optimization of multi-electrode implant configurations and programming for the delivery of non-ablative electric fields in intratumoral modulation therapy

Licensed Content Author Erin Iredale, Andrew Deweyert, Douglas A. Hoover, et al

Licensed Content Date Oct 13, 2020

Licensed Content 47

Volume

Licensed
Content Issue 11

Licensed
Content Pages 14

Type of use Dissertation/Thesis

Requestor
type Author of this Wiley article

Format Electronic

Portion Full article

Will you be
translating? No

Title Spatiotemporal Optimization of Intratumoral Electric Field Modulation for
Cancer Therapy

Institution
name Western University

Expected
presentation
date Mar 2023

Ms. Erin Iredale
1151 Richmond St

Requestor
Location London, ON N6A 3K7
Canada

JOHN WILEY AND SONS LICENSE
TERMS AND CONDITIONS

Jan 17, 2023

This Agreement between Ms. Erin Iredale ("You") and John Wiley and Sons ("John Wiley and Sons") consists of your license details and the terms and conditions provided by John Wiley and Sons and Copyright Clearance Center.

License Number 5471481310535

License date Jan 17, 2023

Licensed Content
Publisher John Wiley and Sons

Licensed Content
Publication Medical Physics

Licensed Content
Title Planning system for the optimization of electric field delivery using
implanted electrodes for brain tumor control

Licensed Content
Author Erin Iredale, Brynn Voigt, Adam Rankin, et al

Licensed Content
Date Jul 10, 2022

Licensed Content
Volume 49

Licensed Content
Issue 9

Licensed Content Pages	13
Type of use	Dissertation/Thesis
Requestor type	Author of this Wiley article
Format	Electronic
Portion	Full article
Will you be translating?	No
Title	Spatiotemporal Optimization of Intratumoral Electric Field Modulation for Cancer Therapy
Institution name	Western University
Expected presentation date	Mar 2023
Requestor Location	Ms. Erin Iredale 1151 Richmond St London, ON N6A 3K7 Canada Attn: Ms. Erin Iredale
Publisher Tax ID	EU826007151
Total	0.00 CAD

Terms and Conditions

TERMS AND CONDITIONS

This copyrighted material is owned by or exclusively licensed to John Wiley & Sons, Inc. or one of its group companies (each a "Wiley Company") or handled on behalf of a society with which a Wiley Company has exclusive publishing rights in relation to a particular work (collectively "WILEY"). By clicking "accept" in connection with completing this licensing transaction, you agree that the following terms and conditions apply to this transaction (along with the billing and payment terms and conditions established by the Copyright Clearance Center Inc., ("CCC's Billing and Payment terms and conditions"), at the time that you opened your RightsLink account (these are available at any time at <http://myaccount.copyright.com>).

Terms and Conditions

- The materials you have requested permission to reproduce or reuse (the "Wiley Materials") are protected by copyright.
- You are hereby granted a personal, non-exclusive, non-sub licensable (on a stand-alone basis), non-transferable, worldwide, limited license to reproduce the Wiley Materials for the purpose specified in the licensing process. This license, **and any CONTENT (PDF or image file) purchased as part of your order**, is for a one-time use only and limited to any maximum distribution number specified in the license. The first instance of republication or reuse granted by this license must be completed within two years of the date of the grant of this license (although copies prepared before the end date may be distributed thereafter). The Wiley Materials shall not be used in any other manner or for any other purpose, beyond what is granted in the license. Permission is granted subject to an appropriate acknowledgement given to the author, title of the material/book/journal and the publisher. You shall also duplicate the copyright notice that appears in the Wiley publication in your use of the Wiley Material. Permission is also granted on the understanding that nowhere in the text is a previously published source acknowledged for all or part of this Wiley Material. Any third party content is expressly excluded from this permission.
- With respect to the Wiley Materials, all rights are reserved. Except as expressly granted by the terms of the license, no part of the Wiley Materials may be copied, modified, adapted (except for minor reformatting required by the new Publication), translated, reproduced, transferred or distributed, in any form or by any means, and no derivative works may be made based on the Wiley Materials without the prior permission of the respective copyright owner. **For STM Signatory Publishers clearing permission under the terms of the [STM Permissions Guidelines](#) only, the terms of the license are extended to include subsequent editions and for editions in other languages, provided such editions are for the work as a whole in situ and does not involve the separate exploitation of the permitted figures or extracts,**

You may not alter, remove or suppress in any manner any copyright, trademark or other notices displayed by the Wiley Materials. You may not license, rent, sell, loan, lease, pledge, offer as security, transfer or assign the Wiley Materials on a stand-alone basis, or any of the rights granted to you hereunder to any other person.

- The Wiley Materials and all of the intellectual property rights therein shall at all times remain the exclusive property of John Wiley & Sons Inc, the Wiley Companies, or their respective licensors, and your interest therein is only that of having possession of and the right to reproduce the Wiley Materials pursuant to Section 2 herein during the continuance of this Agreement. You agree that you own no right, title or interest in or to the Wiley Materials or any of the intellectual property rights therein. You shall have no rights hereunder other than the license as provided for above in Section 2. No right, license or interest to any trademark, trade name, service mark or other branding ("Marks") of WILEY or its licensors is granted hereunder, and you agree that you shall not assert any such right, license or interest with respect thereto
- NEITHER WILEY NOR ITS LICENSORS MAKES ANY WARRANTY OR REPRESENTATION OF ANY KIND TO YOU OR ANY THIRD PARTY, EXPRESS, IMPLIED OR STATUTORY, WITH RESPECT TO THE MATERIALS OR THE ACCURACY OF ANY INFORMATION CONTAINED IN THE MATERIALS, INCLUDING, WITHOUT LIMITATION, ANY IMPLIED WARRANTY OF MERCHANTABILITY, ACCURACY, SATISFACTORY QUALITY, FITNESS FOR A PARTICULAR PURPOSE, USABILITY, INTEGRATION OR NON-INFRINGEMENT AND ALL SUCH WARRANTIES ARE HEREBY EXCLUDED BY WILEY AND ITS LICENSORS AND WAIVED BY YOU.
- WILEY shall have the right to terminate this Agreement immediately upon breach of this Agreement by you.
- You shall indemnify, defend and hold harmless WILEY, its Licensors and their respective directors, officers, agents and employees, from and against any actual or threatened claims, demands, causes of action or proceedings arising from any breach of this Agreement by you.
- IN NO EVENT SHALL WILEY OR ITS LICENSORS BE LIABLE TO YOU OR ANY OTHER PARTY OR ANY OTHER PERSON OR ENTITY FOR ANY SPECIAL, CONSEQUENTIAL, INCIDENTAL, INDIRECT, EXEMPLARY OR PUNITIVE DAMAGES, HOWEVER CAUSED, ARISING OUT OF OR IN CONNECTION WITH THE DOWNLOADING, PROVISIONING, VIEWING OR USE OF THE MATERIALS REGARDLESS OF THE FORM OF ACTION, WHETHER FOR BREACH OF CONTRACT, BREACH OF WARRANTY, TORT, NEGLIGENCE, INFRINGEMENT OR OTHERWISE (INCLUDING, WITHOUT LIMITATION, DAMAGES BASED ON LOSS OF PROFITS, DATA, FILES, USE, BUSINESS OPPORTUNITY OR CLAIMS OF THIRD PARTIES), AND WHETHER OR NOT THE PARTY HAS BEEN ADVISED OF THE POSSIBILITY OF SUCH DAMAGES. THIS LIMITATION SHALL APPLY NOTWITHSTANDING ANY

FAILURE OF ESSENTIAL PURPOSE OF ANY LIMITED REMEDY PROVIDED HEREIN.

- Should any provision of this Agreement be held by a court of competent jurisdiction to be illegal, invalid, or unenforceable, that provision shall be deemed amended to achieve as nearly as possible the same economic effect as the original provision, and the legality, validity and enforceability of the remaining provisions of this Agreement shall not be affected or impaired thereby.
- The failure of either party to enforce any term or condition of this Agreement shall not constitute a waiver of either party's right to enforce each and every term and condition of this Agreement. No breach under this agreement shall be deemed waived or excused by either party unless such waiver or consent is in writing signed by the party granting such waiver or consent. The waiver by or consent of a party to a breach of any provision of this Agreement shall not operate or be construed as a waiver of or consent to any other or subsequent breach by such other party.
- This Agreement may not be assigned (including by operation of law or otherwise) by you without WILEY's prior written consent.
- Any fee required for this permission shall be non-refundable after thirty (30) days from receipt by the CCC.
- These terms and conditions together with CCC's Billing and Payment terms and conditions (which are incorporated herein) form the entire agreement between you and WILEY concerning this licensing transaction and (in the absence of fraud) supersedes all prior agreements and representations of the parties, oral or written. This Agreement may not be amended except in writing signed by both parties. This Agreement shall be binding upon and inure to the benefit of the parties' successors, legal representatives, and authorized assigns.
- In the event of any conflict between your obligations established by these terms and conditions and those established by CCC's Billing and Payment terms and conditions, these terms and conditions shall prevail.
- WILEY expressly reserves all rights not specifically granted in the combination of (i) the license details provided by you and accepted in the course of this licensing transaction, (ii) these terms and conditions and (iii) CCC's Billing and Payment terms and conditions.
- This Agreement will be void if the Type of Use, Format, Circulation, or Requestor Type was misrepresented during the licensing process.
- This Agreement shall be governed by and construed in accordance with the laws of the State of New York, USA, without regards to such state's conflict of law rules. Any legal action, suit or proceeding arising out of or relating to these Terms and Conditions or the breach thereof shall be instituted in a court of competent jurisdiction in New

York County in the State of New York in the United States of America and each party hereby consents and submits to the personal jurisdiction of such court, waives any objection to venue in such court and consents to service of process by registered or certified mail, return receipt requested, at the last known address of such party.

WILEY OPEN ACCESS TERMS AND CONDITIONS

Wiley Publishes Open Access Articles in fully Open Access Journals and in Subscription journals offering Online Open. Although most of the fully Open Access journals publish open access articles under the terms of the Creative Commons Attribution (CC BY) License only, the subscription journals and a few of the Open Access Journals offer a choice of Creative Commons Licenses. The license type is clearly identified on the article.

The Creative Commons Attribution License

The [Creative Commons Attribution License \(CC-BY\)](#) allows users to copy, distribute and transmit an article, adapt the article and make commercial use of the article. The CC-BY license permits commercial and non-

Creative Commons Attribution Non-Commercial License

The [Creative Commons Attribution Non-Commercial \(CC-BY-NC\) License](#) permits use, distribution and reproduction in any medium, provided the original work is properly cited and is not used for commercial purposes.(see below)

Creative Commons Attribution-Non-Commercial-NoDerivs License

The [Creative Commons Attribution Non-Commercial-NoDerivs License](#) (CC-BY-NC-ND) permits use, distribution and reproduction in any medium, provided the original work is properly cited, is not used for commercial purposes and no modifications or adaptations are made. (see below)

Use by commercial "for-profit" organizations

Use of Wiley Open Access articles for commercial, promotional, or marketing purposes requires further explicit permission from Wiley and will be subject to a fee.

Further details can be found on Wiley Online Library
<http://olabout.wiley.com/WileyCDA/Section/id-410895.html>

Other Terms and Conditions:

v1.10 Last updated September 2015

Questions? customercare@copyright.com or +1-855-239-3415 (toll free in the US) or +1-978-646-2777.

Reusing IOP Published Content

[Home](#) > Reusing IOP Published Content

In order to reuse content published by IOP or its partners, you may need to request express permission. If permission is required, the way you will need to obtain this permission depends on what material you wish to reuse, and how you wish to reuse it. For full details on when permission is required, and how to obtain permission, please read the information below.

When permission is not needed:

There are a few instances in which you don't need permission to reuse IOP published content:

- If you are publishing a **new work with IOP** and wish to reuse content from an **IOP journal or eBook, or a partner journal that we handle permissions for**. IOP already has the permission to use this content, so you do not need to request it again.
- If the content was published on an **open-access** basis that allows the type of reuse you need. For details of open access licences, please see [Creative Commons Licences](#).
- If you are the **original author** of the content you wish to reuse, and your reuse falls within the allowances of our [Author Rights policy](#).

Appendix B – Supplemental Materials for Chapter 1

Anti-mitotic mechanisms have been documented in the literature¹⁻⁷, where cell death was found to correlate with cell doubling time⁸. Prolonged mitosis, abnormal chromosome segregation, multinucleation, spindle assembly checkpoint failure and aneuploidy in surviving cells have all been observed with the application of TTFields^{2,4,7,9-11}. An alternate hypothesis for the reduction in microtubule polymerization is that changes in trans-membrane potential cause an influx of intracellular Ca²⁺ ions^{12,13}. DNA repair has also been documented as a potential mechanism in TTFields^{14,15}. The downregulation of genes such as BRCA1, ATRIP, MLH1, MRE11A, FANCM, FANCD2 and Fanconi anemia pathway genes observed in TTFields treated cells could help explain the role of DNA repair in TTFields efficacy^{14,15}. Following concurrent *in vitro* TTFields and irradiation, an increase in DNA damage (from increased γ -H2AX foci) was observed over time compared to radiation alone, and DNA repair was slowed with increased chromatic aberrations and enhanced mitotic catastrophe^{10,16,17}, supported *in vivo*¹⁸. TTFields in combination with cisplatin was also shown to increase the γ -H2AX foci with additive effects¹⁸. Increased replication stress was observed through an increase in R-loop formation and the impairment of replication forks^{19,20}. Abnormal activation of mTOR and deletion of CDKN2A could contribute to the resistance to TTFields after prolonged treatment²¹. Lastly, homologous recombination repair (HRR) is impaired by the downregulation of BRCA and RAD51²²⁻²⁵ following TTFields plus radiotherapy¹⁶. The timing of concurrent therapies has shown impact on non-small cell lung cancer cells, where electric fields applied prior to radiation showed increased toxicity compared to when applied after radiation¹⁵. Overall, the gene downregulations cause an increase in double strand breaks from replication stress and reduced efficiency of double strand break repair from HRR impairment.

Anti-migratory mechanisms have been proposed after observation of suppression of glioma cell migration and invasion following TTFields treatment, through downregulation of NF- κ B, MAPK, and P13K/Akt, and inhibition of phosphorylation^{10,17,26}. Reductions in metastases *in vivo*^{27,28}, decreased dispersal and migration velocity *in vitro*²⁸, reduction in microtubule formation²⁹, and suppression of

vascular development and endothelial growth factor *in vitro*¹⁷ have supported this mechanism. The upregulation of autophagy is associated with tumour suppression when cancer is in the early stages, but during late stages it is associated with cancer survival and resistance to treatment³⁰. P13K/Akt/mTORC signaling pathways inhibit autophagy, and with their downregulation when exposed to TTFields, autophagy is increased^{31,32}. Cancer cells treated with electric fields exhibited an upregulation of autophagy-related genes, increase in morphological changes³¹, dilated endoplasmic reticula, an increase in the number of autophagosomes and vacuoles^{26,33,34}, and replication stress³⁵, all associated with autophagy. Positive autophagy regulators (AMPK) were also upregulated, while negative regulators (AKT2) were reduced in treated groups^{31,35}. More research is needed to determine if the increased autophagy supports the cytotoxicity of TTFields^{26,31}, or is a resistance mechanism³⁵, as both possibilities have been proposed and are likely influenced by the state of cancer³⁰.

Immunogenic mechanisms of TTFields are of particular interest, as in combination with immunotherapy, they could present possible improvements to treatment outcomes. *In vitro* studies have found evidence of M1 macrophage polarization (pro-inflammatory)^{36,37}, proinflammatory cytokines and markers^{37,38}, MHC II upregulation, CD80 and CD40 markers on dendritic cells, increased phagocytosis, and DAMP secretion (ATP, HMGB1)^{33,39}. Immunogenic cell death can be a response to cell stress, DNA damage, and increases in reactive oxygen, all which have been observed in cells treated with TTFields^{15,34,40}. Increased mRNA expression of IL-1 β and TNF- α in macrophage cells³⁶ and increased reactive oxygen species produced by macrophages was observed following *in vitro* treatment, and found to mediate anti-tumour immunity effects by regulating NF- κ B and MAPK signaling pathways in macrophages, with the potential to overcome the immune escape mechanisms of glioblastoma^{36,41}. *In vivo*, reduced lung metastases burden was observed in treated groups (no treatment applied directly to lung), along with immune markers (in lung tumours) CD4+ (T-helper), CD8+ (cytotoxic T) and CD45+, suggesting the possibility of abscopal effects²⁷. Activation of the cGAS-STING and AIM1 pathways⁴² leading to immune response, and improved tumour control when combined with a PD-1 inhibitor³³ were also observed. One study found that the mitotic catastrophe from fields resulted in micronuclei with weak nuclear envelopes that enable

DNA release into the cytoplasm, activating the cGAS/STING and AIM2 DNA pathways⁴². Increased T-cell (cytotoxic and memory) and dendritic cell activation were observed in the PBMCs of human glioma patients treated with TTFields⁴³. These T cells had increased PD-1 expression, suggesting checkpoint inhibitor concurrent therapy may be advantageous. The number of infiltrating lymphocytes with activation signs was also increased in gliomas from patients following TTFields and chemoradiation⁴³. The increased immunogenic cell death and anti-tumour immunity observed has prompted clinical trials, combining anti-PD-1 therapy and TTFields, that are currently underway for non-small cell lung cancer⁴⁴.

Tumour selective impacts on the cell membrane and blood brain barrier (BBB) are especially promising, with an increase in the number and size of holes in tumour cell membranes when exposed to TTFields compared to normal fibroblast cells⁴⁵. Tumour cells exhibit different electrical properties than normal cells, theoretically leading to increased transmembrane potentials in tumour cells⁴⁶⁻⁴⁹. Various biophysical explanations have been proposed for this increase in cancer cell membrane permeability including ion channel activation influence⁵⁰, membrane destabilization and shape changes (bioelectrorheologic model)⁵¹, and electroporation⁵⁰. TTFields have also been investigated for their impact on the blood brain barrier, where reversible BBB integrity disruption was observed^{52,53}, and chemotherapeutic agents not normally able to cross the BBB appeared to contribute to tumour suppression when combined with TTFields⁵⁴. The enhancement of drug efficacy through BBB crossing provides a potential explanation for the improved survival outcomes with TMZ⁵⁵. While the impact of each potential mechanism (anti-mitotic, DNA repair, anti-migratory, autophagic, immunogenic, and membrane permeability) has yet to be confirmed, it is clear that efficacy lies in synergistic intracellular mechanisms.

References

1. Rominiyi O, Vanderlinden A, Clenton SJ, Bridgewater C, Al-Tamimi Y, Collis SJ. Tumour treating fields therapy for glioblastoma: current advances and future directions. *Br J Cancer*. 2021;124(4):697-709. doi:10.1038/s41416-020-01136-5
2. Kirson ED, Gurvich Z, Schneiderman R, et al. Disruption of Cancer Cell Replication by Alternating Electric Fields. *Cancer Res*. 2004;64(9):3288-3295. doi:10.1158/0008-5472.CAN-04-0083
3. Kirson ED, Dbalý V, Tovaryš F, et al. Alternating electric fields arrest cell proliferation in animal tumor models and human brain tumors. *Proc Natl Acad Sci*. 2007;104(24):10152-10157. doi:10.1073/pnas.0702916104
4. Giladi M, Schneiderman RS, Voloshin T, et al. Mitotic Spindle Disruption by Alternating Electric Fields Leads to Improper Chromosome Segregation and Mitotic Catastrophe in Cancer Cells. *Sci Rep*. 2016;5(1):18046. doi:10.1038/srep18046
5. Wong ET, Lok E, Swanson KD. Alternating Electric Fields Therapy for Malignant Gliomas: From Bench Observation to Clinical Reality. In: *Progress in Neurological Surgery*. Vol 32. ; 2018:180-195. doi:10.1159/000469690
6. Spiliotis ET, Kinoshita M, Nelson WJ. A Mitotic Septin Scaffold Required for Mammalian Chromosome Congression and Segregation. *Science (80-)*. 2005;307(5716):1781-1785. doi:10.1126/science.1106823
7. Gera N, Yang A, Holtzman TS, Lee SX, Wong ET, Swanson KD. Tumor Treating Fields Perturb the Localization of Septins and Cause Aberrant Mitotic Exit. Prigent C, ed. *PLoS One*. 2015;10(5):e0125269. doi:10.1371/journal.pone.0125269
8. Lavy Shahaf G, Giladi M, Schneiderman R, et al. P04.17 Cancer cell lines response to tumor treating fields: results of a meta-analysis. *Neuro Oncol*. 2018;20(suppl_3):iii282-iii282. doi:10.1093/neuonc/noy139.251
9. Tuszynski J, Wenger C, Friesen D, Preto J. An Overview of Sub-Cellular Mechanisms Involved in the Action of TTFIELDS. *Int J Environ Res Public Health*. 2016;13(11):1128. doi:10.3390/ijerph13111128
10. Kim EH, Kim YJ, Song HS, et al. Biological effect of an alternating electric field on cell proliferation and synergistic antimetabolic effect in combination with ionizing radiation. *Oncotarget*. 2016;7(38):62267-62279. doi:10.18632/oncotarget.11407

11. Timmons JJ, Preto J, Tuszyński JA, Wong ET. Tubulin's response to external electric fields by molecular dynamics simulations. Prigent C, ed. *PLoS One*. 2018;13(9):e0202141. doi:10.1371/journal.pone.0202141
12. Gal V, Martin S, Bayley P. Fast disassembly of microtubules induced by Mg²⁺ or Ca²⁺. *Biochem Biophys Res Commun*. 1988;155(3):1464-1470. doi:10.1016/S0006-291X(88)81306-8
13. Hepler PK, Callahan DA. Free calcium increases during anaphase in stamen hair cells of *Tradescantia*. *J Cell Biol*. 1987;105(5):2137-2143. doi:10.1083/jcb.105.5.2137
14. Turner N, Tutt A, Ashworth A. Hallmarks of "BRCAness" in sporadic cancers. *Nat Rev Cancer*. 2004;4(10):814-819. doi:10.1038/nrc1457
15. Karanam NK, Srinivasan K, Ding L, Sishc B, Saha D, Story MD. Tumor-treating fields elicit a conditional vulnerability to ionizing radiation via the downregulation of BRCA1 signaling and reduced DNA double-strand break repair capacity in non-small cell lung cancer cell lines. *Cell Death Dis*. 2017;8(3):e2711-e2711. doi:10.1038/cddis.2017.136
16. Giladi M, Munster M, Schneiderman RS, et al. Tumor treating fields (TTFields) delay DNA damage repair following radiation treatment of glioma cells. *Radiat Oncol*. 2017;12(1):206. doi:10.1186/s13014-017-0941-6
17. Kim EH, Song HS, Yoo SH, Yoon M. Tumor treating fields inhibit glioblastoma cell migration, invasion and angiogenesis. *Oncotarget*. 2016;7(40):65125-65136. doi:10.18632/oncotarget.11372
18. Mumblat H, Martinez-Conde A, Braten O, et al. Tumor Treating Fields (TTFields) downregulate the Fanconi Anemia-BRCA pathway and increase the efficacy of chemotherapy in malignant pleural mesothelioma preclinical models. *Lung Cancer*. 2021;160:99-110. doi:10.1016/j.lungcan.2021.08.011
19. Karanam NK, Ding L, Aroumougame A, Story MD. Tumor treating fields cause replication stress and interfere with DNA replication fork maintenance: Implications for cancer therapy. *Transl Res*. 2020;217:33-46. doi:10.1016/j.trsl.2019.10.003
20. Karanam NK, Ding L, Sishc B, Saha D, Story MD. Abstract 3217: Newly identified role of tumor treating fields in DNA damage repair and replication stress pathways. *Cancer Res*. 2018;78(13_Supplement):3217-3217. doi:10.1158/1538-7445.AM2018-3217
21. Robins HI, Nguyen HN, Field A, Howard S, Salamat S, Deming DA. Molecular Evolution of a Glioblastoma Controlled With Tumor Treating Fields and Concomitant Temozolomide. *Front Oncol*. 2018;8(OCT). doi:10.3389/fonc.2018.00451

22. Davies AA, Masson J-Y, McIlwraith MJ, et al. Role of BRCA2 in Control of the RAD51 Recombination and DNA Repair Protein. *Mol Cell*. 2001;7(2):273-282. doi:10.1016/S1097-2765(01)00175-7
23. Scully R, Chen J, Plug A, et al. Association of BRCA1 with Rad51 in Mitotic and Meiotic Cells. *Cell*. 1997;88(2):265-275. doi:10.1016/S0092-8674(00)81847-4
24. Venkitaraman AR. Functions of BRCA1 and BRCA2 in the biological response to DNA damage. *J Cell Sci*. 2001;114(20):3591-3598. doi:10.1242/jcs.114.20.3591
25. Mason JM, Chan Y-L, Weichselbaum RW, Bishop DK. Non-enzymatic roles of human RAD51 at stalled replication forks. *Nat Commun*. 2019;10(1):4410. doi:10.1038/s41467-019-12297-0
26. Silginer M, Weller M, Stupp R, Roth P. Biological activity of tumor-treating fields in preclinical glioma models. *Cell Death Dis*. 2017;8(4):e2753-e2753. doi:10.1038/cddis.2017.171
27. Kirson ED, Giladi M, Gurvich Z, et al. Alternating electric fields (TTFields) inhibit metastatic spread of solid tumors to the lungs. *Clin Exp Metastasis*. 2009;26(7):633-640. doi:10.1007/s10585-009-9262-y
28. Voloshin T, Schneiderman RS, Volodin A, et al. Tumor Treating Fields (TTFields) Hinder Cancer Cell Motility through Regulation of Microtubule and Actin Dynamics. *Cancers (Basel)*. 2020;12(10):3016. doi:10.3390/cancers12103016
29. Sarkari A, Korenfeld S, Ladner K, et al. Abstract 2011: Tumor treating fields induce cellular and morphologic changes including disruption of intercellular communication networks in malignant pleural mesothelioma. *Cancer Res*. 2021;81(13_Supplement):2011-2011. doi:10.1158/1538-7445.AM2021-2011
30. Yun C, Lee S. The Roles of Autophagy in Cancer. *Int J Mol Sci*. 2018;19(11):3466. doi:10.3390/ijms19113466
31. Kim EH, Jo Y, Sai S, et al. Tumor-treating fields induce autophagy by blocking the Akt2/miR29b axis in glioblastoma cells. *Oncogene*. 2019;38(39):6630-6646. doi:10.1038/s41388-019-0882-7
32. Paquette M, El-Houjeiri L, Pause A. mTOR Pathways in Cancer and Autophagy. *Cancers (Basel)*. 2018;10(1):18. doi:10.3390/cancers10010018
33. Voloshin T, Kaynan N, Davidi S, et al. Tumor-treating fields (TTFields) induce immunogenic cell death resulting in enhanced antitumor efficacy when combined with anti-PD-1 therapy. *Cancer Immunol Immunother*. 2020;69(7):1191-1204. doi:10.1007/s00262-020-02534-7

34. Jo Y, Kim E, Sai S, et al. Functional Biological Activity of Sorafenib as a Tumor-Treating Field Sensitizer for Glioblastoma Therapy. *Int J Mol Sci.* 2018;19(11):3684. doi:10.3390/ijms19113684
35. Shteingauz A, Porat Y, Voloshin T, et al. AMPK-dependent autophagy upregulation serves as a survival mechanism in response to Tumor Treating Fields (TTFIELDS). *Cell Death Dis.* 2018;9(11):1074. doi:10.1038/s41419-018-1085-9
36. Park J-I, Song K-H, Jung S-Y, et al. Tumor-Treating Fields Induce RAW264.7 Macrophage Activation Via NK- κ B/MAPK Signaling Pathways. *Technol Cancer Res Treat.* 2019;18:153303381986822. doi:10.1177/1533033819868225
37. Barsheshet Y, Brant B, Voloshin T, et al. Abstract 1305: Tumor Treating Fields (TTFIELDS) promote a pro-inflammatory phenotype in macrophages. *Cancer Res.* 2022;82(12_Supplement):1305-1305. doi:10.1158/1538-7445.AM2022-1305
38. Wong ET, Timmons J, Swanson KD. Abstract 1707: Tumor treating fields exert cellular and immunologic effects. *Cancer Res.* 2018;78(13_Supplement):1707-1707. doi:10.1158/1538-7445.AM2018-1707
39. Kroemer G, Galluzzi L, Kepp O, Zitvogel L. Immunogenic Cell Death in Cancer Therapy. *Annu Rev Immunol.* 2013;31(1):51-72. doi:10.1146/annurev-immunol-032712-100008
40. Karanam NK, Story MD. An overview of potential novel mechanisms of action underlying Tumor Treating Fields-induced cancer cell death and their clinical implications. *Int J Radiat Biol.* 2021;97(8):1044-1054. doi:10.1080/09553002.2020.1837984
41. Brown NF, Carter TJ, Ottaviani D, Mulholland P. Harnessing the immune system in glioblastoma. *Br J Cancer.* 2018;119(10):1171-1181. doi:10.1038/s41416-018-0258-8
42. Chen D, Le SB, Hutchinson TE, et al. Tumor Treating Fields dually activate STING and AIM2 inflammasomes to induce adjuvant immunity in glioblastoma. *J Clin Invest.* 2022;132(8). doi:10.1172/JCI149258
43. Diamant G, Simchony Goldman H, Gasri Plotnitsky L, et al. T Cells Retain Pivotal Antitumoral Functions under Tumor-Treating Electric Fields. *J Immunol.* 2021;207(2):709-719. doi:10.4049/jimmunol.2100100
44. Weinberg U, Farber O, Giladi M, Bomzon Z, Kirson E. Abstract CT173: Tumor Treating Fields (150 kHz) concurrent with standard of care treatment for stage 4 non-small cell lung cancer (NSCLC) following platinum failure: The Phase III LUNAR study. *Cancer Res.* 2019;79(13_Supplement):CT173-CT173. doi:10.1158/1538-7445.AM2019-CT173

45. Chang E, Patel CB, Pohling C, et al. Tumor treating fields increases membrane permeability in glioblastoma cells. *Cell Death Discov.* 2018;4(1):113. doi:10.1038/s41420-018-0130-x
46. Li X, Yang F, Rubinsky B. A Correlation Between Electric Fields That Target the Cell Membrane Potential and Dividing HeLa Cancer Cell Growth Inhibition. *IEEE Trans Biomed Eng.* 2021;68(6):1951-1956. doi:10.1109/TBME.2020.3042650
47. Yang M, Brackenbury WJ. Membrane potential and cancer progression. *Front Physiol.* 2013;4. doi:10.3389/fphys.2013.00185
48. Kotnik T, Miklavčič D. Analytical Description of Transmembrane Voltage Induced by Electric Fields on Spheroidal Cells. *Biophys J.* 2000;79(2):670-679. doi:10.1016/S0006-3495(00)76325-9
49. Li X, Yang F, Rubinsky B. A Theoretical Study on the Biophysical Mechanisms by Which Tumor Treating Fields Affect Tumor Cells During Mitosis. *IEEE Trans Biomed Eng.* 2020;67(9):2594-2602. doi:10.1109/TBME.2020.2965883
50. Aguilar AA, Ho MC, Chang E, et al. Permeabilizing Cell Membranes with Electric Fields. *Cancers (Basel).* 2021;13(9):2283. doi:10.3390/cancers13092283
51. Pawlowski P, Fikus M. Bioelectrorheological model of the cell 1. Analysis of stresses and deformations. *J Theor Biol.* 1989;137(3):321-337. doi:10.1016/S0022-5193(89)80075-X
52. Salvador E, Kessler A, Hoermann J, et al. Tumor treating fields effects on the blood-brain barrier in vitro and in vivo. *J Clin Oncol.* 2020;38(15_suppl):2551-2551. doi:10.1200/JCO.2020.38.15_suppl.2551
53. Kessler AF, Salvador E, Domröse D, et al. Blood Brain Barrier (BBB) Integrity Is Affected By Tumor Treating Fields (TTFields) in Vitro and In Vivo. *Int J Radiat Oncol.* 2019;105(1):S162-S163. doi:10.1016/j.ijrobp.2019.06.182
54. Salvador E, Kessler AF, Domröse D, et al. Tumor Treating Fields (TTFields) Reversibly Permeabilize the Blood–Brain Barrier In Vitro and In Vivo. *Biomolecules.* 2022;12(10):1348. doi:10.3390/biom12101348
55. Stupp R, Taillibert S, Kanner A, et al. Effect of Tumor-Treating Fields Plus Maintenance Temozolomide vs Maintenance Temozolomide Alone on Survival in Patients With Glioblastoma. *JAMA.* 2017;318(23):2306. doi:10.1001/jama.2017.18718

Appendix C – Supplemental Materials for Chapter 2

Animations of electric fields referenced in chapter 2 can be viewed at the following URL under Supporting Information:

<https://aapm.onlinelibrary.wiley.com/doi/10.1002/mp.14496>

To show that our objective function is not convex, we will present a counter example to the definition of convexity¹. For all points in the domain $(\vec{x}, \vec{y}) \in \mathbb{R}^n$ and all $\lambda \in [0,1]$:

$$F(\lambda\vec{x} + (1 - \lambda)\vec{y}) \leq \lambda F(\vec{x}) + (1 - \lambda)F(\vec{y}). \quad (\text{B.1})$$

Using a random sample of parameters within the bounds of the problem, two parameter arrays can be tested to see if the inequality is satisfied. For continuous functions, it is sufficient to use $\lambda = 0.5$ to check if parameters satisfy the inequality¹.

We must first address the uncertainty in our objective function, which comes from the mesh grid discretization of the electric field. Small variations in the location of electrodes can result in uncertainty in the objective function. To overcome this uncertainty, random location variables (r, θ) are incremented every 0.5 mm for r and every $\pi/8$ degrees for θ . Our model also contains both phase shift and geometric symmetries that we must address in order to find a true counter example. Firstly, for any geometry and number of electrodes, with variable phase shifts relative to electrode 1 ($\varphi_1 = 0$), symmetry dictates that: $F(\varphi_2, \varphi_3, \dots, \varphi_n) = F(2\pi - \varphi_2, 2\pi - \varphi_3, \dots, 2\pi - \varphi_n)$. Next, since one electrode is held at a constant $\theta_1 = 0$, and we are dealing with a spherical tumour model, there is a symmetry along the x axis (perpendicular to the electrode insertion direction). Therefore, $F(\theta_2, \theta_3, \dots, \theta_n) = F(2\pi - \theta_2, 2\pi - \theta_3, \dots, 2\pi - \theta_n)$.

Both phase and location symmetries result in 4 symmetric regions, where $\theta_R = 2\pi - \theta$ and $\varphi_R = 2\pi - \varphi$:

Region 1. θ, φ

Region 2. θ_R, φ

Region 3. θ, φ_R

Region 4. θ_R, φ_R

All 4 of these configurations will result in the same objective value for any number of electrodes/contacts. If the pair of parameter points being tested by the inequality are in different symmetry regions, a false non-convex determination could be made. Since the region a parameter set belongs to is unknown, we will transform one parameter set to check the other 3 regions until both points are in the same region. With the restriction in place of removing symmetric solutions, if (B.1) is not satisfied by a pair of parameter points, then we have shown that the objective function is not convex.

An algorithm to test (B.1) was created, which starts by finding 50 random pairs of parameter points. The inequality is checked for the first pair of parameter sets. If (B.1) is not satisfied, all θ values in point 2 are changed to θ_R to check symmetric region 2. If the inequality is still not satisfied, all φ values in point 2 are changed to φ_R (with initial θ 's) to check symmetric region 3. If it is still not satisfied, both θ and φ are converted to θ_R and φ_R to check region 4. If the inequality is still not satisfied after all 4 symmetric regions have been checked, then the function is not convex.

For a 3-electrode single contact model with fixed location, the algorithm was tested for φ_2, φ_3 phase shift variables. It can be shown that the objective function for these parameters is convex. However, we will now show that the 3-electrode single contact model with variable location and phase is not convex. Running the algorithm for a 3 electrode, single contact model with variable location and variable phase, a counter example was found after 12 iterations. For the following variables ($\varphi_2, \varphi_3, r_1, r_2, r_3, \theta_2, \theta_3$), the objective function is not convex.

2.95, 3.36, 5.5 mm, 10.5 mm, 11 mm, 3.53, 0.39

5.65, 3.11, 9.5 mm, 8.5 mm, 11.5 mm, 5.50, 2.36

The objective was also tested for convexity for a 4 electrode, single contact model with fixed location. After 3 iterations a counter example was found for phase shift parameters

$(\varphi_2, \varphi_3, \varphi_4)$ of (4.08, 0.38, 3.37) radians and (3.89, 6.07, 1.98) radians. Lastly the objective was tested for the 3-electrode dual contact model, with fixed location. A counter example for the phase parameters $(\varphi_2, \varphi_3, \varphi_4, \varphi_5, \varphi_6)$ was found after 7 iterations to be (4.05, 4.22, 0.08, 6.26, 2.39) radians and (4.20, 5.21, 2.10, 4.36, 5.54) radians respectively.

By finding counter examples to the definition of convexity, we are able to show that our objective function is not convex for full location and phase optimizations, phase (and location) optimizations of more than 3 electrodes, and phase (and location) optimizations of multi-contact electrode models.

1. Boyd SP, Vandenberghe L. *Convex Optimization*. Cambridge University Press. 2004.

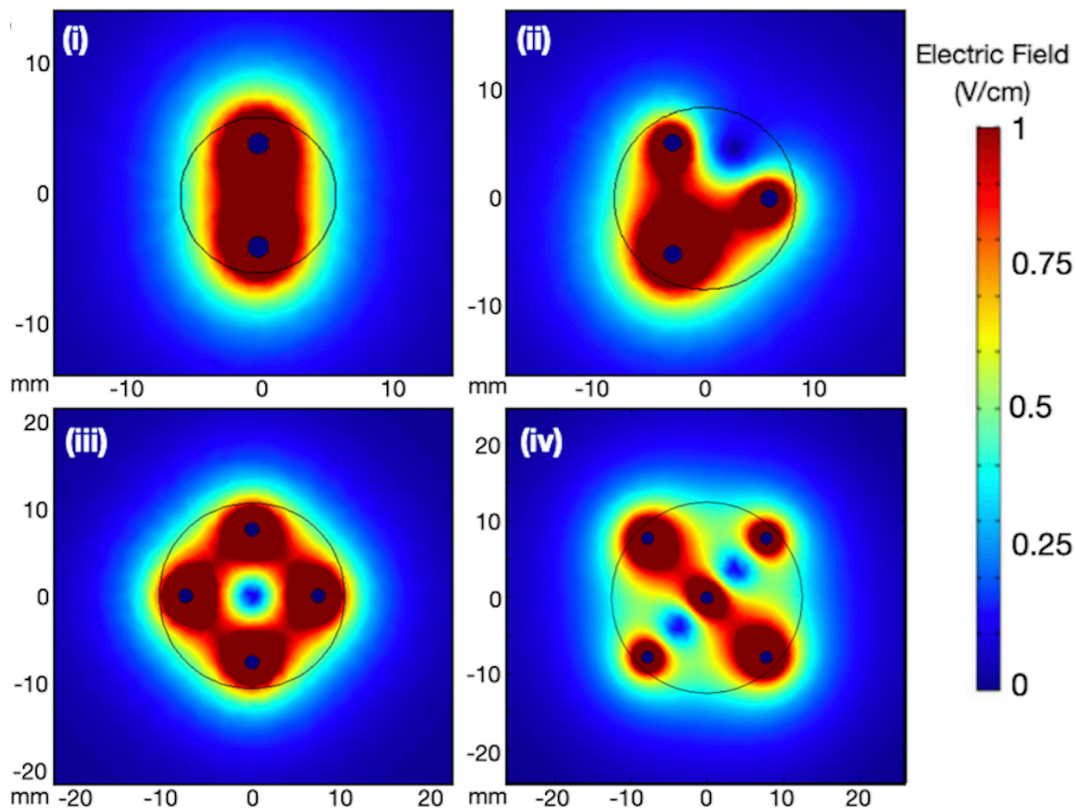


Figure C.1: Average temporal electric field maps for optimized 2-5 electrodes configurations with no phase shifting.

Appendix D – Supplemental Materials for Chapter 3

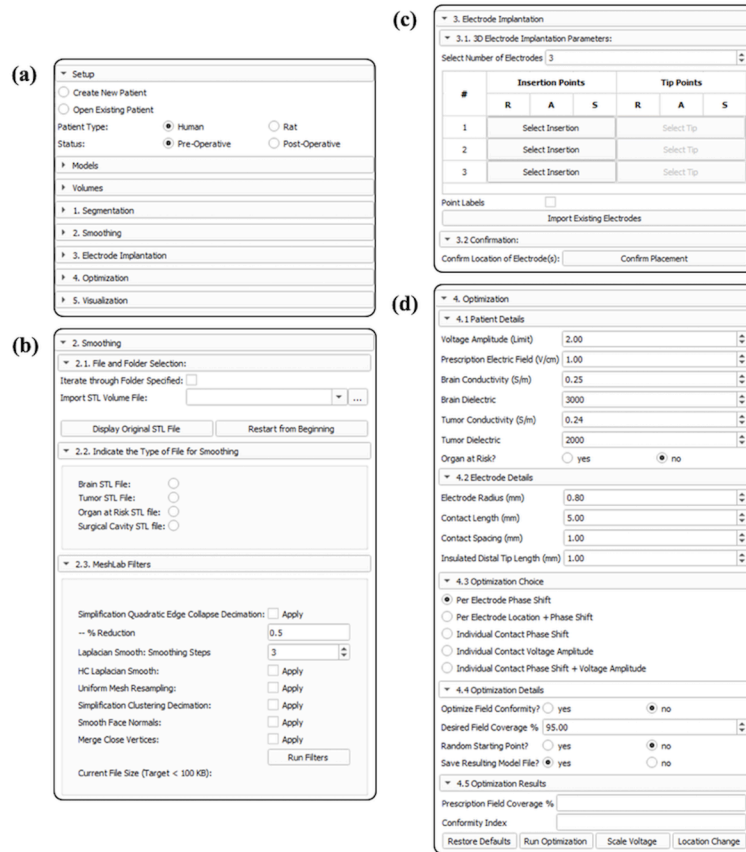


Figure D.1: Custom IMT Slicelet design including (a) the numbered pipeline, (b) the smoothing module, (c) the electrode implantation module, and (d) the optimization module.

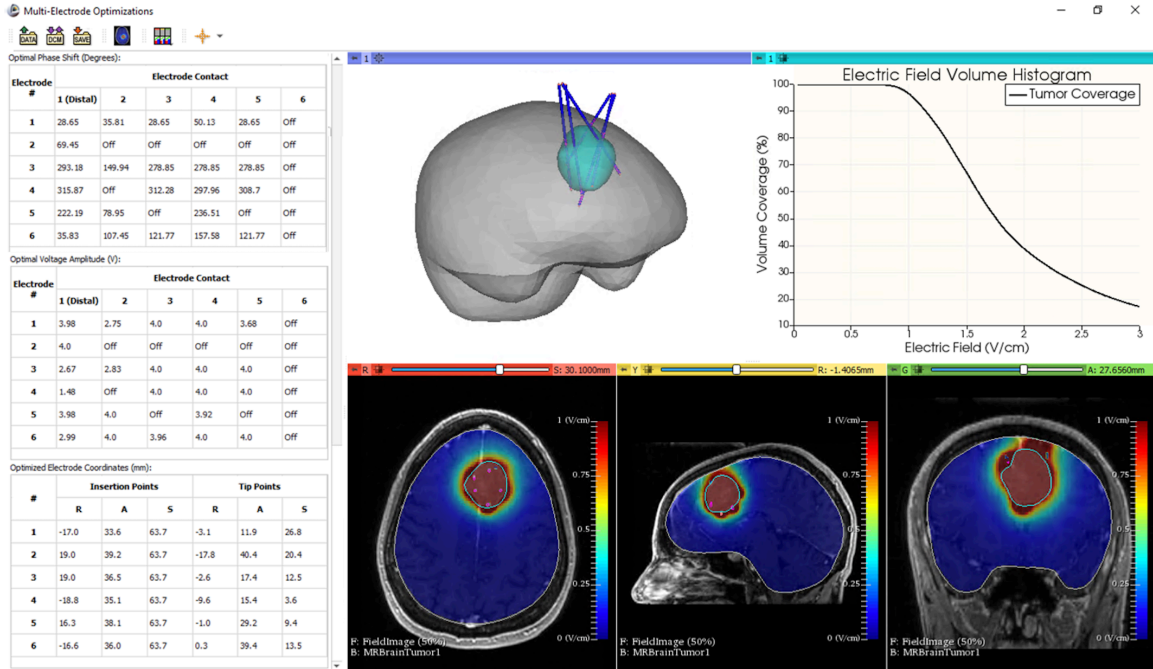


Figure D.2: Treatment planning system full visualization layout of optimized plan results for the human dual entry model including phase shift and voltage amplitude programming, electrode insertion and tip coordinates, the interactive 3D brain, tumour, and electrode models, the EVH, and the axial, sagittal and coronal interactive slice views of the electric field on the MRI.

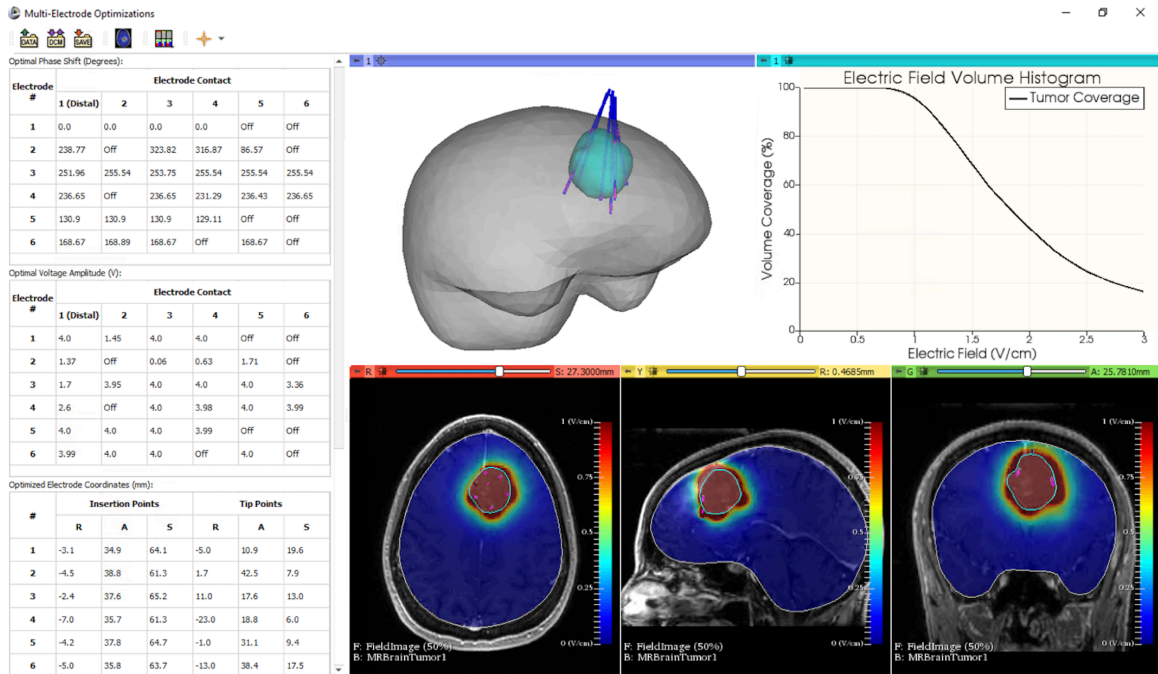


Figure D.3: Treatment planning system full visualization layout of optimized plan results for the human single entry model including phase shift and voltage amplitude programming, electrode insertion and tip coordinates, the interactive 3D brain, tumor, and electrode models, the EVH, and the axial, sagittal and coronal interactive slice views of the electric field on the MRI.

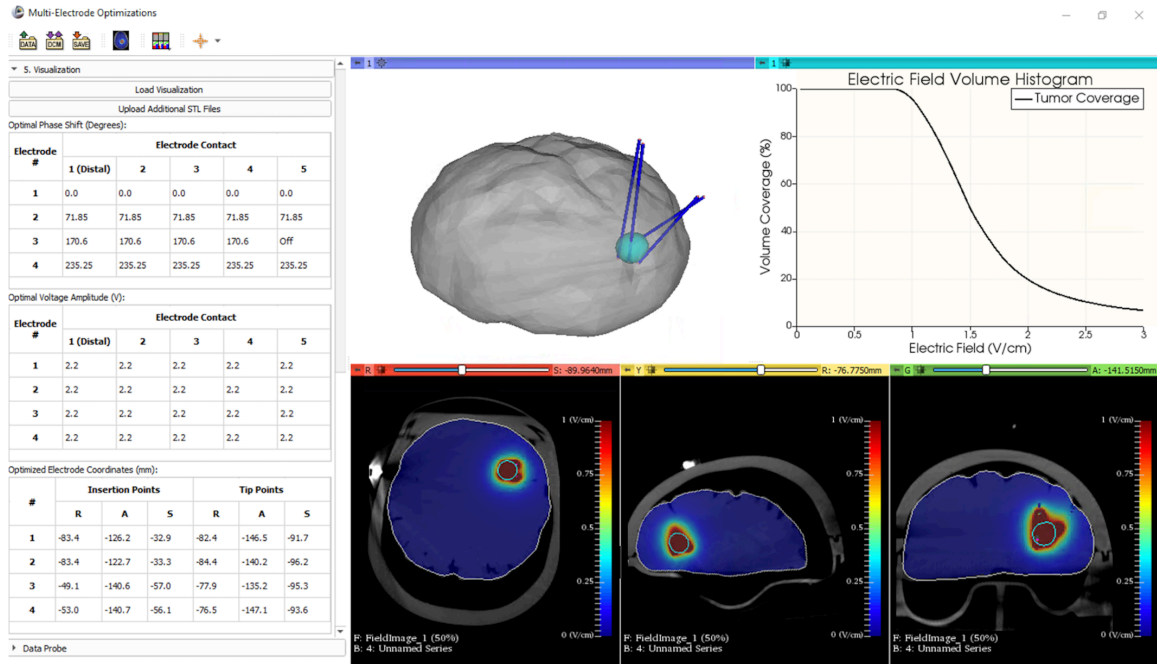
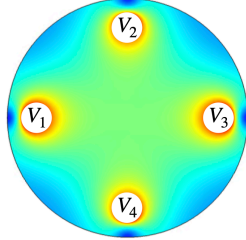
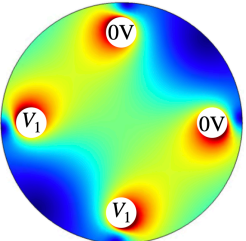
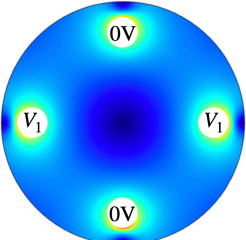


Figure D.4: Treatment planning system full visualization layout of optimized plan results for the phantom CT dual entry model including phase shift and voltage amplitude programming, electrode insertion and tip coordinates, the interactive 3D brain, tumour, and electrode models, the EVH, and the axial, sagittal and coronal interactive slice views of the electric field on the MRI.

Appendix E – Supplemental Materials for Chapter 4

Animation of figure 4.3 can be viewed at the following URL under Supplementary data:

Figure S3: <https://iopscience.iop.org/article/10.1088/1361-6560/acc308>

Field Map	Voltage Amplitude (V)	Current (mA)	Impedance (Ω)	Average Power (mW)	System Power (mW)
	1.06	9.41	113	4.99	20.0
	2.30	10.21	225	11.74	23.5
	1.06 (1.86)	6.19 (10.86)	171 (171)	3.28 (10.0)	6.56 (20.0)

Current I_n is computed using the Admittance Matrix Y below from $\mathbf{I} = \mathbf{YV}$. Admittance is the inverse of the impedance Z ($Y = Z^{-1}$), with quantities y_{nm} the admittance between voltage sources n and m . y_n is the admittance between the voltage source n and the external ground source: in this case this resistance is infinite and hence the admittance $y_n = 0$.

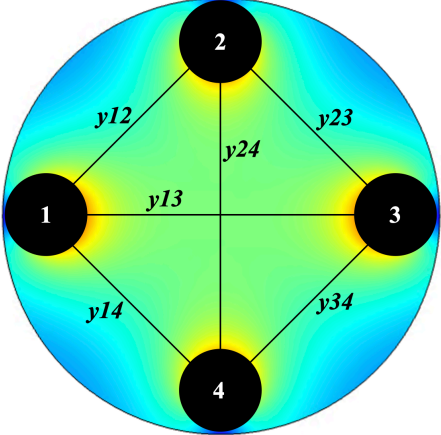
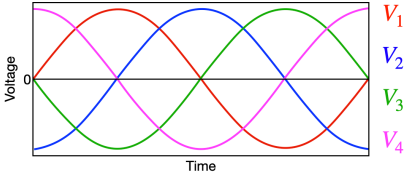
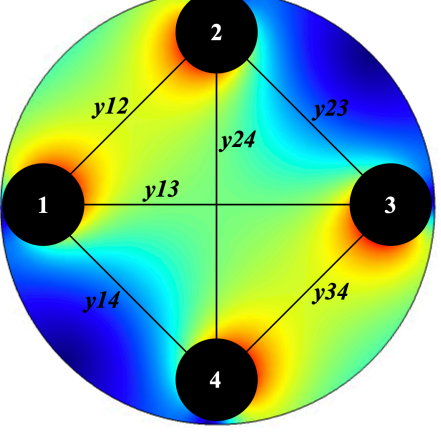
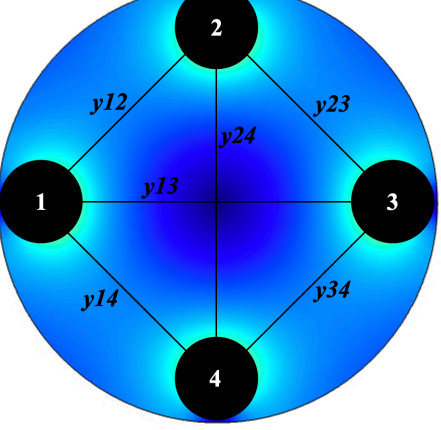
$$\begin{bmatrix} I_1 \\ I_2 \\ I_3 \\ I_4 \end{bmatrix} = \begin{bmatrix} y_1 + y_{12} + y_{13} + y_{14} & -y_{12} & -y_{13} & -y_{14} \\ -y_{12} & y_2 + y_{12} + y_{23} + y_{24} & -y_{23} & -y_{24} \\ -y_{13} & -y_{23} & y_3 + y_{13} + y_{23} + y_{34} & -y_{34} \\ -y_{14} & -y_{24} & -y_{34} & y_4 + y_{14} + y_{24} + y_{34} \end{bmatrix} \begin{bmatrix} V_1 \\ V_2 \\ V_3 \\ V_4 \end{bmatrix}$$

Due to the geometrical symmetry of the electrodes, $y_{12} = y_{14} = y_{23} = y_{34}$ and $y_{13} = y_{24}$. The admittance matrix computed in COMSOL for the 4-electrode geometry yielded $y_{12} = 0.00292$ S and $y_{13} = 0.00152$ S. For electrode 1, the current is therefore:

$$I_1 = V_1(2y_{12} + y_{13}) - V_2(y_{12}) - V_3(y_{13}) - V_4(y_{12})$$

The average power is calculated from $P_{avg} = 0.5VI$.

Specific Solutions

	<p>For the optimized rotating case: $V_1 = -V_3 = 1.06 \text{ V}$ and $V_2 = -V_4 = 1.06 \text{ V}$</p>  $I_1 = V_1(2y_{12} + y_{13}) - V_2(y_{12}) - (-V_1)(y_{13}) - (-V_2)(y_{12})$ $I_1 = V_1(2(y_{12} + y_{13}))$ $I_1 = \mathbf{0.00941 \text{ A}}$ $Z_1 = [2(y_{12} + y_{13})]^{-1}$ $Z_1 = \mathbf{113 \Omega}$
	<p>For the optimized non-rotating case: $V_1 = V_4 = 2.30 \text{ V}$ and $V_2 = V_3 = 0 \text{ V}$</p> $I_1 = V_1(2y_{12} + y_{13}) - V_1(y_{12})$ $I_1 = V_1(y_{12} + y_{13})$ $I_1 = \mathbf{0.01021 \text{ A}}$ $Z_1 = [y_{12} + y_{13}]^{-1}$ $Z_1 = \mathbf{225 \Omega}$
	<p>For the destructive interference case: $V_1 = V_3 = 1.06 \text{ V}$ and $V_2 = V_4 = 0 \text{ V}$</p> $I_1 = V_1(y_{12} + y_{13} + y_{12}) - V_1(y_{13})$ $I_1 = V_1(2y_{12})$ $I_1 = \mathbf{0.00619 \text{ A}}$ $Z_1 = [2y_{12}]^{-1}$ $Z_1 = \mathbf{171 \Omega}$

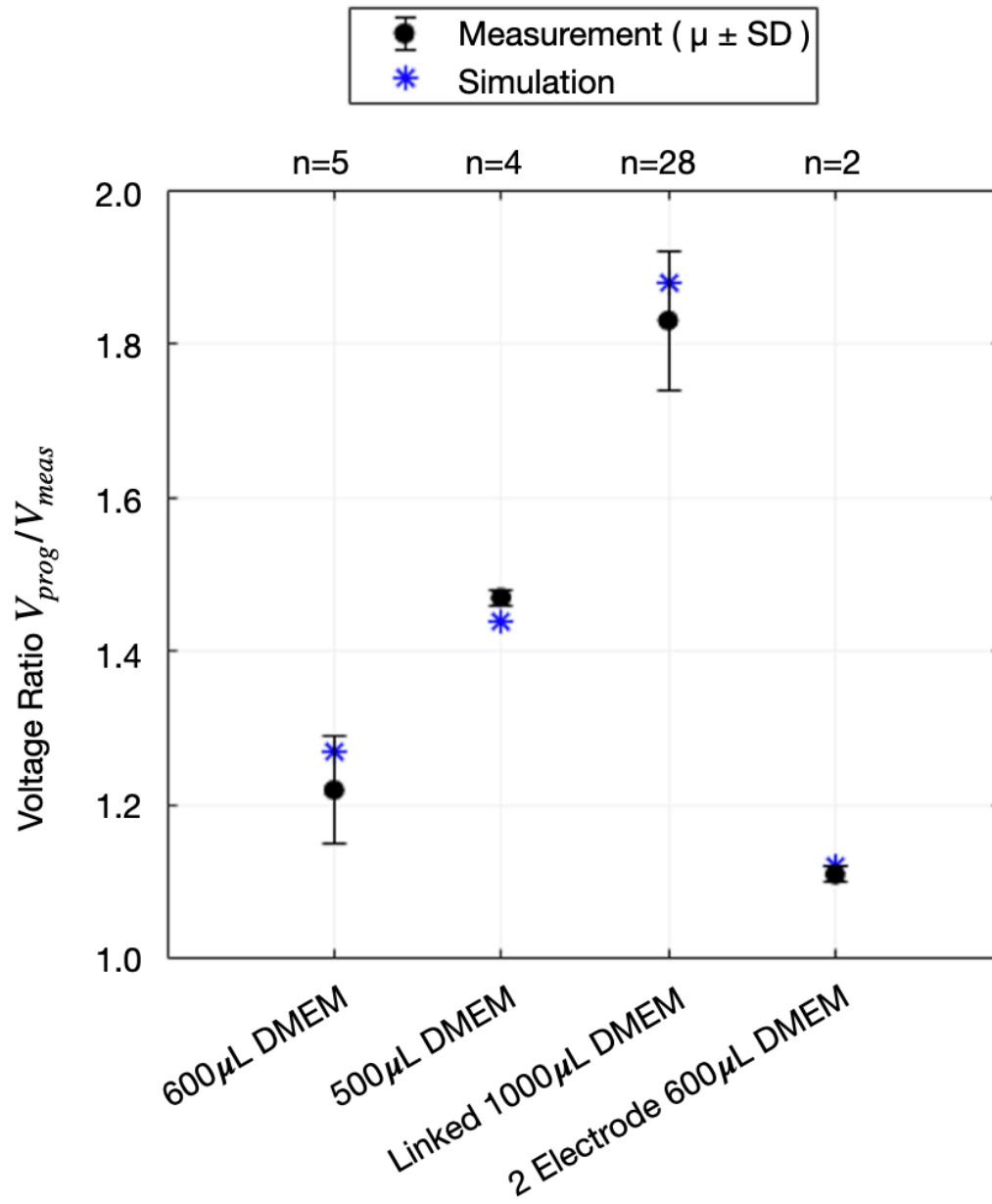


Figure E.1: Ratio of programmed to measured voltage for 24-well, 4 electrode *in vitro* scenarios including different volumes of DMEM, two wells linked together, and two stimulating electrodes.

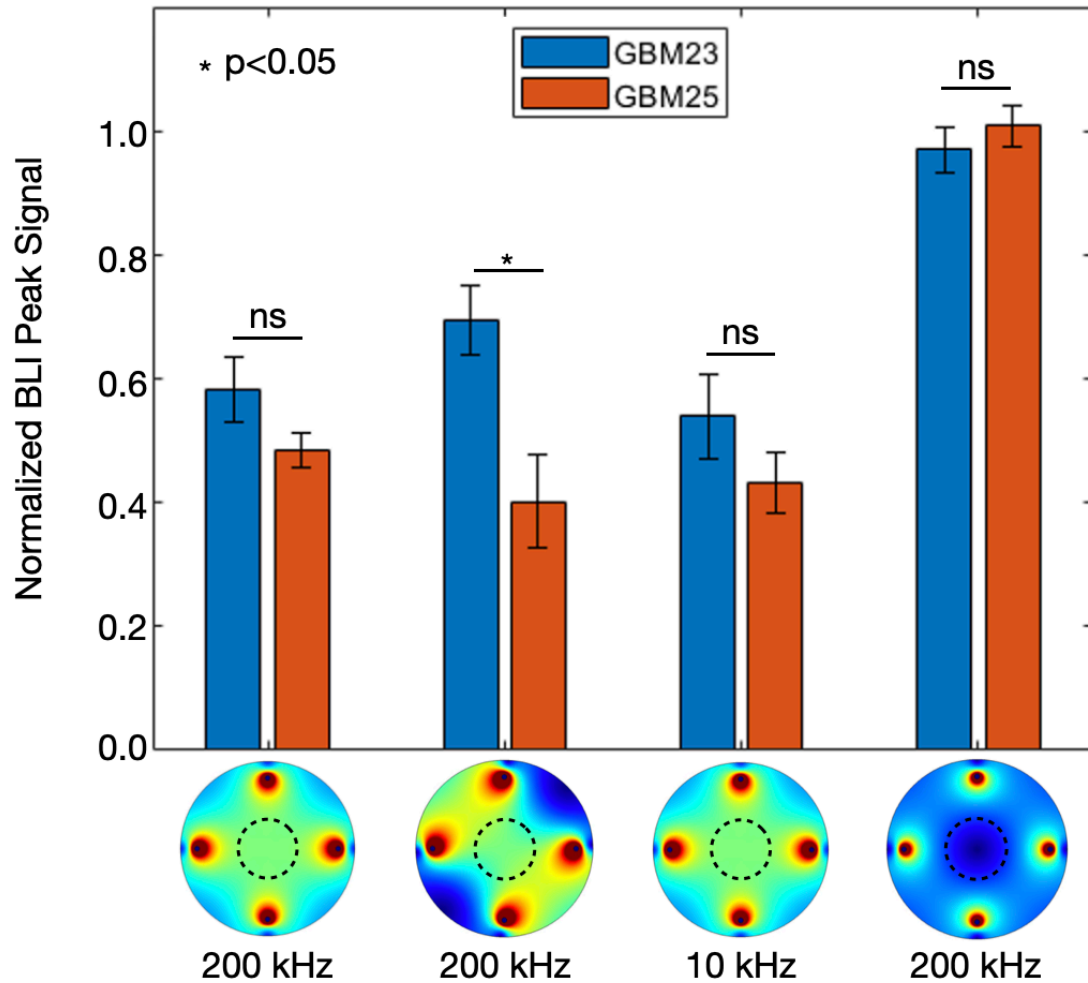


Figure E.2: Cell viability comparison between patient derived cell line GBM 23 and GBM 25. Mean of the BLI peak signal normalized to sham \pm standard error, for the cases of constructive interference 200 kHz rotating fields (0.58 ± 0.05 , $n=6$ vs. 0.48 ± 0.03 , $n=6$), 200 kHz non-rotating (0.69 ± 0.06 , $n=6$ vs. 0.40 ± 0.07 , $n=6$), and 10 kHz rotating fields (0.54 ± 0.07 , $n=6$ vs. 0.43 ± 0.05 , $n=6$), and destructive interference 200 kHz voltage matched non-rotating fields (0.97 ± 0.04 , $n=6$ vs. 1.01 ± 0.03 , $n=6$).

Appendix F – IMT Planning System (IMTPS) User Guide

IMT Planning System (IMTPS) User Guide

Erin Iredale
Updated January 2023

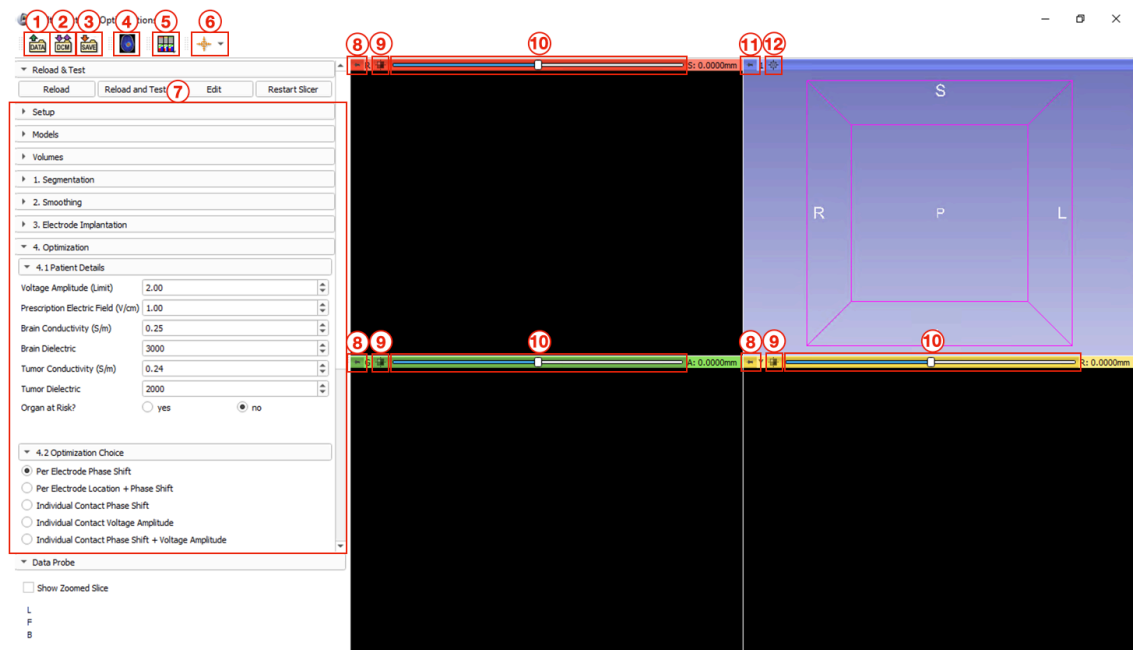
Table of Contents

Navigating IMTPS & 3D Slicer User Interface.....	2
Patient Setup Module	4
Models Module: Adjusting 3D Model	5
Volumes Module: Adjusting DICOM Window Levels.....	6
Segmentation Module.....	7
Smoothing Module	10
Electrode Implantation Module.....	11
Optimization Module.....	12
Visualization Module	14

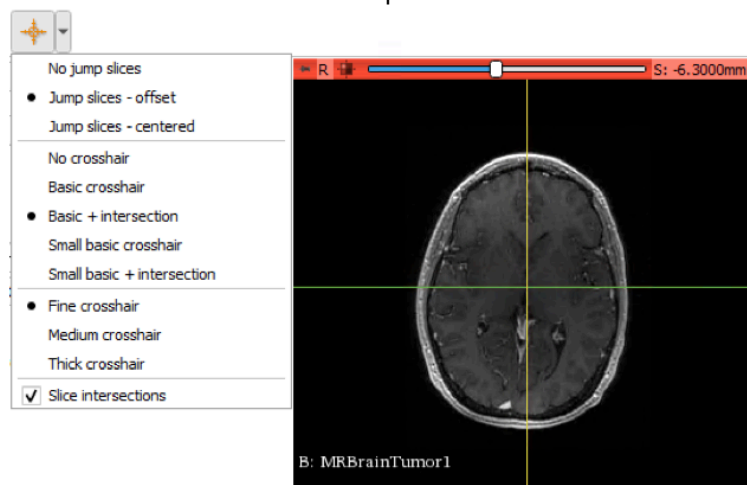
Preface

The suggested default pipeline is to begin in the setup module to select the patient folder, patient type, and import the DICOM image. Next, segment the brain and tumor (and any organs at risk to avoid placing electrodes in, and surgical resection cavity) in the segmentation module. Next, smooth the segmentations in the smoothing module, and choose electrode trajectories in the electrode implantation module. Next, use the optimization module and begin with a per electrode phase shift optimization (+location if necessary), followed by a voltage scaling if desired coverage not reached, followed by an individual contact phase shift optimization (and lastly individual contact phase shift + voltage amplitude conformity index optimization in order to minimize the input voltage). Lastly, view the results in the visualization module.

Navigating IMTPS & 3D Slicer User Interface



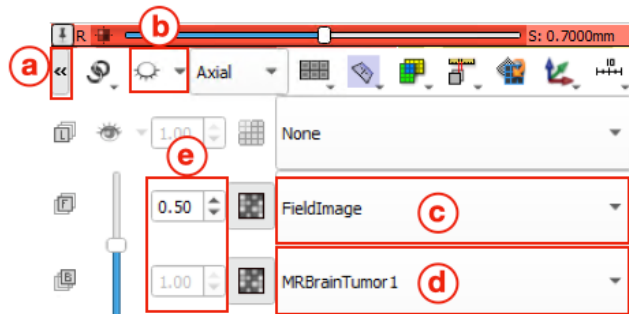
1. Upload additional data files
2. Upload DICOM image
3. Save models, volumes, scene views, etc.
4. Return to IMTPS interface
5. Change display layout (3D model, slice view orientation)
6. Enable crosshairs on slice and 3D views. Example of crosshairs on axial slice:



7. IMTPS module navigation (individual module guides starting on page 4)

8. Additional settings for cross sectional views (red: axial, green: coronal, yellow: sagittal)

- a.** Expand/collapse more settings
- b.** Toggle slice visibility in 3D view
- c.** Foreground image volume (electric field map)
- d.** Background image volume (patient MR, CT, etc.)
- e.** Change opacity of selected image volume

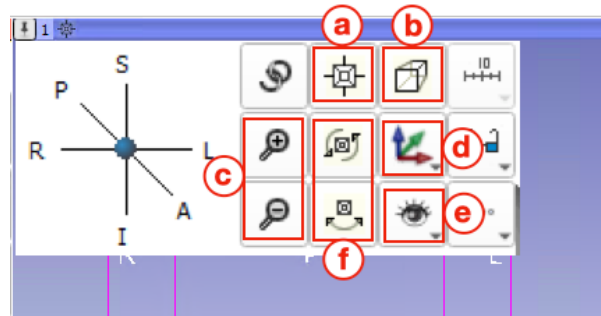


9. Centre slice view

10. Scroll through image slices

11. Additional settings for 3D view

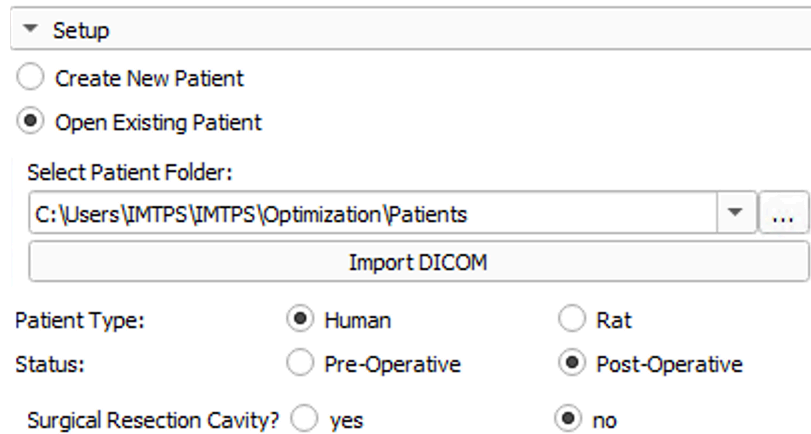
- a.** Centre 3D view
- b.** Toggle between orthographic and perspective rendering in the 3D view
- c.** Zoom in and out
- d.** Add directional label to view
- e.** Edit visibility of box, axis labels, and background colour
- f.** Spin and rock animations of 3D view



12. Centre 3D view

Patient Setup Module

The setup module is a custom module used to choose the patient folder (either create new patient or open existing patient), import patient DICOM images previously loaded to 3D Slicer (MRI, CT, etc), and choose patient type (human or rat) and operative status (pre-operative or post-operative). The selection of post-operative includes an additional selection of surgical resection cavity presence.



▼ Setup

Create New Patient

Open Existing Patient

Select Patient Folder:


C:\Users\IMTPS\IMTPS\Optimization\Patients

Import DICOM

Patient Type: Human Rat

Status: Pre-Operative Post-Operative

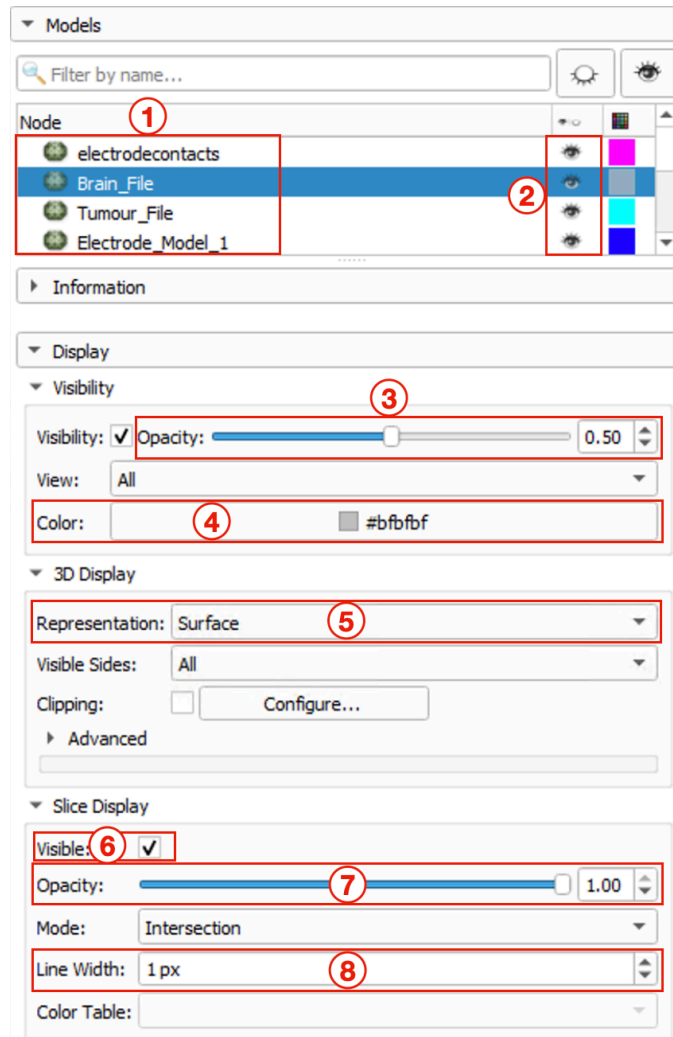
Surgical Resection Cavity? yes no

If patient DICOM has not yet been loaded to 3D Slicer before, use upload DICOM image button in the top toolbar() to select from files. Once that DICOM has been loaded to slicer once, it will remain in the DICOM database and can be accessed quickly by the Import DICOM button in the setup module.

Models Module: Adjusting 3D Model

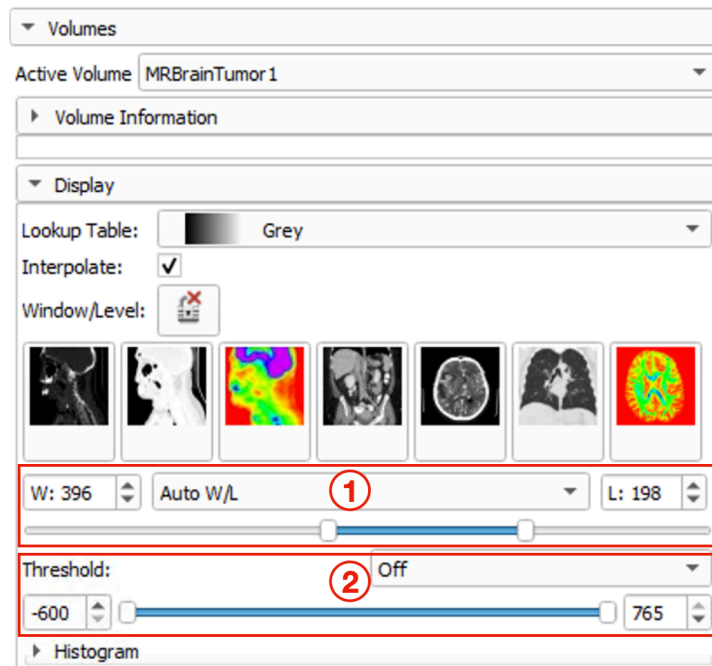
The 3D Slicer models module is used for adjusting the visualization of the 3D models after a treatment has been planned.

1. Name of model
2. Toggle visibility of selected model
3. Change the opacity of the selected model in the 3D view
4. Change the colour of the selected model
5. Change how the 3D model is displayed (surface rendering, mesh points, wireframe, or surface with wireframe)
6. Toggle visibility of model outline in the slice views
7. Change the opacity of the model border intersection in the slice views
8. Change the line width of the model border intersection in the slice views.



Volumes Module: Adjusting DICOM Window Levels

The 3D Slicer volumes module is used to adjust the display of the DICOM image.

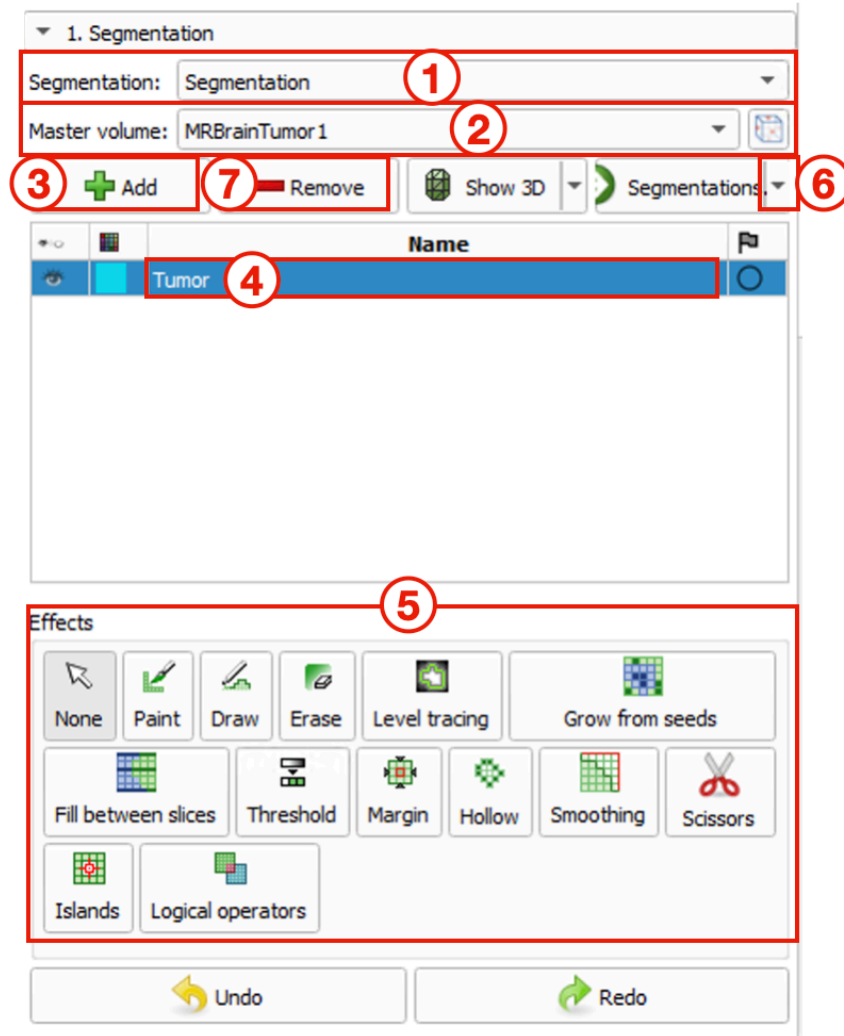


1. Adjust the Window/Level values of the image. Window represents the range of voxel values, Level represents the midpoint of voxel values.

2. Adjust the threshold of voxel intensity.

Segmentation Module

The 3D Slicer segmentation module is used to segment the brain, tumor and OAR or Cavity volumes if applicable. To start a segmentation:

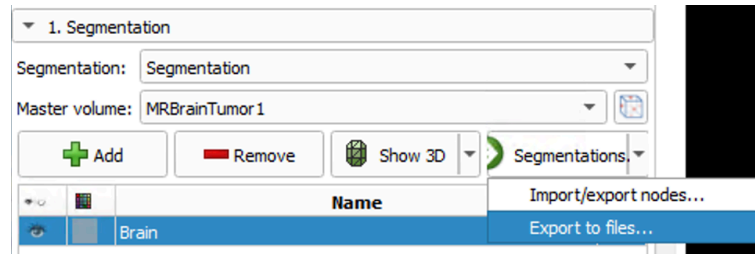


1. Use the dropdown to select Create new Segmentation
2. Use the dropdown to select the DICOM volume you will be using to segment
3. Add segmentation

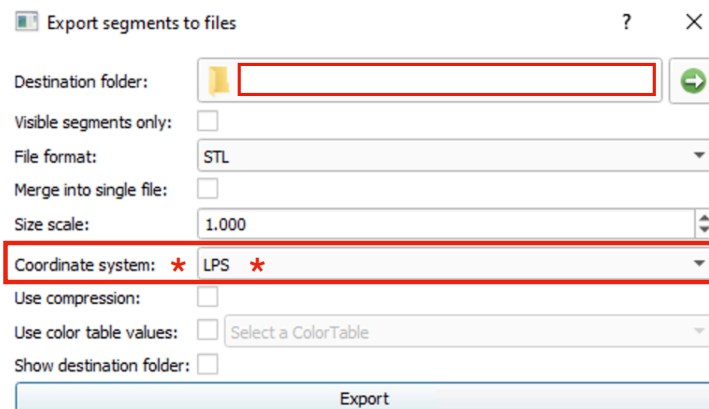
4. Rename segmentation appropriately

5. Use the effects to segment the volume on the DICOM image on the right (explanation for each effect below). Segmentation can be done on any slice (coronal, sagittal, axial)

6. When finished with the first segmentation, use the dropdown and click Export to files...



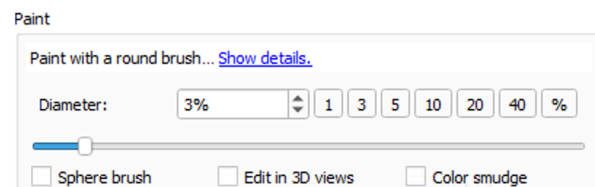
In the popup, choose the destination folder as that patient's folder by clicking the file path and navigating to the appropriate path. Ensure **LPS** coordinate system is selected. Click Export.



7. Remove the segmentation just completed, and repeat the process for the next segmentation. Note: Do not add more than one segmentation to the model at once, the completed segmentation must be removed first.

Effects

Paint: Use this tool to paint on the slice with a round brush at specified diameter. The selection of sphere brush will mask multiple slices simultaneously.

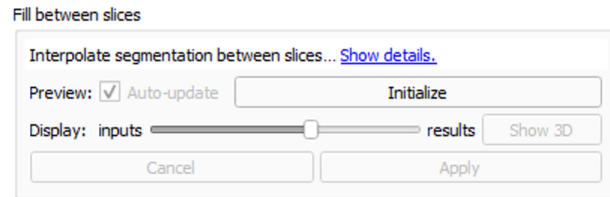


Draw: This tool is used to trace the outline of the volume on a slice, and then press enter to fill the outline.

Erase: This tool works the same as paint, but erases the mask instead.

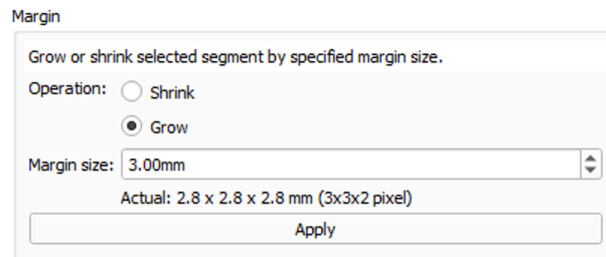
Level tracing: When this tool is selected and hovered over the slice, a border is created at the voxel intensity you are hovering over.

Fill between slices: This is a useful tool to interpolate the segmentation in between slices already segmented. First click Initialize to preview, then click Apply.



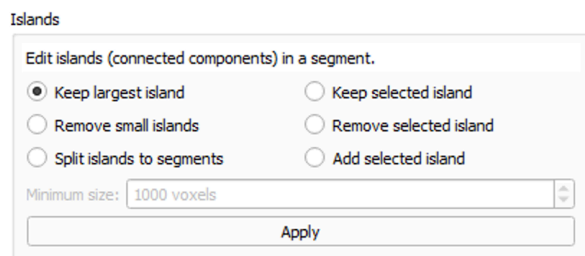
Threshold: For segmenting voxels in a certain threshold range.

Margin: To add margins a segmentation use this tool. For example, if a surgical resection cavity is segmented, use the grow feature to create a margin to treat with the electric field. This is also useful for creating margins around the visible tumor volume to cover microscopic disease.



Smoothing: This provides a necessary initial boundary smoothing of the volume prior to the smoothing module.

Islands: This is used (specifically keep largest island) to ensure no stray unconnected voxels are present in the segmentation.



Smoothing Module

With initial segmentations now complete, the custom smoothing module is used to prepare these volumes for the optimization module.

1. Click ... to select the segmentation file to import for smoothing.

2. Click to display the file in the 3D view and slice views.

3. Use this button if you need to start the smoothing process over again.

4. Select the type of segmentation file you are smoothing. This is required for naming the smoothed file.

5. Smoothing filters that can be applied to the volume.

Simplification Quadratic Edge Collapse Decimation reduces the number of vertices in the mesh by the reduction factor below (0.9 is more subtle, 0.5 more extreme). **Laplacian Smooth** will smooth the mesh with the number of iterations specified. **HC Laplacian Smooth** is another smoothing option (in addition to **Smooth Face Normals**). **Uniform Mesh Resampling** will change the current mesh into a more uniform distribution of vertices (use with caution). **Simplification Clustering Decimation** is another simplification method, and **Merge Close Vertices** will combine vertices that are close together into a single vertex.

6. Click Run Filters to apply the selected filters. This is an iterative process where different filters and combinations of filters can be applied, so repeat step 5 and 6 until the target file size is reached.

7. The file size after the filters were applied is displayed here, with the target of reducing the file size to under 100 KB. Example: Current File Size (Target < 100 KB): 74 KB

The screenshot shows the '2. Smoothing' module interface. It is divided into three main sections:

- 2.1. File and Folder Selection:** Contains an 'Iterate through Folder Specified:' checkbox, an 'Import STL Volume File:' input field with a dropdown arrow and a '...' button (callout 1), a 'Display Original STL File' button (callout 2), and a 'Restart from Beginning' button (callout 3).
- 2.2. Indicate the Type of File for Smoothing:** Contains four radio button options: 'Brain STL File:', 'Tumor STL File:', 'Organ at Risk STL file:', and 'Surgical Cavity STL file:' (callout 4).
- 2.3. MeshLab Filters:** Contains a list of filters with checkboxes and 'Apply' buttons: 'Simplification Quadratic Edge Collapse Decimation:' (with a '% Reduction' input field set to 0.5), 'Laplacian Smooth: Smoothing Steps' (with a dropdown set to 3), 'HC Laplacian Smooth:', 'Uniform Mesh Resampling:', 'Simplification Clustering Decimation:', 'Smooth Face Normals:', and 'Merge Close Vertices:'. A 'Run Filters' button (callout 6) is at the bottom right of this section. Below the filters is a 'Current File Size (Target < 100 KB):' input field showing '74 KB' (callout 7).

Electrode Implantation Module

This custom module allows users to plan the fixed electrode trajectories or variable tip trajectories that will be used as starting points for the tip location optimization.

3. Electrode Implantation

3.1. 3D Electrode Implantation Parameters:

Select Number of Electrodes 2

#	Insertion Points			Tip Points		
	R	A	S	R	A	S
1	-0.469	71.189	49.033	Select Tip		
2	Select Insertion			Select Tip		

Point Labels

4 Import Existing Electrodes

3.2 Confirmation:

Confirm Location of Electrode(s): Confirm Placement 5

Check Geometry Status Test Go or No-Go for Optimization 6

Build Status

1. Choose the number of electrodes

2. Click buttons for Select Insertion and Select Tip and choose the appropriate location on the images slices. Points can be moved after initial placement. For surgical resection cavity option, the selection points are changed to Centre Points and Trajectory points, where the centre of each array element is selected along with the direction of the element. Preclinical rat model pre-operative option only requires the insertion point of the apparatus to be selected.

3. Selection of insertion point 1 on the sagittal slice of the MR image (click to place). The point can be moved after initial placement by dragging the point.

4. Use this if electrodes have already been planned.

5. Click to confirm the placement of all electrodes.

6. Click to test if brain, tumor, and electrode geometries build successfully. If Go is displayed, optimization can be started. If No-Go is displayed, re-smoothing and/or electrode implantation coordinate adjustment may be required.

Optimization Module

In the custom optimization module, the programming and electrode tip coordinates can be optimized. Default values are provided for all necessary selections.

4. Optimization

4.1 Patient Details

1 Voltage Amplitude (Limit)

2 Prescription Electric Field (V/cm)

3 Brain Conductivity (S/m)

3 Brain Dielectric

3 Tumor Conductivity (S/m)

3 Tumor Dielectric

4 Organ at Risk? yes no

4.2 Electrode Details

5 Electrode Radius (mm)

5 Contact Length (mm)

5 Contact Spacing (mm)

5 Insulated Distal Tip Length (mm)

4.3 Optimization Choice

6 Per Electrode Phase Shift

Per Electrode Location + Phase Shift

Individual Contact Phase Shift

Individual Contact Voltage Amplitude

Individual Contact Phase Shift + Voltage Amplitude

4.4 Optimization Details

7 Optimize Field Conformity? yes no

8 Desired Field Coverage %

9 Random Starting Point? yes no

9 Save Resulting Model File? yes no

4.5 Optimization Results

10 Prescription Field Coverage %

10 Conformity Index

Restore Defaults

Run Optimization 11

Scale Voltage 12

Location Change 13

1. Select the fixed voltage amplitude of waveforms, or the voltage limit for optimizations involving the voltage.

2. Select the prescription electric field magnitude.

3. Define the electrical properties of the brain and tumor tissues if different than the default. If surgical resection cavity was selected, the electrical properties must be defined as well.

Cavity Conductivity (S/m)	1.00
Cavity Dielectric	100

4. Select if organ at risk is present. If yes is selected, an OAR weighting factor and electrical properties must be defined.

OAR Weighting Factor	0.10
OAR Conductivity (S/m)	0.25
OAR Dielectric	3000

5. Customize cylindrical electrode sizing specifications including electrode radius, length of a single active contact, spacing between contacts, and the length of the insulated distal electrode tip.

6. Select the type of optimization. **Per Electrode Phase Shift** will consider all contacts on the same electrode to have equal phase shift, and optimize the relative phase shifts of each electrode (this type is a good starting point). **Per Electrode Location + Phase Shift** adds the electrode tip coordinates as optimization parameters (this type is lengthy, will take ~ 5 hrs). **Individual Contact Phase Shift** will optimize each contacts' phase shift (this type is a good second step after the per electrode options). **Individual Contact Voltage Amplitude** will optimize each contacts' voltage amplitude (this type is for conformity index optimization only). **Individual Contact Phase Shift + Voltage Amplitude** will optimize both phase shift and voltage (this type is good for a final conformity index optimization).

7. Select if electric field conformity is to be optimized (to create electric fields shaped around tumor, minimizing the field outside the tumor)

8. Define the field coverage percent.

9. Select if a random starting point should be used for optimization (not recommended), and if the COMSOL model file should be saved to the patient folder.

10. The resulting tumor percentage covered by the prescription electric field and the conformity index are displayed.

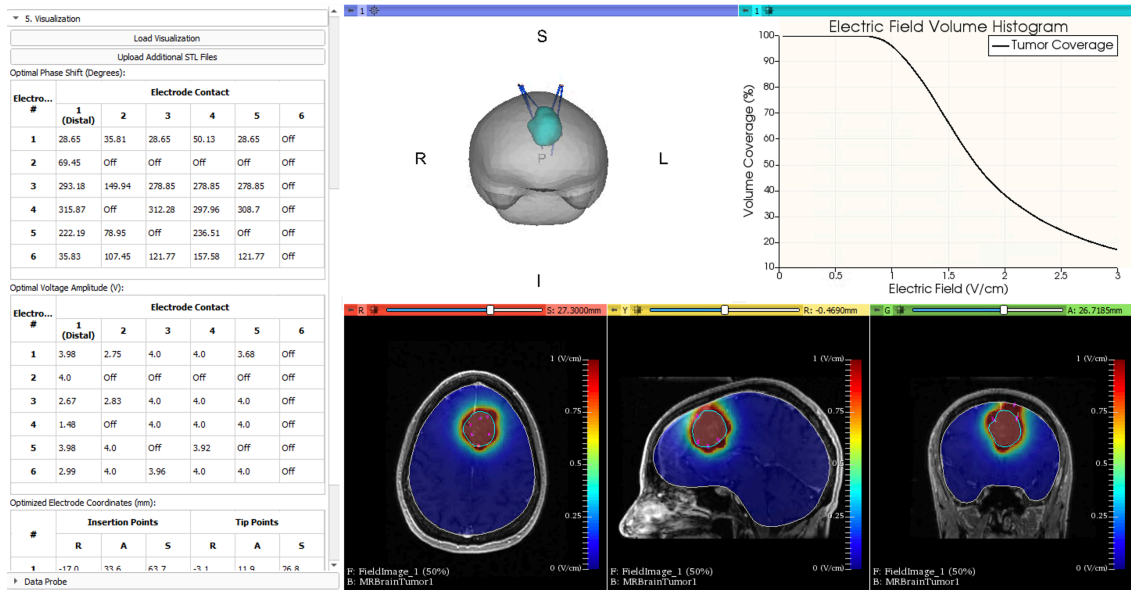
11. Click to run the optimization. While an optimization is running the IMTPS cannot be interacted with.

12. Use this button if you want to increase the tumor coverage to the desired field coverage % value stated in 7. The voltage will be adjusted accordingly and displayed.

13. Use this button if you manually changed the electrode trajectories in the implantation module and would like to see how the field has been updated with the same stimulation parameters.

Visualization Module

The custom visualization module pertains to displaying a treatment plan. The Load Visualization button will import all necessary files within the patient folder and display the plan. Views include 3D, and electric field volume histogram showing coverage, and the electric field superimposed on the image slices. The Upload Additional STL Files button can be used to add any files not imported already. The electrode programming (phase shift and voltage) for each electrode contact and the coordinates of each are displayed in this module.



Curriculum Vitae

Name:	Erin Iredale
Post-secondary Education and Degrees:	Western University London, ON Ph.D. CAMPEP Medical Biophysics 09/2017 - 05/2023
	Western University London, ON B.Sc. Medical Physics and Applied Math 09/2012 - 04/2017
Honours and Awards:	NSERC Canada Graduate Scholarship – Doctoral 05/2020 - 04/2023
	Ontario Graduate Scholarship (Declined) 05/2020 - 04/2021
	NSERC Canada Graduate Scholarship – Master’s 01/2019 - 12/2019
	Western Graduate Research Scholarship 09/2017 - 12/2022
	Ontario Graduate Scholarship 09/2017 - 12/2018
	Dean’s Honor List 09/2015 - 04/2017
	Mary Louise and Dr. Peter Cameron Scholarships 09/2012 - 04/2016
	Western Scholarship of Excellence 09/2012 - 04/2013
Related Work Experience	Doctoral Research Assistant (MSc, PhD) Medical Biophysics, Western University 09/2017 - 05/2023
	Course Development Assistant Physics & Astronomy, Western University

Western Student Internship (Course Development Award)
11/2020 - 12/2020

Summer Research Assistant
Medical Biophysics, Western University
05/2017 - 08/2017

Summer Research Assistant
Physics & Astronomy, Western University
05/2016 - 08/2016

Math and Science Tutor
Grades 7-12, College, and University level
Math, Physics, Calculus, Chemistry, Biology
09/2014 - 12/2018

Publications:

Journal Articles

1. **Iredale, E.**, Elsaleh, A., Xu, H., Christiaans, P., Deweyert, A., Ronald, J., Schmid, S., Hebb, M.O., Peters, T., Wong, E. (2023) Spatiotemporally dynamic electric fields for brain cancer treatment: an in vitro investigation. *Physics in Medicine and Biology*. 68:085012.
2. **Iredale, E.**, Voigt, B., Rankin A., Kim, K.W., Chen, J.Z., Schmid, S., Hebb, M.O., Peters, T., Wong, E. (2022) Planning system for the optimization of electric field delivery using implanted electrodes for brain tumor control. *Medical Physics*. 49(9): 6055-6067.
3. **Iredale, E.**, Deweyert, A., Hoover, D., Chen, J., Schmid, S., Hebb, M.O., Peters, T., Wong, E. (2020) Optimization of implanted multi-electrode configurations and programming for non-ablative electric fields delivered using intratumoral modulation therapy. *Medical Physics*. 47(11):5441-5454.
4. Deweyert, A., **Iredale, E.**, Xu, H., Schmid, S., Wong, E., Hebb, M.O. (2019) Diffuse intrinsic pontine glioma cells are vulnerable to low intensity electric fields delivered by intratumoral modulation therapy. *Journal of Neuro-Oncology*. 143:49-56.
5. Di Sebastiano, A., Deweyert, A., Benoit, S., **Iredale, E.**, Xu, H., Oliveira, C., Wong, E., Schmid, S., Hebb, M.O. (2018) Preclinical outcomes of Intratumoral Modulation Therapy for glioblastoma. *Scientific Reports*. 8:7301.

Conference Proceedings

1. **Iredale, E.**, Kang, D., Schmid, S., Hebb, M.O., Peters, T., Wong, E. (2023) Electrode Array Design and Planning for Treatment of Brain Tumor Surgical Resection Cavity Margins with Anti-Cancer Electric Fields. *AAPM Annual Meeting & Exhibition Program*. Houston, TX, United States.

2. **Iredale, E.**, Voigt, B., Rankin A., Kim, K.W., Chen, J.Z., Schmid, S., Hebb, M.O., Peters, T., Wong, E. (2022) A Planning Environment for Intracranial Electric Field Treatment of Brain Tumors. *AAPM Annual Meeting & Exhibition Program*. Washington, DC, United States.
3. **Iredale, E.**, Elsaleh, A., Xu, H., Ronald, J., Schmid, S., Hebb, M.O., Peters, T., Wong, E. (2022) In Vitro Validation of Rotating Electric Fields for Treating Glioblastoma. *Oncology Research & Education Day Event Program*. London, ON, Canada.
4. **Iredale, E.**, Voigt, B., Rankin A., Kim, K.W., Chen, J.Z., Schmid, S., Hebb, M.O., Peters, T., Wong, E. (2022) Multi-Electrode Intracranial Electric Field Treatment for Brain Tumors: Planning System and Robot-Assisted Electrode Implantation. *2022 CNS Departmental Research Day Event Program*. London, ON, Canada.
5. **Iredale, E.**, Kim, K.W., Deweyert, A., Chen, J.Z., Schmid, S., Hebb, M.O., Peters, T., Wong, E. (2021) Multi-Electrode Treatment Planning System for Intratumoral Modulation Therapy. *Oncology Research & Education Day Event Program*. London, ON, Canada (Virtual).
6. **Iredale, E.**, Kim, K.W., Deweyert, A., Chen, J.Z., Schmid, S., Hebb, M.O., Peters, T., Wong, E. (2021) Multi-Electrode Treatment Planning System for Intratumoral Modulation Therapy. *2021 CNS Departmental Research Day Event Program*. London, ON, Canada (Virtual).
7. **Iredale, E.**, Kim, K.W., Deweyert, A., Chen, J.Z., Schmid, S., Hebb, M.O., Peters, T., Wong, E. (2021) Treatment Planning System for Multi-Electrode Intratumoral Modulation Therapy. *Robarts Research Retreat Event Program*. London, ON, Canada (Virtual).
8. Deweyert, A., **Iredale, E.**, Xu, H., Oliveira, C., Wong, E., Schmid, S., Hebb, M.O. (2021) Intratumoral Modulation Therapy reduces tumor burden in 3D patient-derived glioblastoma models. *2021 CNS Departmental Research Day Event Program*. London, ON, Canada (Virtual).
9. Deweyert, A., **Iredale, E.**, Xu, H., Wong, E., Schmid, S., Hebb, M.O. (2020) Custom 3D Brain Cancer Model to Test a Novel Anti-Cancer Electrotherapy. *The FASEB Journal*, 34: 1-1. *Experimental Biology 2020 Meeting Abstracts*. San Diego, CA, United States.
10. **Iredale, E.**, Deweyert, A., Schmid, S., Hebb, M.O., Peters, T., Wong, E. (2019) Computerized optimization of multi-electrode locations and voltages in intratumoral modulation therapy for primary brain tumors. *Robarts Research Retreat Event Program*. London, ON, Canada.
11. **Iredale, E.**, Deweyert, A., Hebb, M.O., Schmid, S., Peters, T., Wong, E. (2019) Computerized optimization of multi-electrode locations and voltages in intratumoral modulation therapy for primary brain tumors. *2019 CNS Departmental Research Day Program*. London, ON, Canada.
12. Deweyert, A., **Iredale, E.**, Xu, H., Wong, E., Schmid, S., Hebb, M.O. (2019) Intratumoral modulation therapy enhances multi-modality treatment platforms for pediatric diffuse intrinsic pontine glioma. *2019 CNS Departmental Research Day Event Program*. London, ON, Canada.
13. Deweyert, A., Di Sebastiano, A., Xu, H., Oliveira, C., **Iredale, E.**, Wong, E., Schmid, S., Hebb, M.O. (2018) Intratumoral modulation therapy: a novel

electrotherapeutic approach to control pediatric diffuse intrinsic pontine glioma and glioblastoma. *Oncology Research & Education Day Event Program*. London, ON, Canada.

14. **Iredale, E.**, Deweyert, A., Di Sebastiano, A., Xu, H., Oliveira, C., Schmid, S., Hebb, M.O., Wong, E. (2017) Simulation of electric field from implanted electrodes in an animal model for the treatment of glioblastoma. *Oncology Research & Education Day Event Program*. London, ON, Canada.
15. Deweyert, A., Xu, H., Oliveira, C., **Iredale, E.**, Wong, E., Schmid, S., Hebb, M.O. (2017) Intratumoral Modulation Therapy for glioblastoma: determination of the electric field intensity threshold for the induction of apoptosis in low passage patient-derived glioblastoma monolayer and neurosphere cultures. *Oncology Research & Education Day Event Program*. London, ON, Canada.

Research Presentations:

1. **Platform Presentation:** Electrode Array Design and Planning for Treatment of Brain Tumor Surgical Resection Cavity Margins with Anti-Cancer Electric Fields. (2023) American Association of Physicists in Medicine (AAPM) Annual Meeting & Exhibition, Houston, TX, United States.
2. **Platform Presentation:** A Planning Environment for Intracranial Electric Field Treatment of Brain Tumors. (2022) American Association of Physicists in Medicine (AAPM) Annual Meeting & Exhibition, Washington, DC, United States.
3. **Poster Presentation:** In Vitro Validation of Rotating Electric Fields for Treating Glioblastoma. (2022) Oncology Research & Education Day, Western University.
4. **Platform Presentation:** Multi-Electrode Intracranial Electric Field Treatment for Brain Tumors: Planning System and Robot-Assisted Electrode Implantation. (2022) CNS Departmental Research Day, Western University.
5. **Seminar Presentation:** Impact of Rotating Electric Fields on Patient Derived Glioblastoma Cells. (2022) Department of Medical Biophysics Seminar, Western University.
6. **Winning Poster Presentation & 2 min Talk:** Multi-Electrode Treatment Planning System for Intratumoral Modulation Therapy. (2021) CNS Departmental Research Day, Western University.
7. **Winning Poster Presentation & 6 min Talk:** Treatment Planning System for Multi-Electrode Intratumoral Modulation Therapy. (2021) Robarts Research Retreat, Western University.
8. **Poster Presentation & 3 min Talk:** Multi-Electrode Treatment Planning System for Intratumoral Modulation Therapy. (2021) Oncology Research & Education Day, Western University.
9. **Seminar Presentation:** Custom Multi-Electrode Planning System for the Treatment of Brain Tumors. (2021) Department of Medical Biophysics Seminar, Western University.
10. **Seminar Presentation:** Investigating Mechanisms of Action in the Application of Electric Fields on Single and Dividing Tumor Cells. (2020) Department of Medical Biophysics Seminar, Western University.

11. **Poster Presentation:** Computerized optimization of multi-electrode locations and voltages in intratumoral modulation therapy for primary brain tumors. (2019) Robarts Research Retreat, Western University.
12. **Platform Presentation:** Computerized optimization of multi-electrode locations and voltages in intratumoral modulation therapy for primary brain tumors. (2019) CNS Departmental Research Day, Western University.
13. **Seminar Presentation:** Spatiotemporal Optimization of Electric Field for the Treatment of Unresectable Brain Tumors. (2019) Department of Medical Biophysics Seminar, Western University.
14. **Seminar Presentation:** Applications of Electric Field Optimization Methods for Primary Brain Tumor Treatment with Intratumoral Modulation Therapy. (2019) Department of Medical Biophysics Seminar, Western University.
15. **Poster Presentation:** Optimization and design of implanted electrodes for the treatment of primary brain tumors. (2018) Fallona Family Interdisciplinary Showcase, Western University.
16. **Seminar Presentation:** Implanted Electrode Design and Optimization for the Treatment of Primary Brain Tumors. (2018) Department of Medical Biophysics Seminar, Western University.
17. **Poster Presentation:** Simulation of electric field from implanted electrodes in an animal model for the treatment of glioblastoma. (2017) Oncology Research and Education Day, Western University.
18. **Poster Presentation:** Electric Field Computer Simulations for Treatment of Glioblastoma In Vitro and In Vivo. (2017) Fallona Family Interdisciplinary Showcase, Western University.

Supervisory Activities:

- | | |
|-------------------|---|
| 05/2022 - 08/2022 | <p>Project Supervisor (2 Students)
Supervision of two undergraduate summer students with projects involving in vitro cell work for rotating electric fields on tumour cells and computational work on surgical resection cavity electrode array designs.</p> |
| 09/2021 - 04/2023 | <p>Project Supervisor (1 Student)
Supervision of undergraduate scholar's elective student with project investigating electric fields applied to brain tumour cells in vitro.</p> |
| 09/2021 - 08/2022 | <p>CAMPEP Advisor (1 Student)
Advising CAMPEP MSc Clinical Medical Biophysics student in the Academic Mentorship Program</p> |
| 01/2021 - 12/2021 | <p>Project Supervisor (2 Students)
Supervision of two undergraduate coop students with projects involving coding portions of a novel treatment planning system in 3D Slicer</p> |

01/2020 - 06/2020 **Project Supervisor (1 Student)**
Supervision of high school PEL co-op student with project investigating numerical optimization methods

Professional Memberships & Activities:

09/2022 - 08/2023 **WE-Empower**
Participation as accepted graduate student in WE-Empower Mentorship Program through WORLDiscoveries, Western University.

07/2022 - Present **AAPM Accessibility Subcommittee**
American Association of Physicists in Medicine (AAPM) Accessibility Subcommittee member, under the EDIC (Equity, Diversity, and Inclusion Committee).

07/2021 - 04/2023 **AAPM Membership**
American Association of Physicists in Medicine (AAPM) Student Member.

07/2021 - 04/2023 **COMP Membership**
Canadian Organization of Medical Physicists (COMP) Student Member.

10/2020 - 12/2020 **Contouring Bootcamp**
Completion of Anatomy and Radiology Contouring Bootcamp, Western University.